Title
Engineering electromagnetic wavefronts with metasurfaces

Author
Hsu, LiYi

Publication Date
2020

UNIVERSITY OF CALIFORNIA SAN DIEGO

Engineering electromagnetic wavefronts with metasurfaces

A dissertation submitted in partial satisfaction of the requirements for the degree Doctor of Philosophy

in

Electrical Engineering (Applied Physics)

by

Li-Yi Hsu

Committee in charge:

Professor Boubacar Kanté, Chair
Professor Richard Averitt
Professor Yu-Hwa Lo
Professor Daniel F. Sievenpiper
Professor Oscar Vazquez Mena

2020

The dissertation of Li-Yi Hsu is approved, and it is acceptable in quality and form for publication on microfilm and electronically:

Chair

University of California San Diego

2020

DEDICATION

To my family。

EPIGRAPH

The best way to predict your future is to create it.

-ABRAHAM LINCOLN

TABLE OF CONTENTS

Signature Page iii

Dedication iv

Epigraph v

Table of Contents vi

List of Figures viii

List of Tables xii

Acknowledgments xiii

Vita xv

Abstract of the Dissertation xvii

Chapter 1 Introduction 1
- 1.1 Generalized Snell's laws 2
- 1.2 General design methods of metasurface element 5
- 1.3 Outline of Dissertation 7
- 1.4 Reference 8

Chapter 2 9

Extremely Thin Dielectric Metasurface for Carpet Cloaking 9
- 2.1 Introduction 10
- 2.2 Phase Distribution 12
- 2.3 Dielectric Metasurface 14
- 2.4 Full Cloak Simulation 19
- 2.5 Conclusion 23
- 2.6 References 24

Chapter 3 27

Broadband and linear polarization metasurface carpet cloak in the visible 27
- 3.1 Introduction 27
- 3.2 Design Principle 29
- 3.3 Results 33
- 3.4 Conclusion 38
- 3.5 Reference 39

Chapter 4 Ultra-broadband, high efficiency, and linear polarization achromatic meta-lens from visible to telecommunication wavelength 42
- 4.1 Introduction 43
- 4.2 Design Principle 44
- 4.3 First Implementation: Hybrid metalens 45
- 4.4 Second Implementation: Fishnet-Achromatic-Metalens (FAM) 49
- 4.5 Efficiency ratio change with non-zero phase-shift intercepts in the metalens.. 53
- 4.6 Fabrication method 54
- 4.7 Experimental measurements 55

4.8 Performance Measurement 61
4.9 Conclusion 64
4.10 Reference 65

Chapter 5 Local phase method for designing and optimizing metasurface devices 68
5.1 Introduction 68
5.2 Local phase method 70
5.3 Deflector 72
5.4 High Numerical Aperture Concentrator 77
5.5 Conclusion 80
5.6 Reference 81

Chapter 6 From parabolic-trough to metasurface-concentrator: assessing focusing in the wave-optics limit 84
6.1 Introduction 85
6.2 Intercept factor and slope error 86
6.3 Quantitative analysis of IF/SE in non-perfect metasurface 88
6.4 Conclusion 96
6.5 Reference 98

Chapter 7 Summary 100

LIST OF FIGURES

Figure 1.1: Generalized Snell's law. (a) A wall with varying height along the seashore will change the optimal route for a lifeguard to reach a drowning man in the sea. (b) The interface between the two media is artificially structured in order to introduce an abrupt phase shift in the light path, which is a function of position along the interface. 4

Figure 1.2: Phase shift and magnitude of reflection for different radii and schematic of the unit cylindrical elements. P (period), h (thickness of the resonator), R (radius), hs (thickness of the spacer), hg (thickness of the ground plane). Materials: TiO_2 (brown), SiO_2 (blue), Ag (grey). [7] 7

Figure 2.1: (a) Reflection from a flat plane. (b) Reflection from a flat plane with a counterclockwise rotation by an angle φ. Cases a and b are both governed by Snell's law. (c) Reflection from a Gaussian scatterer that can be treated locally, at each point along the surface, as a flat plane. 13

Figure 2.2: Schematic of the entire metasurface, discretized with 25 cylinders, and coordinate system. (Inset) Unit cell of the metasurface. The bottom black line is the ground plane, the light blue substrate is Teflon, and the dark blue cylinder is ceramic. The incident wave is polarized along the y axis. 14

Figure 2.3: Graded metasurface design flowchart (a) Scatterer geometry vs. position x. (b) Local incident angle vs. position x. (c) Phase shift vs. position x. (d) Height of the cylinder vs. position x.. 16

Figure 2.4: Simulated phase shift with varying height h and local incident angle θ_L for a frequency of 4.15 GHz. The dark points correspond to the different heights chosen for the 25 cylinders on the metasurface. 17

Figure 2.5: (a) Electric field reflection pattern for (a) a flat ground plane. (b) for a Gaussian scatterer. (c) for a Gaussian scatterer with dielectric cylinders cloaking metasurface. (d) for a Gaussian scatterer with more continuously varying refractive index. (e) Phase plot along the equi-phase line L in (a)-(d). 20

Figure 2.6: Phase difference on the equi-phase line L between the phase reflected by our metasurface (designed for 45 degree) and phase expected from a flat ground plane for different global incident angles.. 22

Figure 3.1: (a) Required phase-shift profile (in radians) at specified frequencies for a broadband metasurface carpet cloaking. (b) Phase-shift with position. (c) Phase-shift with frequency at specified positions.. 30

Figure 3.2: (a) Schematic of the carpet cloaking system. (b) The considered geometry of the unit cell of the metasurface. (c) Normalized electric field at 409 THz with w = 80 nm and θ_L = 45°.. 32

Figure 3.3: The design flowchart. (a) Bump geometry as function of the position (b) Local incident angle as function of the position. (c) The fitting result at x=0 (center of the bump). (d) Width of the slot waveguide as a function of the position.. 33

Figure 3.4: Fitting results for different positions (a) x = -7000 nm (b) x = -1400 um (c) x = -1400 nm (d) x = 7000 nm. 34

Figure 3.5: Real part of electric E field for the ground plane, bump, and metasurface at different frequencies from 375 THz to 460 THz. 35

Figure 3.6: Phase profile of electric E field in figure 3.5 (black dish lines) at different frequencies from 375 THz to 460 THz. (a) 375THz (b) 392 THz (c) 409 THz (d) 426 THz (e) 443 THz (f) 460 THz. 38

Figure 4.1 Design of metasurface (a) Schematic of a hybrid metalens. (b) Unit cell of the metalens (c) The normalized e-field of a unit cell at 375THz with L = 240 nm and p = 200 nm. (d) The intercept of the phase-shift. (e) The slope of the phase-shift. 47

Figure 4.2 Normalized power intensity distribution for different frequencies (a) 600 THz (b) 518 THz (c) 436 THz (d) 354THz (e) 272 THz and (f) 190 THz. The black crosses present focal points and the while dish line presents the designed focal length. 48

Figure 4.3 Simulation focal length in spectral range from 190 THz to 600 THz. 49

Figure 4.4 Schematic and scanning electron micrograph of a fishnet-achromatic-metalens (FAM). (a) Schematic of the proposed broadband metalens and its unit-cell. (b) Top view of an optical microscope image of a fabricated FAM and zoom-in showing the quality of the fabricated device. The scale bar represents 5 µm. 51

Figure 4.5 Design strategy of the FAM. To control the slope (a, c) and the phase-shift intercept (b, d), at least two parameters need to be controlled. The considered two parameters are the width and the radius (W, R). 52

Figure 4.6 Efficiency ratio between the metasurface with randomly distributed non-zero phase-shift intercept and the one with zero phase-shift intercept. 54

Figure 4.7 Fabrication flow chart of metalenses. 55

Figure 4.8 Experimental setup. 56

Figure 4.9 Experimental demonstration of achromatic and broadband focusing by a FAM. (a) Measured intensity profiles. (b) Normalized cross-section of the experimental measurements. (c) Normalized intensity profiles in the plane x = 0 (axial x-z plane). Black crosses represent the focal spots for different wavelengths from 640 nm to 1200 nm. 57

Figure 4.10 Top view (x-z plane) of the experimental intensity profiles of the achromatic metalens along axial planes at different wavelength from 640 nm to 1200nm (15µmx15µm). The black crosses represent the center of focal spots for different wavelength from 640 nm to 1200 nm. 58

Figure 4.11 presents the normalized intensity profiles along the black cross achromatic metalens in Fig. 4.10. Measured intensity profiles (1D and 2D) of the achromatic metalens at different wavelength from 640 nm to 1200 nm (15µmx15µm). The circles are the measurement and the lines are from an ideal Airy spot. 59

Figure 4.12 Top view (x-z plane) of the experimental intensity profiles of the achromatic metalens along axial planes at different wavelength from 640 nm to 1200nm (20µmx20µm). The black crosses represent the center of focal spots for different wavelength from 640 nm to 1200 nm. 60

Figure 4.13 Normalized intensity profiles along the black cross achromatic metalens in Fig. 4.12. Measured intensity profiles (1D and 2D) of the achromatic metalens at different wavelength from 640 nm to 1200 nm (20µmx20µm). The circles are the measurement and the lines are from an ideal Airy spot. 61

Figure 4.14 Measured performance of various FAMs. SEM of metalenses of diameter 20 µm (a), 15 µm (b), and 10 µm (c). (d) Comparison of the measured and designed focal lengths for metalenses of various sizes. € Focus efficiency and (f), FWHM at corresponding focal planes as a function of the wavelength.. 63

Figure 5.1: The schematic of the local phase method (LPM). The deflector super-cell is made of 9 different elements.. 71

Figure 5.2: Dimensions of (a) the rectangular elements. (b) the rectangular elements with covered layer. (c) the parallelepiped elements. Phase-shift obtained with the UCM with (d) the rectangular elements, (e) the rectangular elements with covered layer and (f) the parallelepiped elements. 73

Figure 5.3: Designing metasurfaces with rectangular elements. (a) Dimensions for the UCM and LPM metasurface elements. (b) Radar cross-section of the UCM and LPM metasurfaces. (c) Phase difference between two adjacent elements for two metasurfaces. (d) Phase error for the UCM and LPM metasurfaces... 75

Figure 5.4: Designing metasurfaces with rectangular elements embedded in a SiO_2 layer. (a) Dimensions for the UCM and LPM metasurface elements. (b) Radar cross-section of the UCM and LPM metasurfaces. (c) Phase difference between two adjacent elements for two metasurfaces. (d) Phase error for the UCM and LPM metasurfaces. 76

Figure 5.5: Designing metasurfaces with slanted parallelepiped elements. (a) Dimensions for the UCM and LPM metasurface elements. (b) Radar cross-section of the UCM and LPM metasurfaces. (c) Phase difference between two adjacent elements for two metasurfaces. (d) Phase error for the UCM and LPM metasurfaces. 77

Figure 5.6: (a) The schematic of the concentrator. (b) Dimensions for unit cell method and LPM (c) Phase difference between two adjacent elements for the two methods. (d) Phase error for the two methods. 79

Figure 5.7: Real part of the reflected electric field for (a) the UCM, and (b) for the LPM. The black rectangular boxes represent the index position of the first 11 elements (from 0 to 10). 79

Figure 5.8: Total power density plot for (a) the UCM, and (b) for the LPM. The LPM increase the power at the spot. 80

Figure 6.1: (a) Schematic of the parabolic concentrator: comparison between the ideal and real cases. (b) Ideal metasurface with uniform sampling of the exact phase required for a concentrator. (c) Real metasurface with a phase variation $\delta\varphi$ due to fabrication imperfections. 88

Figure 6.2: (a-c) Schematic of a conventional metasurface structure (cylinders, rectangular parallelepipeds and ellipses.) (d-f) Phase shift for different size of the cylinders, rectangular parallelepipeds and ellipses. 91

Figure 6.3: Flowchart of transformation. (a) The phase shifts as a function of a geometrical parameter. (b) The sensitivity of the phase shifts to the parameter resolution in degree/nm. (c) Same in absolute value for an average noise of 10 nm. (d) Sensitivity in degree as a function of the targeted phase shift. 93

Figure 6.4: Sensitivity for cylinders, ellipses and rectangular parallelepipeds. 94

Figure 6.5: (A_1) Intercept factor and (A_2) Standard variation of the slope error for cylinders, rectangular parallelepipeds and ellipses. (B) Power pattern. 96

LIST OF TABLES

Table 2.1 Samples of calculated z(x), θ_L(x), Φ(x) and h(x) on the scatterer. 18

ACKNOWLEDGMENTS

Firstly, I would like to express my sincere gratitude to my advisor, Professor Boubacar Kanté, for the continuous support of my Ph.D study and related research, for his encouragement, guidance, and immense knowledge. We worked together and obtained the first big funding from department of energy. I remember it seemed like never-ending proposals, reports, and presentations. In hindsight, our efforts were not in vain.

I would also like to thank my other committee members, Prof. Daniel F. Sievenpiper for his fruitful advice and kindly support of my microwave measurement. Prof. Yu-Hwa Lo for his broadly encompassing courses on semiconductor and nanoscience. Prof. Richard Averitt and Oscar Vazquez Mena for fruitful discussions on the utility of my research in various other fields.

I have many to thank due to the interdisciplinary nature of my research. I owe a great deal of thanks to Abdoulaye Ndao for his supports on nanofabrication, optical setups/measurements, report/paper revision and invaluable suggestions on search and my life over the years. I would like to thank Thomas Lepetit for his mentorship and useful feedback in my early research. Thanks to Jeongho Ha for amazing nanofabrication. Thanks to Ashok Kodigala for setting up the laboratory and fruitful discussions. Thanks to Junhee Park for kindly help on drawing many nice figures. I would also like to thank Matthieu Dupré for the help in the setup of supercomputers and the microwave measurement suggestions. A special thanks to Julie Moritz for the countless paperwork. Last, I would also like to thank my many colleagues in the group: Babak Bahari, Ricardo Tellez-Limon, Wanwoo Noh, Quynh Le Van, Hadiseh Nasari, Rushin Contractor, Zhetao Jia, Mutasem Odeh.

Of course, none of this would happen without the love and support of my parents, Ruilong and YueTao, and my brother, ShengKai.

Chapter 2, in part, is a reprint of the material as it appears in L.-Y. Hsu, T. Lepetit, B. Kanté, “Extremely Thin Dielectric Metasurface for Carpet Cloaking,” Progress in Electromagnetics Research, 152, 33–40 (2015). The dissertation author was the primary researcher and author of this paper.

Chapter 3, in part, is a reprint of the material as it appears L.-Y. Hsu, A. Ndao, B. Kanté, “Broadband and linear polarization metasurface carpet cloak in the visible,” Optics Letters 44 (12), 2978-2981 (2019). The dissertation author was the primary researcher and author of this paper.

Chapter 4, in part, has been submitted for publication of the material as it may appear in Nature Communications, 2020, A. Ndao, J. Ha, J. Park, and B. Kanté. The dissertation author was the primary researcher and author of this paper.

Chapter 4, in part, is currently being prepared for submission for publication of the material. A. Ndao and B. Kanté. The dissertation/thesis author was the primary investigator and author of this material.

Chapter 5, in part, is a reprint of the material as it appears L.-Y. Hsu, M. Dupré, A. Ndao, J. Yellowhair, B. Kanté, “Local phase method for designing and optimizing metasurface devices,” Optics express 25 (21), 24974-24982 (2017). The dissertation author was the primary researcher and author of this paper.

Chapter 6, in part, is a reprint of the material as it appears L.-Y. Hsu, M. Dupré, A. Ndao, B. Kanté, “From parabolic-trough to metasurface-concentrator: assessing focusing in the wave-optics limit,” Optics letters 42 (8), 1520-1523 (2017). The dissertation author was the primary researcher and author of this paper.

VITA

2020	Doctor of Philosophy, Electrical Engineering (Applied Physics), University of California San Diego USA
2007	Master of Science, Physics, National Tsing Hua University Taiwan
2005	Bachelor of Science, Physics, National Chung Hsing University Taiwan

PUBLICATIONS

L.-Y. Hsu, A. Ndao, B. Kanté, “Broadband and linear polarization metasurface carpet cloak in the visible,” Optics Letters 44 (12), 2978-2981 (2019).

J. Ha, A. Ndao, **L.-Y. Hsu**, J.-H. Park, B. Kante, “Planar dielectric cylindrical lens at 800 nm and the role of fabrication imperfections,” Optics express 26 (18), 23178-23184 (2018).

M. Dupré, **L.-Y. Hsu**, B. Kanté, “On the design of random metasurface based devices,” Scientific reports 8 (1), 7162 (2018).

L.-Y. Hsu, M. Dupré, A. Ndao, J. Yellowhair, B. Kanté, “Local phase method for designing and optimizing metasurface devices,” Optics express 25 (21), 24974-24982 (2017).

L.-Y. Hsu, M. Dupré, A. Ndao, B. Kanté, “From parabolic-trough to metasurface-concentrator: assessing focusing in the wave-optics limit,” Optics letters 42 (8), 1520-1523 (2017).

R. Tellez-Limon, B. Bahari, **L.-Y. Hsu**, J.-H. Park, A. Kodigala, B. Kanté, “Integrated metaphotonics: symmetries and confined excitation of LSP resonances in a single metallic nanoparticle,” Optics express 24 (13), 13875-13880 (2016).

L.-Y. Hsu, T. Lepetit, B. Kanté, “Extremely Thin Dielectric Metasurface for Carpet Cloaking,” Progress in Electromagnetics Research, 152, 33–40 (2015).

ABSTRACT OF THE DISSERTATION

Engineering electromagnetic wavefronts with metasurfaces

by

Li-Yi Hsu

Doctor of Philosophy in Electrical Engineering (Applied Physics)

University of California San Diego 2020

Professor Boubacar Kanté, Chair

Planar structured interfaces, also known as metasurfaces are continuously attracting interest owing to their ability to manipulate fundamental attributes of light including angular momentum, phase polarization. Metasurface can utilize abnormal phase abrupt changes at an interface to manipulate electromagnetic wave fronts. It provides an effective method for applications including planar lens imaging, polarization splitter, half-wave plate, extra thin layer hologram and so on. Different from traditional optical devices are bulky, metasurfaces are thin layers with multifunction, low loss, and easy to integrate. Due to their advantages, metasurfaces

have become a rapidly growing field of research and have attracted wide attention. In this dissertation, we focus on both physics and applications of manipulating electromagnetic (EM) wave fronts with the metasurfaces. First, we review the mechanics of metasurface and the general design methods of metasurfaces. Secondly, as the application, we demonstrate a novel and simple approach to cloaking a scatterer on a ground plane with an extremely thin dielectric metasurface. The metasurface compensates the wave fronts distortion by a scatterer. With this design, any observer will just see a flat ground plane and the scatterer will be invisible and thus effectively cloaked. Then, a linear polarization broadband metasurface carpet cloaking at visible is studied. We reveal the requirements of linear polarization broadband (wavelengths from 650 nm to 800 nm) metasurface carpet cloaking and propose a unit cell to provide the required phase. The 2D simulation results show the distortion is fixed due to our metasurface design and the 1D result further show the quantity of corrected phase. In additional to linear polarization broadband metasurface carpet cloaking, we also investigate linear polarization, high efficiency, and broadband achromatic meta-lens. Despite exciting findings, achieving simultaneously high efficiencies and large bandwidths has remained a challenge. Recent state of the art results in the visible reported a bandwidth from 470 nm to 670 nm with an efficiency of 20 % while the efficiency of 40% was obtained for the bandwidth from 400 nm to 660 nm. Here, we experimentally report polarization-independent, fishnet-achromatic-metalenses (FAM) with measured average efficiencies over 70% in the band from the visible (640 nm) to the infrared (1200 nm).

Metasurfaces are so far demonstrated using unit cell method where the approach usually used to engineer metasurface devices assumes that neighboring elements are identical, by extracting the phase information from simulations with periodic boundaries, or that near-field coupling between particles is negligible, by extracting the phase from single particle simulations. In this thesis, we proposed a new method that quantify the phase error of each element of the metasurfaces with the proposed local phase method paves the way to the design of highly efficient metasurface devices including, but not limited to, deflectors, high numerical aperture metasurface concentrators, lenses, cloaks, and modulators. As illustrations, we proposed to use deflectors and high numerical aperture concentrators where we demonstrate an improvement of 100% compare to unit cell method. We also introduced and evaluated the intercept factor and the slope error from solar industry to quantify fabrication imperfections. The concept opens a new path to calculate metasurfaces sensitivities to fabrication imperfections and will be critical for practical systems.

Chapter 1

Introduction

Optics is an ancient discipline. Archaeological excavation proves that as early as about 3,000 years ago, the ancient Assyrians made lenses by crystals although the purpose is unclear. At the end of the 16th century, Zacharias Janssen invented the microscope and later Robert Hooke improved the microscope and used it to observe bacteria. It was the first time the bacteria were discovered. At the beginning of the 17th century, Hans Lippershey and others invented the telescope. People begin to explore the mystery of the universe. In the first half of the 17th century, Snell and Descartes studied mathematically the formula of the reflection and refraction of light. In 1666, Newton used a prism to demonstrate that all the colors already existed in white light and stated that light was composed of corpuscles (particles of matter). On the other hand, Huygens is an opponent of the light particle theory. He proposed that light is a wave-like sound. The famous Huygens principle states that every point on a wave front is the source of spherical wave and the sum of them forms the wave front at the subsequent time. Around 1860, Maxwell revealed that electric and magnetic fields can be transformed into each other to form an electromagnetic wave and light is also an electromagnetic wave. In the historical development of optical component, realizing full control of electromagnetic (EM) waves within the whole frequency domain is one of the human dreams. It is not only important basic scientific research significance, but also has tremendous applications in different fields such as information communication, national defense, and energy utilization. One of the key issues is how to control EM waves efficiently with a compact size. However, conventional optics use accumulated propagating phases to control EM waves and hence require huge space (>1000 times wavelength) to achieve certain functionality. Besides, due to the dispersion of material, the functionality varies with different frequencies. Recently, metasurface was proposed to overcome this issue. Metasurfaces are extremely thin, man-made surfaces whose transmission /reflection properties (magnitude and phase) can be tailored at will by their structures. This versatility makes them ideal for the design of compact and highly efficient optical elements. Recently, interest has turned towards thinner, lighter devices known as metasurfaces [1-5]. They are subwavelength nanostructured interfaces, capable of controlling optical waves], on both fundamental science and diversified applications of metasurfaces. In this section, the foundation of metasurface which is the generalized Snell's law, general design rule of metasurface, and the outline of dissertation will be introduced.

1.1 Generalized Snell’s laws

When light is incident on the interface of the two media, reflection and refraction are generated, and the direction satisfies the Snell's law.

$$n_1 \sin\theta_1 = n_2 \sin\theta_2 \tag{1}$$

where n_1 and n_2 are the refractive index of the two media and θ_1 and θ_2 are the angle measured from the normal of the boundary for the two media. In fact, Snell's law can be derived from Fermat's principle, which states that the path taken by a ray of light between two points is that of least time. To be more specific, the optical path taken by light between two-point A and B is defined as [5]

$$S = \int_A^B d\varphi(r) = \int_A^B n(r)dr, \tag{2}$$

where $\varphi(r)$ is the local phase and $n(r)$ is the local index of refraction. Both Snell's laws of reflection and refraction can be derived from Fermat's principle.

Fermat's principle was simply illustrated by Richard Feynman with the drowning man dilemma [6]. Imagine a lifeguard wanting to reach a drowning man in the shortest time possible (see Figure 1.1 (a)). Because a lifeguard runs faster than he swims ($\nu_{land} > \nu_{sea}$), he should head for a point on the seashore that extends the running distance in exchange for a shortened swimming distance. The optimal route (white dashed curve in Figure 1.1 (a)) satisfies the following equation: $\sin\theta_i/\nu_{land} - \sin\theta_t/\nu_{sea} = 0$. This equation has the same form as Snell's law $\sin\theta_i/\nu_i - \sin\theta_t/\nu_t = 0$, where v_i and v_t are, respectively, the phase velocity of light in the media before and after the light beam goes through the interface.

Now, consider the impact of a wall with varying height along the seashore. It will change the optimal route for a lifeguard to reach a drowning man because the lifeguard has to consider the time to climb up and down the wall. As before, there will necessarily be an optimal route (yellow solid curve in Figure 1.1 (a)). Likewise, a gradient of phase jump on the interface between two optical media will change the optical path according to Fermat's principle. This leads to generalized Snell's laws for reflection and refraction [6].

To be more specific, the optical path taken by light between two point A and B can now be redefined as

$$S = \int_A^B d\varphi(r) + \varphi(r_s). \tag{3}$$

It is this additional phase shift $\varphi(r_s)$, which is localized at the interface between two media and can be implemented with metasurfaces, that is the key to light manipulation and novel devices.

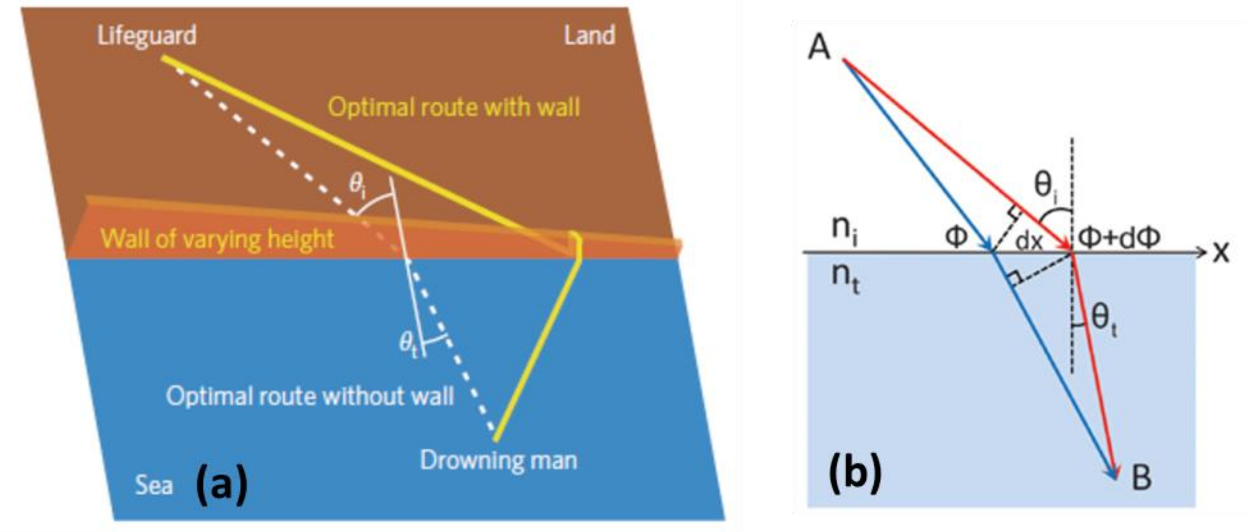

Figure 1.1: Generalized Snell's law. (a) A wall with varying height along the seashore will change the optimal route for a lifeguard to reach a drowning man in the sea. Likewise, a gradient of phase jump on the interface between two optical media will change the path of stationary phase according to Fermat's principle, leading to a generalized Snell's law [6]. (b) The interface between the two media is artificially structured in order to introduce an abrupt phase shift in the light path, which is a function of position along the interface [5].

Generalized Snell's laws for reflection and refraction are a natural consequence of this redefined optical path [6]. Consider a plane wave incident on an interface between two media (Figure 1.1 (b)). Fermat's principle dictates that the phase difference between two points that are infinitesimally close to the optimum light path be zero,

$$[k_0 n_i \sin\theta_i dx + (\Phi + d\Phi)] - [k_0 n_t \sin\theta_t dx + \Phi] = 0, \tag{4}$$

where Φ and $\Phi + d\Phi$ are the phase discontinuities across the interface. Equation (3) leads to the generalized Snell's law of refraction,

$$n_t \sin\theta_t - n_i \sin\theta_i = \frac{1}{k_0}\frac{d\Phi}{dx}. \tag{5}$$

Equation (4) implies that a refracted wave can have any arbitrary direction provided a suitable phase gradient along the interface exists. Similarly, for reflection we have

$$n_i \sin\theta_r - n_i \sin\theta_i = \frac{1}{k_0}\frac{d\Phi}{dx}. \tag{6}$$

Equation (5) implies that a reflected wave can have any arbitrary direction provided a suitable phase gradient along the interface exists. The main breakthrough brought by these generalized Snell's laws is that light propagation can be manipulated by a single, very thin layer localized at the interface (metasurface). Recent years have seen the proliferation of extremely flat optical component, which are rapidly replacing previous traditional (bulky) optics designs.

1.2 General design methods of metasurface element

In the previous section, we reviewed the general Snell's Law. In order to manipulate light propagation, it requires precise control of a phase gradient across an interface. In general, there are two main methods to design the elements of metasurfaces to obtain the amplitude and phase required. The first one is single meta-atom method [5]. In this method, people calculate the reflection or transmission of a single particle and the assumption is the coupling between particles is ignorable. In the reference 5, authors used V-antennas to provide the phase gradient. They solved the integral equations for the currents of the symmetric and antisymmetric modes to obtain the optical properties of V-antennas. After the current distributions are known, they calculated the far-field radiation and the transmission. However, there is usually no analytical solution for a meta-atom but a numerical simulation can provide the information we need. In a numerical simulation, a probe is put to record the transmission/reflection, and perfectly matched layers (PMLs) are used. Hence, we can simulation the transmission of a single meta-atom. The second main method is unit cell method. In this approach, the unit cell boundary condition is used. It means the phases are obtained in infinity and identical neighbors. This method is valid if coupling differences between identical neighbors and different neighbors are ignorable. Take a dielectric cylinder element of reflective metasurface as example [7]. Figure 1.2 shows the dielectric metasurfaces unit cell. It consists of a TiO_2 cylindrical resonator on a SiO_2 (h_s = 440 nm) – silver (hg = 100 nm) multilayer. Silicon dioxide (SiO_2) is the spacer and silver (Ag) serves as ground plane to work in reflection. The tuning parameter is radius (R) which changes to achieve the required phase. The main difference is that the metasurface now is periodic boundary condition along the x and y directions instead of PMLs. In this thesis, unit cell method is used from chapter 2 to chapter 5. After that, the coupling effect will be considered.

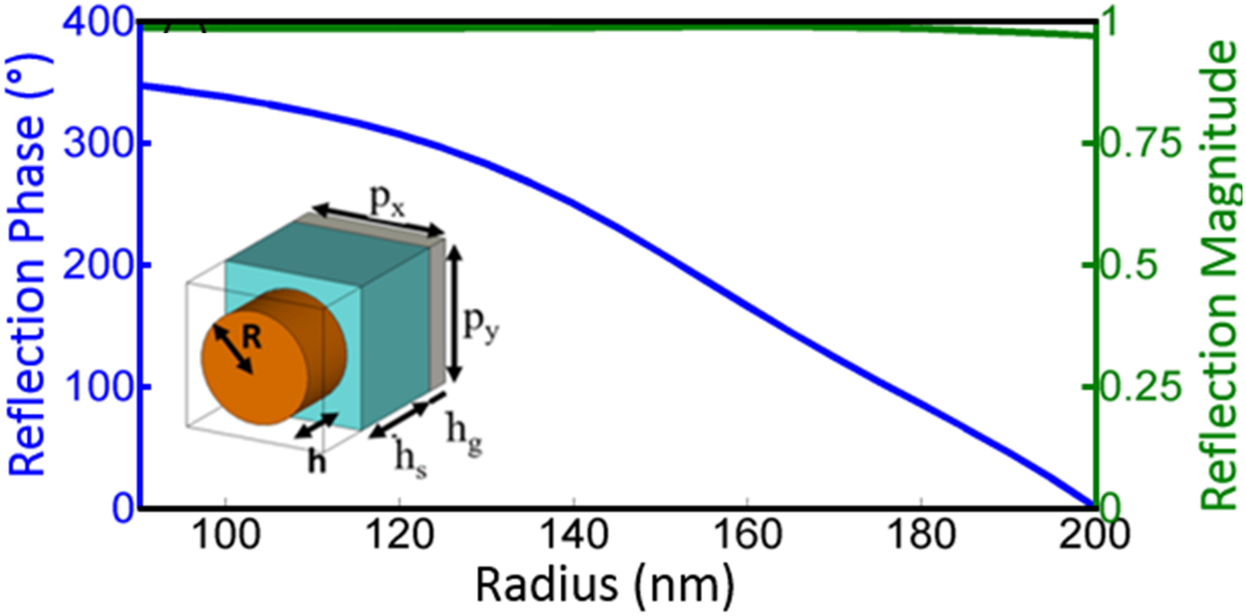

Figure 1.2: Phase shift and magnitude of reflection for different radii and schematic of the unit cylindrical elements. P (period), h (thickness of the resonator), R (radius), hs (thickness of the spacer), hg (thickness of the ground plane). Materials: TiO_2 (brown), SiO_2 (blue), Ag (grey). [7]

1.3 Outline of Dissertation

The dissertation work focuses on metasurface design rules, the impact of fabrication imperfection, broadband metasurface and their applications such as carpet cloaking, deflector, concentrator and meta-lens. They are organized as follows. Chapter 2 provides an example of designing a metasurface carpet cloaking as applications based on metasurfaces. Chapter 3 discusses the requirements of broadband metasurfaces and provides a solution to increase the bandwidth of the metasurface carpet cloaking more than octave bandwidth. Chapter 4 shows a novel way to design broadband linear polarization achromatic meta-lens. Chapter 5 builds a new metasurface design method called local phase method accounting all the coupling effects and used deflectors and high numerical aperture concentrator as illustrations of the proposed method (Local Phase Method). Chapter 6 systematically analyze the impact of fabrication imperfection and re-define the intercept factor/ slope error in solar industry for metasurface to quantify the impact of fabrication imperfection. Lastly, in Chapter 7, we summarize the present work.

1.4 Reference

1. Lalanne, P., Astilean, S., Chavel, P., Cambril, E. & Launois, H. Blazed binary subwavelength gratings with efficiencies larger than those of conventional échelette gratings. Opt. Lett. 23, 1081-1083 (1998).

2. Bomzon, Z., Kleiner, V. & Hasman, E. Pancharatnam-Berry phase in space variant polarization-state manipulations with subwavelength gratings. Opt. Lett. 26, 1424-1426 (2001).

3. Lu, F., Sedgwick, F. G., Karagodsky, V., Chase,C., & Chang-Hasnain, C. J. Planar high-numerical-aperture low-loss focusing reflectors and lenses using subwavelength high contrast gratings, Opt. Exp. 18, 12606-12614 (2010).

4. Fong, B. H., Colburn, J. S., Ottusch, J. J., Visher, J. L. & Sievenpiper, D. F. Scalar and tensor holographic artificial impedance surfaces. IEEE Trans. Antennas Propag. 58, 3212-3221 (2010).

5. Yu, N. F., Genevet, P., Kats, M. A., Aieta, F., Tetienne, J.-P., Capasso, F., Gaburro, Z., Light propagation with phase discontinuities: generalized laws of reflection and refraction. Science 334, 6054 (2011).

6. Yu, N., Capasso, F. Flat optics with designer metasurfaces. Nature Mater 13, 139–150 (2014).

7. J. Ha, A. Ndao, L.-Y. Hsu, J.-H. Park, B. Kante, Planar dielectric cylindrical lens at 800 nm and the role of fabrication imperfections, Optics express 26 (18), 23178-23184 (2018).

Chapter 2

Extremely Thin Dielectric Metasurface for Carpet Cloaking

We propose a novel and simple geometrical approach to cloaking a scatterer on a ground plane. We use an extremely thin dielectric metasurface to reshape the wavefronts distorted by a scatterer in order to mimic the reflection pattern of a flat ground plane. To achieve such carpet cloaking, the reflection angle has to be equal to the incident angle everywhere on the scatterer. We use a graded metasurface and calculate the required phase gradient to achieve cloaking. Our metasurface locally provides additional phase to the wavefronts to compensate for the phase difference amongst light paths induced by the geometrical distortion. We design our metasurface in the microwave range using highly sub-wavelength dielectric resonators. We verify our design by full-wave time-domain simulations using micro-structured resonators and show that results match theory very well. This approach can be applied to hide any scatterer under a metasurface of class C1 (first derivative continuous) on a ground plane not only in the microwave regime, but also at higher frequencies up to the visible.

2.1 Introduction

Due to their amazing ability to manipulate electromagnetic waves, metamaterials have been extensively studied in the past fifteen years. They have resulted in several novel concepts and promising applications, such as cloaking devices [1-12], concentrators [13-15], wormholes [16] and hyperlenses [17]. Among all potential applications, invisibility cloaks especially received considerable attention.

Up to now, the main theoretical tool used for designing invisibility cloaks has been transformation optics/conformal mapping [1-2]. According to Fermat's principle, an electromagnetic wave will travel between two points along the path of least time. In a homogeneous material, this path is just a straight line. However, in an inhomogeneous material, the path becomes a curve because waves travel at different speeds at different points. Thus, one can control the path of waves by appropriately designing the material parameters (electric permittivity and magnetic permeability). In the case of cloaking, a metamaterial surrounding the target can be used to force light bypass a region of space, effectively isolating it from incoming electromagnetic waves.

Using transformation optics as the design method, the first experimental demonstration of cloaking was achieved at microwave frequencies [3]. However, transformation optics usually leads to highly anisotropic and inhomogeneous material parameters. Besides, extreme material parameter values, such as negative or near-zero, are also often required. To obtain extreme values for the permeability, split-ring resonators (SRRs) with magnetic resonances have been used. Such resonances are strongly dispersive and result in cloaks working only in a narrow frequency range. Most metals are also highly lossy at optical frequencies, which prohibits a simple scaling of SRRs down to the nanoscale [18-21].

Recently, a refinement of the transformation optics strategy was put forward [4]. It is called ‘hiding under the carpet’ and works not by routing light around a given scatterer but by transforming its reflection pattern into that of a flat plane. With a well-designed metamaterial, reflected waves appear to be coming from a flat plane and the scatterer on top of it thus becomes invisible. A major drawback of metamaterial-based cloaking devices is that they are large in size. This is because a large space is needed to progressively bend light.

More recently, metasurfaces have been used to overcome this specific disadvantage of metamaterials, although in a different context [22-23]. Metasurfaces or frequency selective surfaces, which are the surface version of metamaterials, have the inherent advantage of taking up less physical space than metamaterials. They have raised significant attention due to the simplified design afforded by generalized Snell’s laws of reflection and refraction [24]. In reference 24, it was shown in a simple and elegant way that wave propagation can be controlled by using a thin coating layer with a properly designed phase gradient over the surface. Many applications have come from metasurfaces, such as reflect-array, flat lenses, and hologram-based flat optics [25]. More recently, total cross-polarization control has also been demonstrated [26].

We propose in this paper a dielectric metasurface with a tailored phase gradient for carpet cloaking. We show that a single extremely thin ($\lambda/12$) all-dielectric metasurface is sufficient to accomplish invisibility. Once the scatterer is covered with the designed metasurface, no observer can distinguish it from a flat surface.

2.2 Phase Distribution

The carpet surface under which cloaking is achieved is described by a surface z(x,y). To illustrate our design strategy, we consider a scattering surface (invariant in y) that is described by a Gaussian function.

$$z(x) = Ae^{-\frac{x^2}{\sigma^2}} \tag{1}$$

To illustrate the cloaking mechanism, we consider two simple cases. In Fig. 2.1(a), an incident wave is reflected by a flat ground plane. Snell's law dictates that the reflection angle is equal to the incident angle ($\theta_r = \theta_i$). In Fig. 2.1(b), when the flat ground plane is rotated counterclockwise by an angle φ, the new incident angle becomes $\theta_i - \varphi$ while the new reflection angle becomes $\theta_r + \varphi$. Approximating each point of the Gaussian scatterer locally by a flat plane, we can design the entire cloak simply based on the geometric considerations made in Figs. 2.1(a-b).

To control the reflection angle, we use the generalized Snell's law of reflection [24]

$$sin(\theta_r) - sin(\theta_i) = \frac{1}{k_i}\frac{d\Phi(x)}{dx} \tag{2}$$

We have introduced the wavevector in the incident medium k_i and the phase distribution $\Phi(x)$. From Eq. (2), the reflection angle is entirely controlled by the phase gradient. Various phase gradients can be achieved with a graded metasurface. For example, we can design a suitable phase gradient on the plane to ensure that the reflected ray in Fig. 2.1(b) follows the same path as the one in Fig. 2.1(a). Hence, the observer will be lead to believe that he/she sees the original flat ground. plane without any rotation.

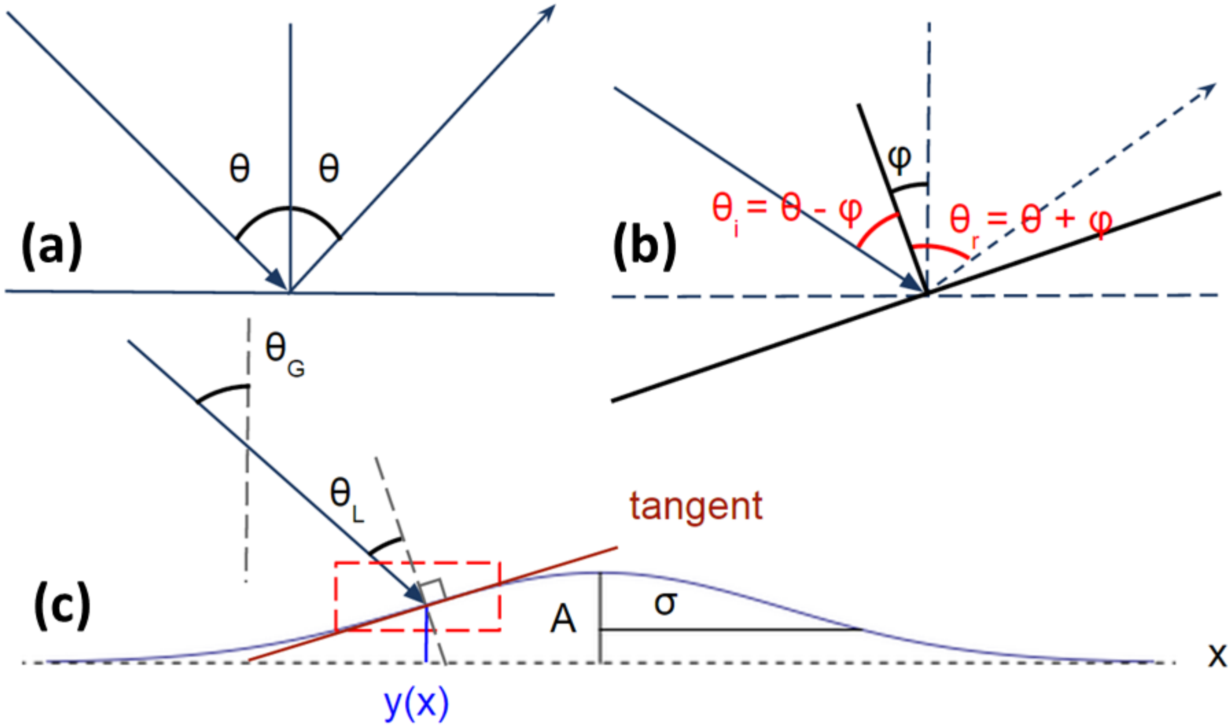

Figure 2.1: (a) Reflection from a flat plane. (b) Reflection from a flat plane with a counterclockwise rotation by an angle φ. Cases a and b are both governed by Snell's law. (c) Reflection from a Gaussian scatterer that can be treated locally, at each point along the surface, as a flat plane.

Treating each point on the Gaussian scatterer locally as a flat plane, we can parametrize the entire scatterer by a local incident angle θ_L that is x-dependent and that is distinct from the global incident angle θ_G (see Fig. 2.1(c)). Assuming the wave is propagating in vacuum we can then write

$$sin(2\theta_G - \theta_L) - sin(\theta_L) = \frac{1}{k_0}\frac{d\Phi(x)}{dx} \tag{3}$$

The phase gradient can then be expressed as a function of the scatterer's shape $z(x)$

$$\frac{d\Phi(x)}{dx} = 2k_0 cos\theta_G \frac{dz(x)}{dx} \tag{4}$$

Finally, after integration the phase distribution $\Phi(x)$ is given by

$$\Phi(x) = 2k_0 z(x) cos\theta_G \tag{5}$$

where *const* is chosen from the known phase of the flat ground plane. From Eq. (5), we see immediately that in the limit of a flat scatterer, the phase distribution is identically constant as it should be. By providing the appropriate phase distribution, as dictated by Eq. 5, we can hide an arbitrary scatterer by making it look like a flat ground plane using a metasurface of class C^1. Our concept is general and the use of loss-free dielectric resonator can lead to applications in optics where metals are lossy [27]. Clearly, the concept introduced here can be realized at higher frequencies by simply picking a proper class of sub-wavelength metasurface elements. A large phase-shift can still be achieved by the same technology using dielectric cylinders metasurface with lower permittivities such as Si or TiO_2. Those materials have been used to achieve near infrared/ optical Mie resonances [28].

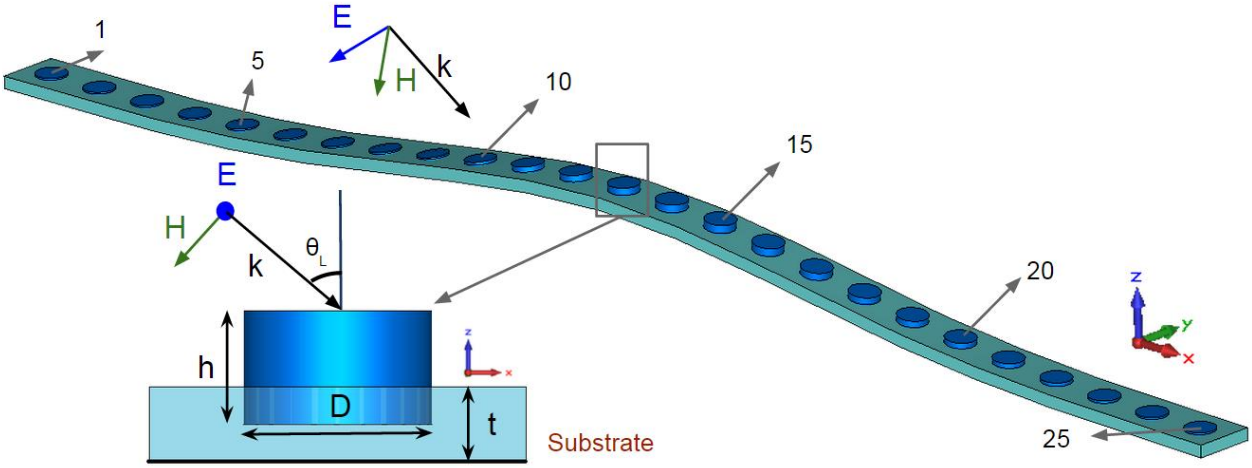

Figure 2.2: Schematic of the entire metasurface, discretized with 25 cylinders, and coordinate system. (Inset) Unit cell of the metasurface. The bottom black line is the ground plane, the light blue substrate is Teflon, and the dark blue cylinder is ceramic. The incident wave is polarized along the y axis.

2.3 Dielectric Metasurface

We design a microwave metasurface made of dielectric cylinders for a frequency of 4.15 GHz (C-band). Cylinders have a circular cross-section and a fixed diameter ($D = 0.58$ in) and the substrate has a fixed thickness ($t = 0.23$ in). Our metasurface is periodic along y with a sub-wavelength unit cell ($w = 1.16$ in). Cylinders are made of a high-permittivity ceramic ($\varepsilon_r = 41 \pm 0.75$) with a low loss-tangent ($tan\delta = 1.10^{-4}$) and are embedded in a Teflon substrate ($\varepsilon_r = 2.1$) with an equally low loss-tangent ($tan\delta = 2.10^{-4}$). Our metasurface is thus almost lossless.

The scatterer is described by a Gaussian function as per Eq. 1. Its standard deviation σ is four times the unit cell width ($\sigma = 4.64$ in) while its amplitude A is the same as the unit cell width ($A = 1.16$ in). Finally, the global incident angle θ_G is chosen to be 45 degrees and the polarization of the incident wave is along the y axis (*i.e.*, TE-polarized). Note that the polarization of reflected wave is the same as the one of the incident wave in our system. To obtain a suitable phase gradient and phase distribution, we design a local variation in cylinder height. Note that this is the only geometrical parameter that is varied. As shown in Fig. 2.3, from the scatterer geometry $z(x)$, we compute the local incident angle $\theta_L(x)$, and then the phase distribution $\Phi(x)$ from Eq. 5. As can be seen from Table 1, to hide the Gaussian scatterer phase covering the 0-to-2π range is needed for different local incident angles.

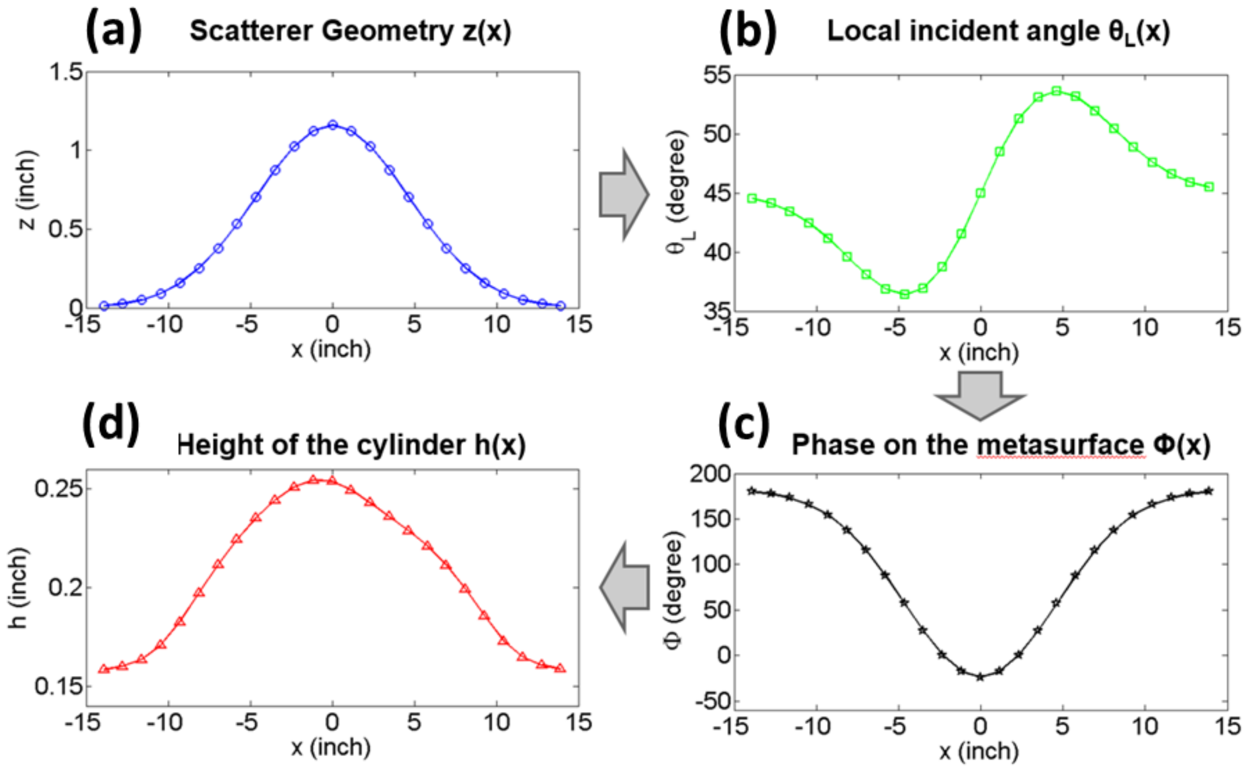

Figure 2.3: Graded metasurface design flowchart (a) Scatterer geometry vs. position x. (b) Local incident angle vs. position x. (c) Phase shift vs. position x. (d) Height of the cylinder vs. position x.

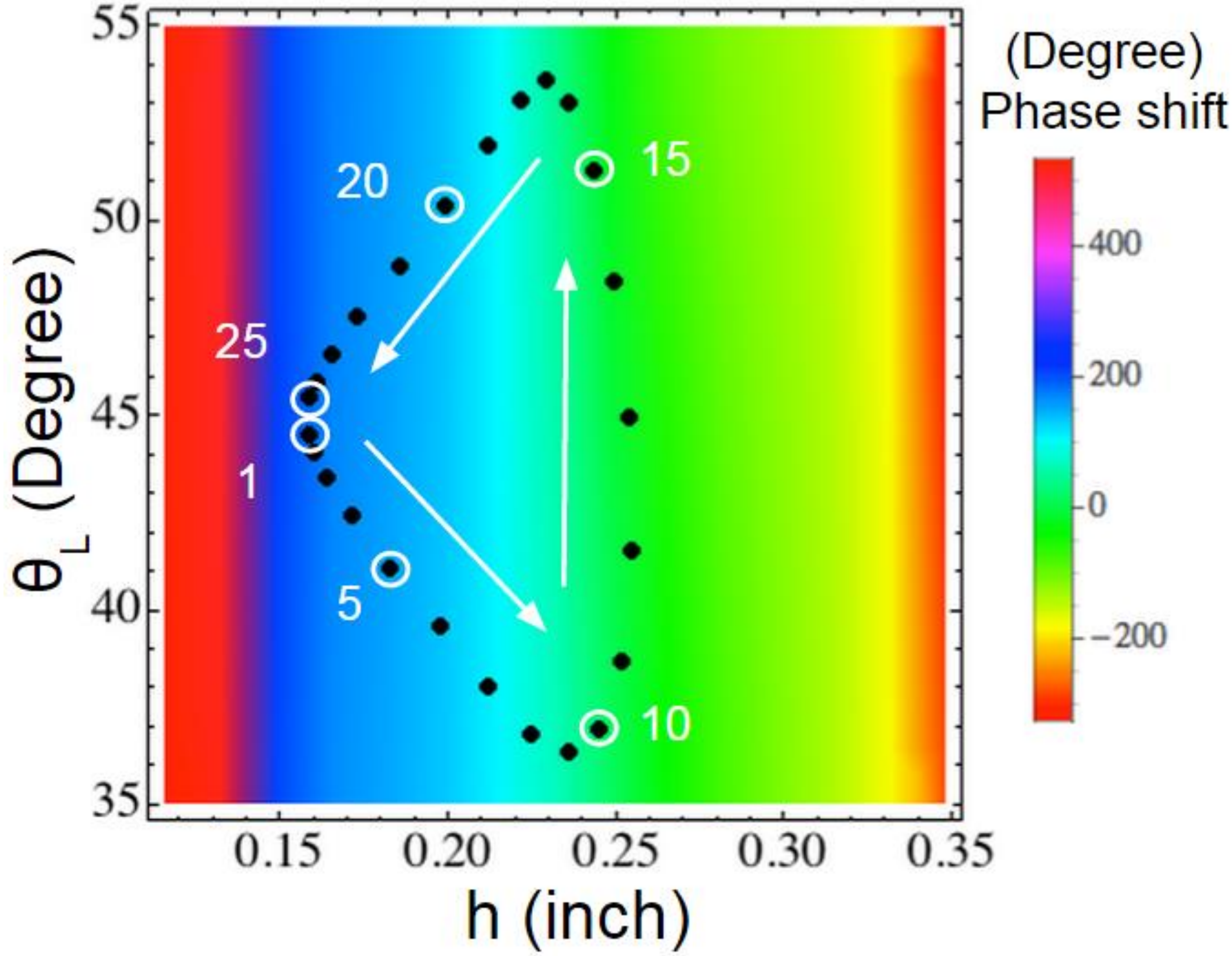

Figure 2.4: Simulated phase shift with varying height h and local incident angle θ_L for a frequency of 4.15 GHz. The dark points correspond to the different heights chosen for the 25 cylinders on the metasurface.

Table 2.1 Samples of calculated z(x), $\theta_L(x)$, $\Phi(x)$ and h(x) on the scatterer.

Function \ Index	1	5	10	15	20	25
z (in)	0.01	0.16	0.88	1.02	0.25	0.01
θ_L (deg)	44.5	41.1	36.9	51.3	50.4	45.5
Φ (deg)	180.0	154.2	26.7	0.4	137.5	180.0
h (in)	0.16	0.18	0.24	0.24	0.20	0.16

To see if the required phase coverage is achievable for different local incident angles θ_L with our dielectric cylinders, we simulate the phase shift as a function of both local incident angle and cylinder height. The phase shift in Fig. 2.4 is simulated using the unit cell in Fig. 2.2 with periodic boundary condition in x and y directions. By both varying height h and local incident angle θ_L for a frequency of 4.15 GHz, we obtain the phase shift plot of Fig. 2.4.

As can be seen from Fig. 2.4, the phase varies over more than 2π for the entire range of local incident angles required ($35° \leq \theta \leq 55°$). By interpolating the $\theta_L - h$ diagram in Fig. 2.4, we obtain the height needed for each dielectric cylinder, *i.e.*, $h(x)$. We discretize the phase distribution with 25 cylinders.

To compute the phase shift from a single metasurface element we assume that its response can be approximated by that of an infinitely periodic array. In our case, this is a good approximation because cylinders are made of a high permittivity material that concentrates the field and, as a result, the coupling between unit cells is weak enough to consider each unit cell as independent. Furthermore, since the phase gradients are small, neighboring cylinders are of comparable dimensions. Thus, the total field of the whole system can be treated as the superposition of the response of each unit cell as follows from Huygens principle.

2.4 Full Cloak Simulation

Based on the design from the previous section, we model the structure shown in Fig. 2.2 using a commercial full-wave solver [29]. Figure 2.5 show the reflection pattern (electric field) for the ground plane (5-(a)), the Gaussian scatterer (5-(b)), the Gaussian scatterer covered by the cloaking cylinder metasurface (5-(c)), and a metasurface using a more continuously varying refractive index satisfying the phase gradient (5-(d)). Figure 2.5(e) is a phase plot along the equi-phase line L in Fig. 2.5(a)-(d).

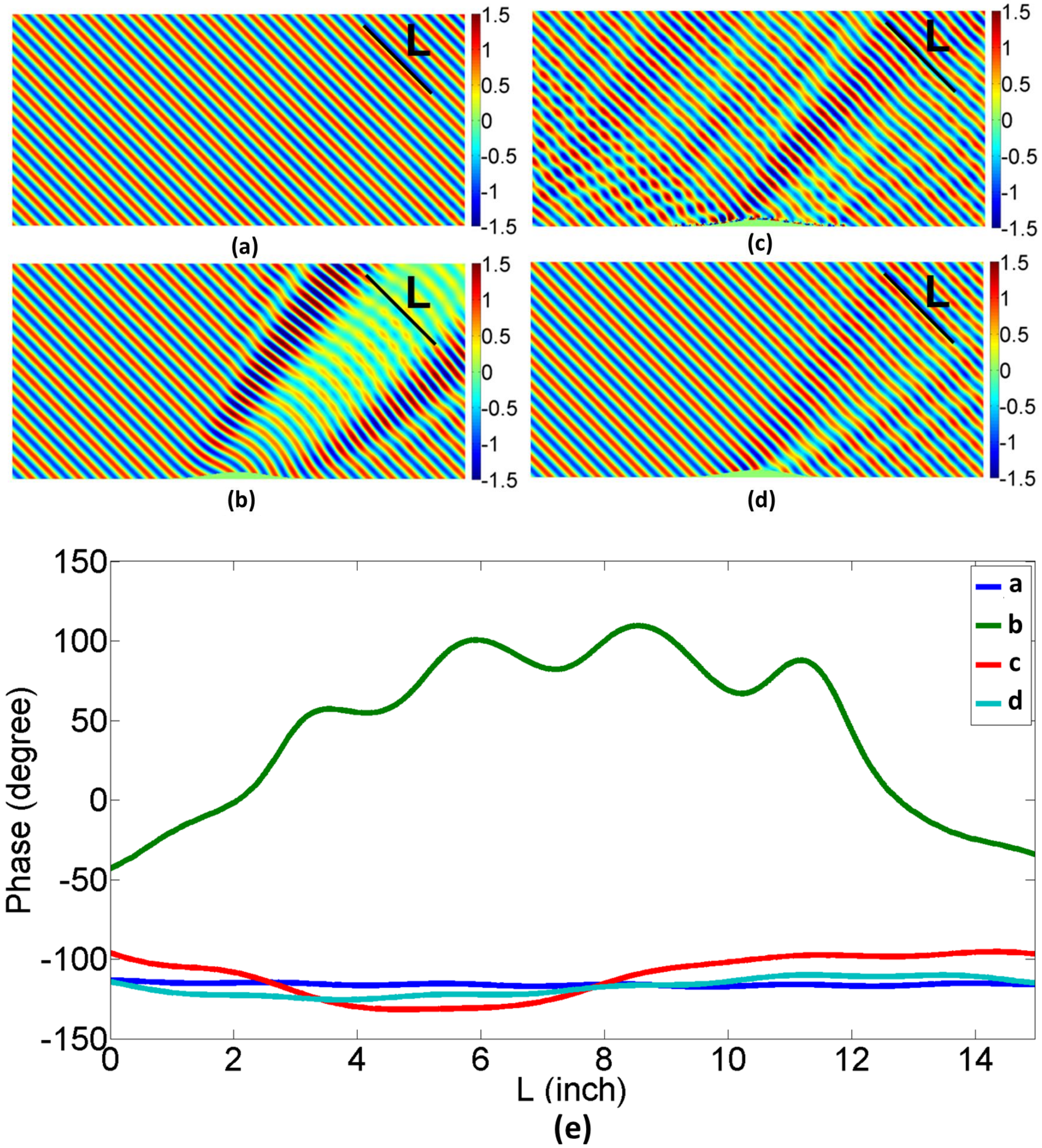

(a) (b) (c) (d) (e)

Figure 2.5: (a) Electric field reflection pattern for a flat ground plane. (b) Electric field reflection pattern for a Gaussian scatterer. (c) Electric field reflection pattern for a Gaussian scatterer with dielectric cylinders cloaking metasurface. (d) Electric field reflection pattern for a Gaussian scatterer with more continuously varying refractive index. (e) Phase plot along the equi-phase line L in (a)-(d).

In Fig. 2.5(b), we observe the expected distortion due to the scatterer and in Fig. 2.5(c) its correction as provided by the metasurface. It is clear that the metasurface fixes the distortion considerably and the reflection pattern is that of a quasi-plane wave. Even with just about two cylinders per wavelength, we achieve a very good level of reflection pattern. The result can also be further improved by increasing the number of unit cells per wavelength as shown by the field pattern while using a more continuously varying refractive index (Fig. 2.5(d)). Other distortions are due to the fact that the metasurface correct the local phase and is cloaking only in the far field and to the use of a hypothetical plane wave of infinite extent filling all space in our simulations.

It is worth noticing that the phase distribution needed on the metasurface will change with different global incident angle θ_G and our metasurface is designed for θ_G = 45 degrees. We have performed an angular sensitivity study. Δphase(degree) in Fig. 2.6 is the phase difference on the equi-phase line L between the phase reflected by our metasurface (designed for 45 degree) and phase expected from a flat ground plane for different global incident angles. Reasonable performances are obtained for $\theta_G \sim 45 \pm 6$ i.e for θ_G between 39 and 51 degrees where the phase advance/delay is less than 3% of a period. To obtain wider global incident angle range, reconfigurable metasurface could be designed by adding active elements to expand the applicability of the work.

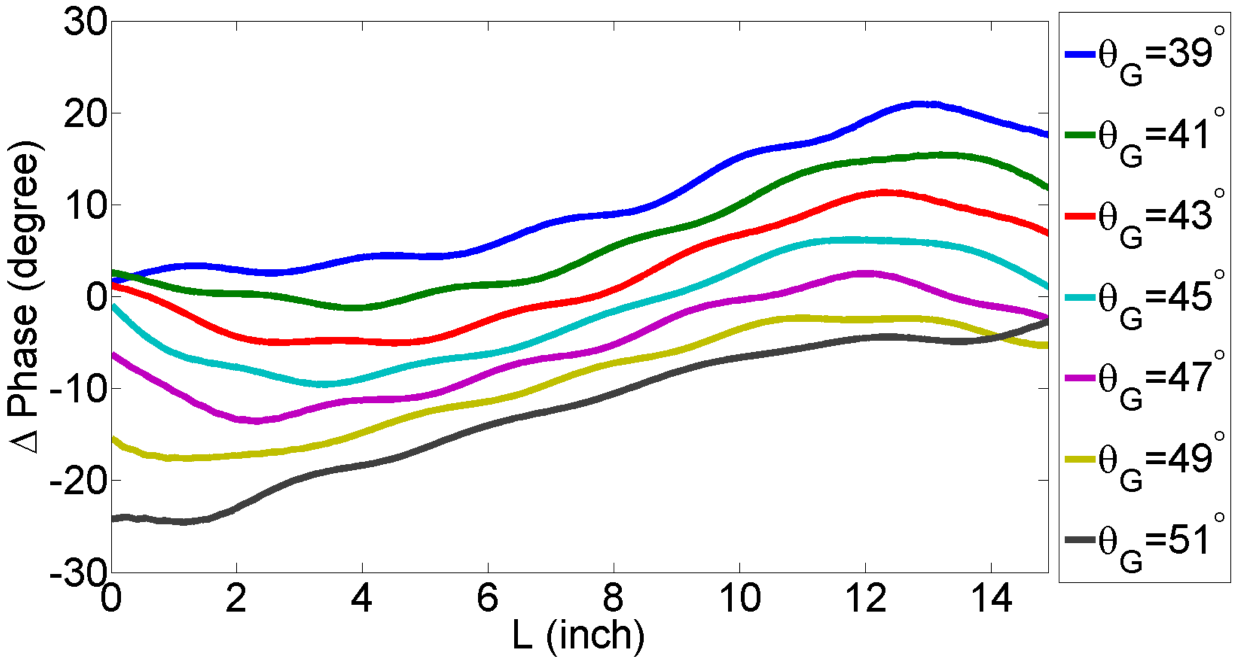

Figure 2.6: Phase difference on the equi-phase line L between the phase reflected by our metasurface (designed for 45 degree) and phase expected from a flat ground plane for different global incident angles.

Further sensitivity analysis can be carried out by computing the partial derivatives with respect to x, θ, and k_0.

$$\mathrm{d}\Phi(x,\theta,k_0)=\frac{\partial\Phi}{\partial x}\mathrm{d}x+\frac{\partial\Phi}{\partial\theta}\mathrm{d}\theta+\frac{\partial\Phi}{\partial k_0}\mathrm{d}k_0 \qquad (6)$$

From Eqs. 5-6, we can draw three conclusions. First, the phase distribution sensitivity with respect to frequency is independent of frequency itself. There are thus no special considerations for different frequency ranges. Second, the phase distribution sensitivity with respect to global incident angle is maximum for grazing incidence ($\theta = \pi/2$). It is thus harder to cloak a scatterer for large angles of incidence. Finally, the phase distribution sensitivity with respect to position is, somewhat surprisingly, independent of position itself for large slopes.

All of this implies that a cloaking device can work for a large range of global incident angles and be broadband if the phase distribution on the metasurface is linear with respect to frequency and cosine-like with respect to global incident angle.

2.5 Conclusion

In this paper, we have reported an extremely thin dielectric metasurface carpet cloak. The geometrical scheme presented is general and can be used for any surface of class C^1 and for frequencies up to the visible. The proposed design flow chart gives a powerful and easy to use recipe to design metasurface cloaks for a given geometry. A specific design has been presented and cloaking performance has been shown to be robust with respect to surface discretization. The observed wavefronts reflected from the proposed metasurface have been shown to be quasi-planar, with little to no distortion. With this design, any observer will just see a flat ground plane and the scatterer will be invisible and thus effectively cloaked. We have also shown that despite being designed for 45 degrees, accepting a phase advance/delay of 3% of the period, results in an angular bandwidth of ± 6 degrees. Moreover, this approach of bending electromagnetic waves with metasurfaces can be used not only for carpet cloaks but also for light focusing to make flat optics devices such as thin solar concentrators, quarter-wave plates, and spatial light modulators. Making these surfaces reconfigurable, we expect ideas proposed here to find applications in flexible devices.

Chapter 2, in part, is a reprint of the material as it appears in L.-Y. Hsu, T. Lepetit, B. Kanté, “Extremely Thin Dielectric Metasurface for Carpet Cloaking,” Progress in Electromagnetics Research, 152, 33–40 (2015). The dissertation author was the primary researcher and author of this paper.

2.6 References

1. J. B. Pendry, D. Schurig, and D. R. Smith, “Controlling electromagnetic fields,” *Science* 312, 1780-1782 (2006).

2. U. Leonhardt, “Optical conformal mapping,” *Science* 312, 1777-1780 (2006).

3. D. Schurig, J. J. Mock, B. J. Justice, S. A. Cummer, J. B. Pendry, A. F. Starr, and D. R. Smith., “Metamaterial electromagnetic cloak at microwave frequencies,” *Science* 314, 977-980 (2006).

4. J. Li, and J. B. Pendry, “Hiding under the carpet: A new strategy for cloaking,” *Phys. Rev. Lett.* 101, 203901 (2008).

5. R. Liu, C. Ji, J. J. Mock, J. Y. Chin, T. J. Cui, and D. R. Smith, “Broadband ground-plane cloak,” *Science* 323, 366-369 (2009).

6. J. Valentine, J. Li, T. Zentgraf, G. Bartal, and X. Zhang, “An optical cloak made of dielectrics,” *Nat. Mat.* 8, 568-571 (2009).

7. E. Kallos, C. Argyropoulos, and Y. Hao, “Ground-plane quasicloaking for free space,” *Phys. Rev. A* 79, 063825 (2009).

8. W. X. Jiang, T. J. Cui, X. M. Yang, Q. Cheng, R. Liu, and D. R. Smith, “Invisibility cloak without singularity,” *Appl. Phys. Lett.* 93, 194102 (2008).

9. U. Leonhardt and T. Tyc, “Broadband invisibility by non-euclidean cloaking,” *Science* 323, 110–112 (2009).

10. W. Cai, U. K. Chettiar, A. V. Kildishev, and V. M. Shalaev, “Optical cloaking with metamaterials,” *Nat. Phot.* 1, 224–227 (2007).

11. A. Alu and N. Engheta, “Multifrequency optical invisibility cloak with layered plasmonic shells,” *Phys. Rev. Lett.* 100, 113901 (2008).

12. B. Kanté, D. Germain, and A. de Lustrac, “Experimental demonstration of a nonmagnetic metamaterial cloak at microwave frequencies,” *Phys. Rev. B* 80, 201104 (2009).

13. H. Chen and C.T. Chan, “Transformation media that rotate electromagnetic fields,” *Appl. Phys. Lett.* 90, 241105 (2007).

14. M. Rahm, D. Schurig, D. A. Roberts, S. A. Cummer, D. R. Smith, and J. B. Pendry, “Design of electromagnetic cloaks and concentrators using form-invariant coordinate transformations of Maxwells equations,” *Photon. Nanostruct. Fundam. Appl.* 6, 87-95 (2008).

15. W. X. Jiang, T. J. Cui, Q. Cheng, J. Y. Chin, X. M. Yang, R. Liu, and D. R. Smith, “Design of arbitrarily shaped concentrators based on conformally optical transformation of nonuniform rational B-spline surfaces,” *Appl. Phys. Lett.* 92, 264101 (2008).

16. A. Greenleaf, Y. Kurylev, and M. Lassas, “Electromagnetic wormholes and virtual magnetic monopolesfrom metamaterials,” *Phys. Rev. Lett.* 99, 183901 (2007).

17. A. V. Kildishev and E. E. Narimanov, “Impedance-matched hyperlens,” *Opt. Lett.* 32, 3432–3434 (2007).

18. S. O’Brien and J. B. Pendry, “Magnetic activity at infrared frequencies in structured metallic photonic crystals,” *J. Phys. Condens. Matter* 14, 6383–6394 (2002).

19. J. Zhou, T. Koschny, M. Kafesaki, E. N. Economou, J. B. Pendry, and C. M. Soukoulis, “Saturation of the magnetic response of split-ring resonators at optical frequencies,” *Phys. Rev. Lett.* 95, 223902 (2005).

20. A. Ishikawa, T. Tanaka, and S. Kawata, “Negative magnetic permeability in the visible light region,” *Phys. Rev. Lett.* 95, 237401 (2005).

21. B. Kanté, A. de Lustrac, J.-M. Lourtioz, and F. Gadot, “Engineering resonances in infrared metamaterials,” *Opt. Express*, 16, 6774-6784 (2008).

22. C. L. Holloway, E. F. Kuester, J. A. Gordon, J. O’Hara, J. Booth, and D. R. Smith., “An overview of the theory and applications of metasurfaces: The two dimensional equivalents of metamaterials,” *IEEE Antennas Propagat. Mag.* 54, 10–35 (2012).

23. B. Kanté, J.-M. Lourtioz, and A. de Lustrac, “Infrared metafilms on a dielectric substrate,” *Phys. Rev. B* 80, 205120 (2009)

24. N. Yu, P. Genevet, M. A. Kats, F. Aieta, J.-P. Tetienne, F. Capasso, and Z. Gaburro, “Light propagation with phase discontinuities: Generalized laws of reflection and refraction,” *Science* 334, 333–337 (2011)

25. N. Yu and F. Capasso, “Flat optics with designer metasurfaces,” Nature Materials 13, 139–150 (2014)

26. K. Zhang, X. Ding, L. Zhang and Q. Wu, “Anomalous three-dimensional refraction in the microwave region by ultra-thin high efficiency metalens with phase discontinuities in orthogonal directions,” New Journal of Physics. 16(10), 103020, (2014)

27. J. Zhang, Z. L. Mei, W. R. Zhang, F. Yang and T. J. Cui, “An ultrathin directional carpet cloak based on generalized Snell's law,” Appl. Phys. Lett. 103, 151115 (2013)

28. L. Zou, M. L.-G., W. Withayachumnankul, C. M. Shah, A. Mitchell, M. Bhaskaran, S. Sriram, R. Oulton, M. Klemm, and C. Fumeaux, “Spectral and angular characteristics of dielectric resonator metasurface at optical frequencies,” Appl. Phys. Lett. 105, 191109 (2014)

29. CST Studio Suite 2014, http://www.CST.com.

Chapter 3

Broadband and linear polarization metasurface carpet cloak in the visible

In the past few years, carpet cloaking attracted interests because of its feasibility at optical frequencies and potential in stealth technologies. Metasurfaces have been proposed as a method to engineer ultra-thin carpet cloaking surfaces due to their abilities to manipulate wavefronts, polarization, and phase at subwavelength scale. However, achieving broadband carpet cloaking with a significant bandwidth is one of the key remaining challenges for metasurface designs. To date, broadband carpet cloaking based on metasurfaces has not been achieved and operation has been limited to discrete wavelengths. Here, we propose and numerically demonstrate a novel metasurface design for broadband carpet cloaking with linear polarization at visible wavelengths from 650 nm to 800 nm. Our proposed method is a promising approach for broadband structured interfaces.

3.1 Introduction

In the past few years, metasurfaces have been investigated as potential alternatives for bulky integrated optical free space components due to the simplicity of their manufacturing.

Metasurfaces are subwavelength nanostructured devices that enable the control of optical wavefronts, polarization, and phase. A large variety of flat optical components, including planar lenses [1-13], solar concentrators [14], polarizers [15], thin absorbers [16-17], sensors [18-19], or carpet cloaks [20-27] have been demonstrated. However, the working bandwidth of currents metasurfaces, despite significant effort, is limited by not only the intrinsic dispersion of optical properties of materials but also their design principle. Although, multiple wavelengths and relatively broadband carpet cloaking have been recently reported in [28-33], the proposed devices are so far either limited to circular polarization, discrete wavelength, or continuous bandwidth in the infrared [34].

Controlling material dispersion has been recognized as a linchpin to broadening optical bandwidth of components. The ability to control the dispersion is, thus, a highly desired property for the medium supporting optical modes. Therefore, minimizing the dispersion of materials is the main challenge in optical components specifically for broadband carpet cloaking. Conventional metasurfaces proposed for large band operation are based on optical waveguides made of a high-index core surrounded by low-index claddings which limit currents metasurfaces applications to relatively small bandwidth governed by the dispersion of the waveguides. To overcome these limitations, we propose an alternative solution that consists in using slot waveguides as they can confine light in the lossless material (air) compared to systems guiding light in high index materials, usually dispersive at higher frequencies.

By using appropriate geometrical parameters, we designed and simulated a broadband metasurface carpet cloak with linear polarization in the visible range from 650 nm to 800 nm. To our knowledge, this is the first time such broadband metasurface carpet cloak with linear polarization is proposed in the visible. This new design enhances the capability of metasurfaces. The presented results may enable broadband metasurfaces for various applications and devices.

3.2 Design Principle

The carpet surface under which cloaking is achieved can be described by a function z(x,y). To illustrate the design strategy, we consider a bump surface (invariant in y) that is described by a Gaussian function. An arbitrary shaped object can always be hidden below a surface of this form.

$$z(x) = Ae^{-\frac{x^2}{\sigma^2}} \tag{1}$$

To achieve the cloaking function, the phase distribution Φ(x) required to compensate the phase advance/delay due to the bump is given by [23]

$$\Phi(x,f) = -2k_0 z(x) cos\theta_G + r(f) = -\frac{4\pi f}{c} z(x) cos\theta_G + r(f)$$

$$\Phi(x,f) = m(x)f + r(f), where\ m(x) = -\frac{4\pi}{c} z(x) cos\theta_G \tag{2}$$

where r(f) is defined by the flat surface, f is the frequency of the incident wave, x is the position on bump and m is the slope of phase equation with respect to frequency f and θG represents the incidence angle. By providing the appropriate phase distribution in equation 2, we can make the bump look like a flat ground plane using all dielectric metasurfaces. Equation 2 implies that a cloaking device can be broadband if the phase distribution on the metasurface is linear with respect to frequency (f). Secondly, the slope is different for different position (x) but r(f) is the same for different positions while it can be different for different frequency (f). To simplify the equation, we choose the phase reference as r(f), then the phase-shift (Φs) distribution required for a broadband metasurface cloaking becomes:

$$\Phi_s(x,f) = \Phi(x,f) - \mathrm{r}(f) = m(x)f \tag{3}$$

To demonstrate broadband carpet cloaking, we design a metasurface carpet cloak for a Gaussian bump where A = 360 nm, σ = 2.4 μm, from 375 THz to 460 THz for an incident angle (θG) 45°. Figure 3.1(a) presents 2D plot for phase-shift (Φs) as function of position and frequency. Figure 3.1(b) presents phase-shift profiles for different frequencies. They are bump-shape curves and the phase-shift gradient with position increases with frequency. Figure 3.1(c) present phase-shift frequency profiles at different positions (x). The phase shifts are linear with respect to the frequency and the phase-shift gradient increases with position.

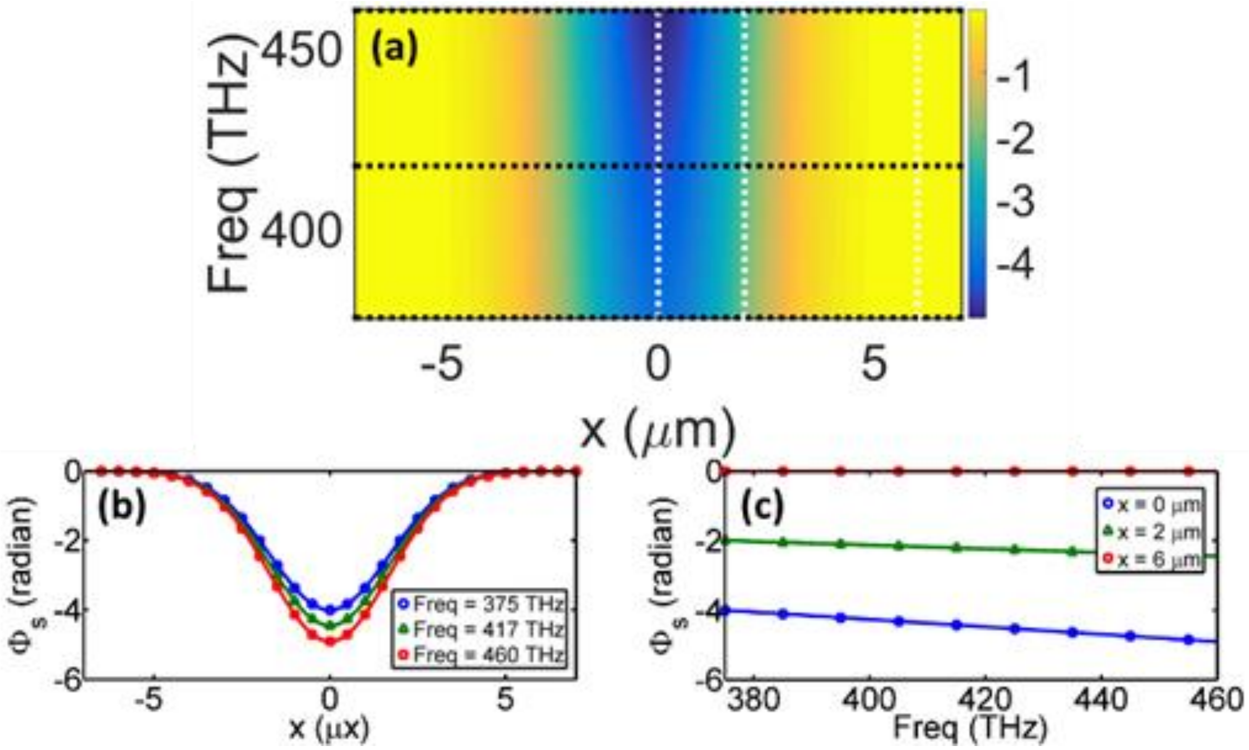

Figure 3.1: (a) Required phase-shift profile (in radians) at specified frequencies for a broadband metasurface carpet cloaking. (b) Phase-shift with position. (c) Phase-shift with frequency at specified positions.

To design a broadband carpet cloak, we propose to use a slot waveguide as building block in order to provide a linear phase with respect to frequency. The slot waveguide consists of two high index ridges (Si_3N_4), separated by a narrow low index gap (air). Due to such refractive index discontinuity, this structure allows one of the propagating modes to confine its energy within the slot region [35]. The advantage of using slot waveguides as a unit cells is to mitigate the material dispersion by confining the mode in air gap and enables subwavelength confinement of the light.

Figure 3.2(a) presents the schematic of the carpet cloaking design. The incident wave is TM polarized with the magnetic field H field along the y direction and with an incident angle θ_G presented on the left. Figure 3.2(b) presents the geometry of the unit cell of the metasurface. The period (p) of the metasurface array is 280 nm, the width (w) of the air gap varies from 80nm to 200nm. The metal layer is silver with a thickness of 100 nm (h_{Silver}), the spacer is SiO2 with thickness 350 nm (h_{SiO2}), and the slot waveguide consists of two ridges of Si_3N_4 with a thickness 350 nm (h_{Si3N4}) separated by an air gap. Figure 3.2(c) shows the normalized electrical field at 409 THz with w = 80 nm and θ_L = 45°. One can observe that the highest field confinement is in the air gap.

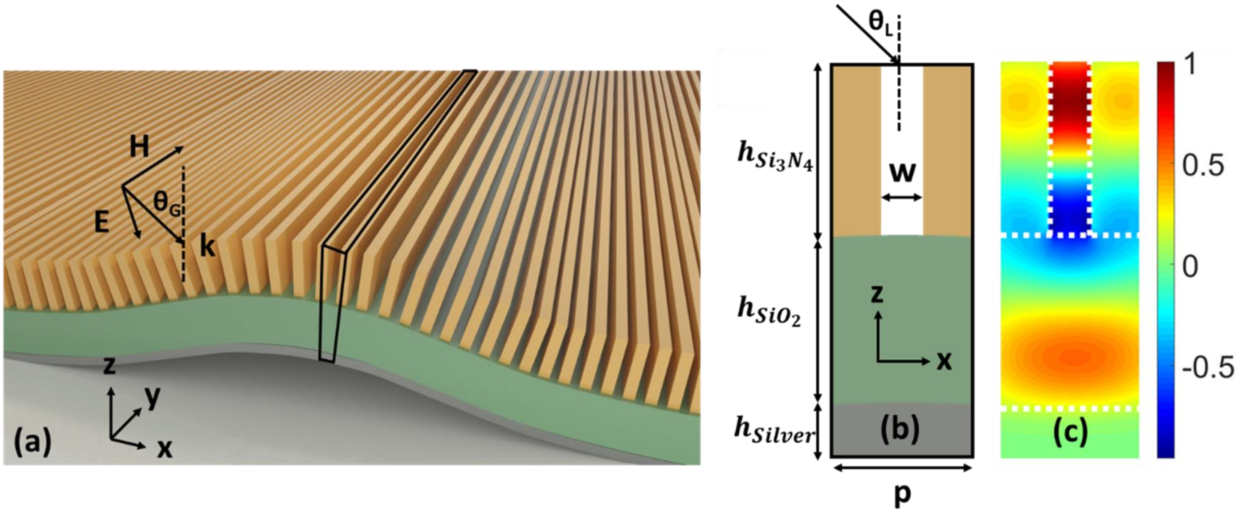

Figure 3.2: (a) Schematic of the carpet cloaking system. The incident wave is TM polarized with the magnetic field H along the y direction and with an incident angle θ_G. (b) The considered geometry of the unit cell of the metasurface. The period (p) of the metasurface array is 280 nm, the width (w) of the air gap is ranging from 80 nm to 200 nm. The metal layer is silver with a thickness of 100 nm (h_{Silver}), the spacer is SiO2 with thickness 350 nm (h_{SiO_2}), and the slot waveguide consists of two ridges of Si3N4 with thickness 350 nm ($h_{Si_3N_4}$) separated with an air gap. (c) Normalized electric field at 409 THz with w = 80 nm and θ_L = 45°.

The design flowchart is as shown in Fig. 3.3, from the bump geometry z(x) [figure 3.3(a)], we compute the local incident angle $\theta_L(x)$ [figure 3.3(b)], and then the phase distribution $\Phi_s(x, f)$ from Eq. 3. Last, for each width at position x and local incident angle $\theta_L(x)$, we simulated the phase respect with frequency as shown in figure 3.3c. Then, we calculated phase difference between simulation and the target. We optimized the width to minimize the sum of square of phase error between simulation and the required target phase. Figure 3.3(c) represents the fitting result at the center of the metasurface (x = 0). The maximum error is less than 20° and it happens at about 384 THz. Figure 3.3(d) is the fitted width with position. The width is not symmetric with the center of the bump (x=0) because the local incident angle is not symmetric with respect to the center of the bump (x=0).

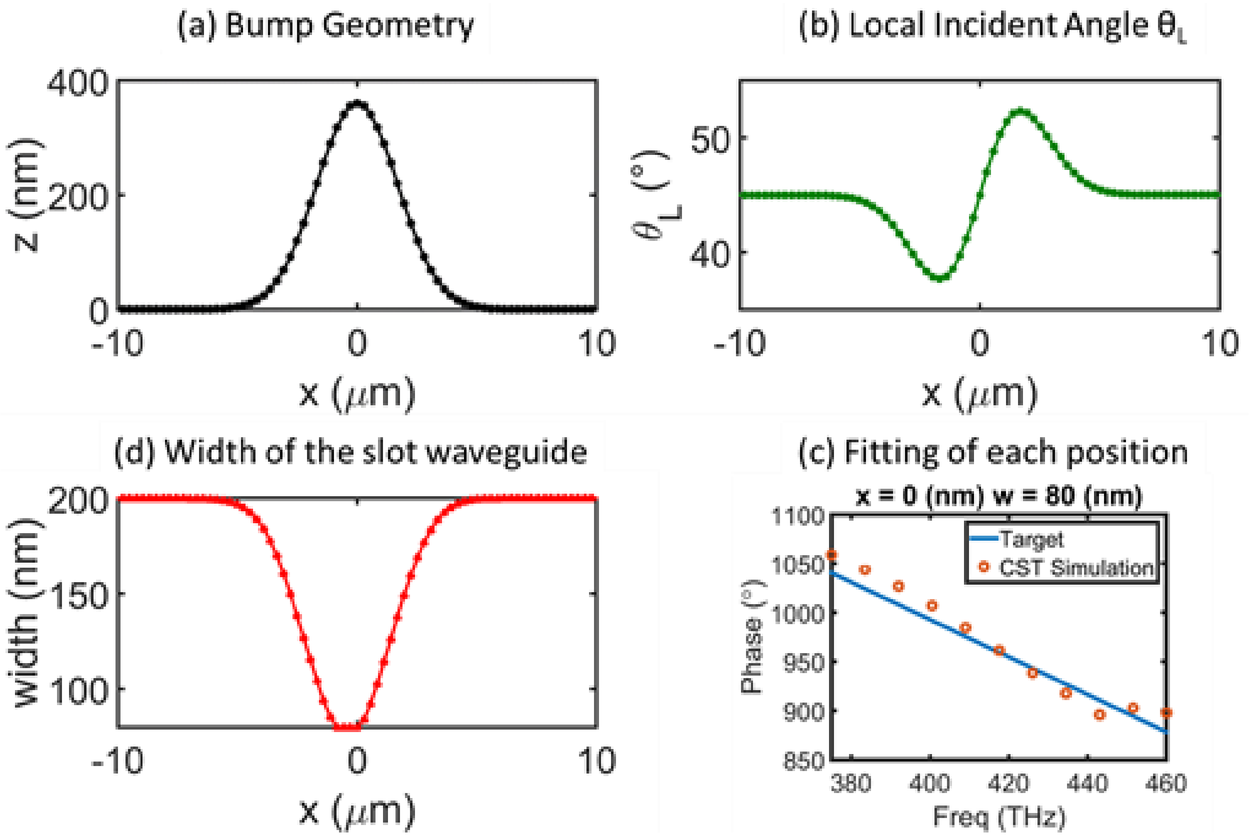

Figure 3.3: The design flowchart. (a) Bump geometry as function of the position (b) Local incident angle as function of the position. (c) The fitting result at x=0 (center of the bump). For each position, we optimized the width of the slot waveguide in order to minimize the square of phase error between simulation and the required phase (target). (d) Width of the slot waveguide as a function of the position.

3.3 Results

Figure 3.4 presents the fitting results at different positions on the metasurface. The blue line is the target phase and the orange circles are simulation results. The average error between numerical simulations and target is about 4°. It is important to mention that although the target phase is symmetric with respect to the center of the bump(x=0), the width of the slot waveguide is not symmetric with respect to the center of the bump (x=0) at oblique incidence. For example, the local incident angle is 37.67° at x = -1.68 μm but it is 52.33° at x = 1.68 μm.

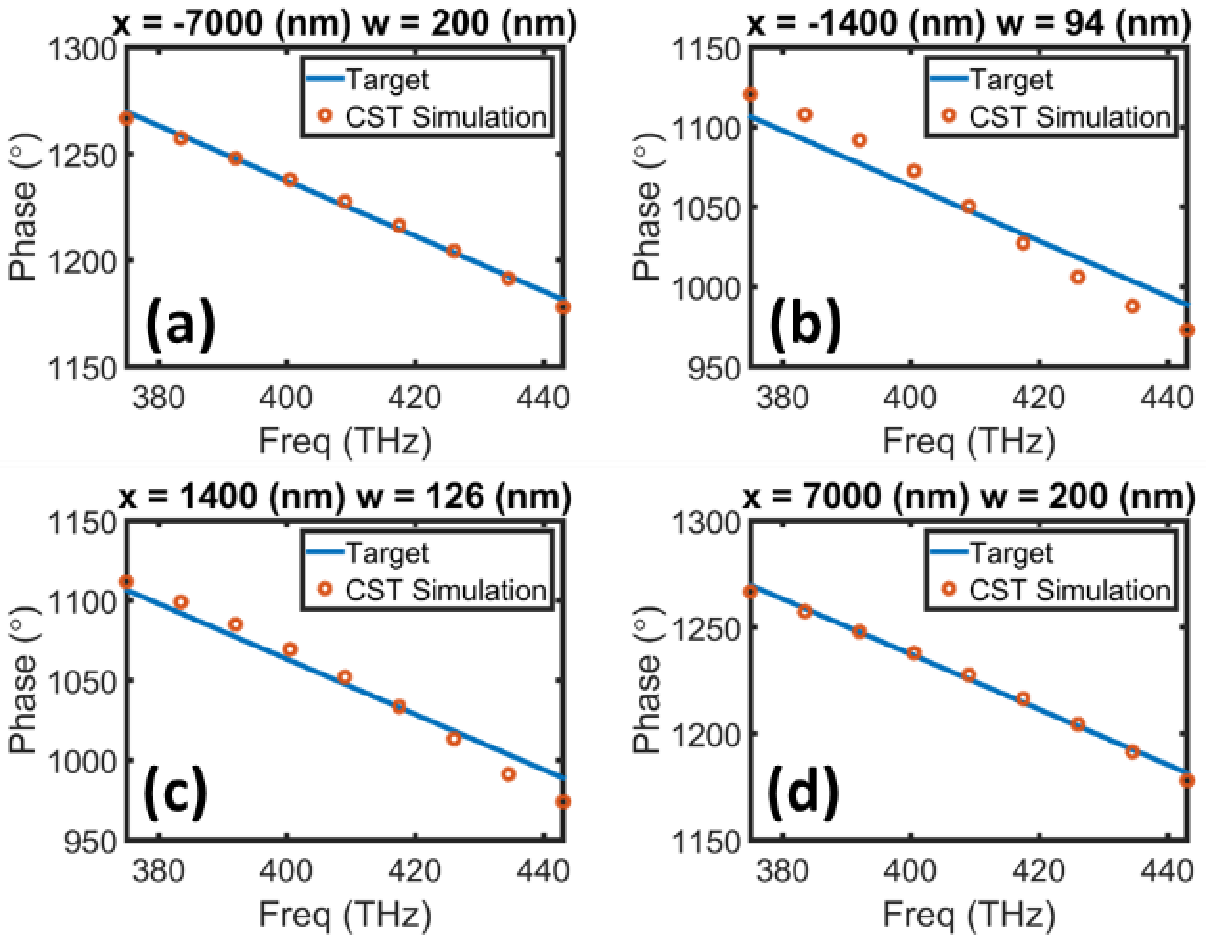

Figure 3.4: Fitting results for different positions (a) x = -7000 nm (b) x = -1400 um (c) x = -1400 nm (d) x = 7000 nm.

In order to simulate the entire structure, we used the transient solver of CST Microwave Studio. Open boundary conditions are applied to x direction and +z direction and periodic boundary condition is applied to y-direction to mimic invariance along the y-direction. The structure is illuminated at oblique incidence (θ_G=45°) from the left with a TM polarized Gaussian beam. Figure 3.5 shows the real part of electric field patterns. The columns present different frequencies (375 THz, 392 THz, 409 THz, 426 THz, 443 THz, 460 THz) and the rows present different structures such as the ground plane (a, d, g, j, m, p), the Gaussian-shaped bump (b, e, h, k, n, q), and the Gaussian-shaped bump covered with the designed metasurface (c, f, i, l, o, r). In figure 3.6, we also plot the phase along an equi-phase line (black line) in figure 3.5. As seen, the wavefronts of reflected waves is flat for the ground plane cases. However, the reflected wavefronts are bent and curved due to Gaussian-shaped bump. After we cover the bump with the metasurface, one can observe that the distortions are corrected, and the reflected wavefronts become flat again. Hence, the designed metasurfaces can properly modify the scattering of the bump in the broadband range from 375 THz (800 nm) to 460 THz (650 nm).

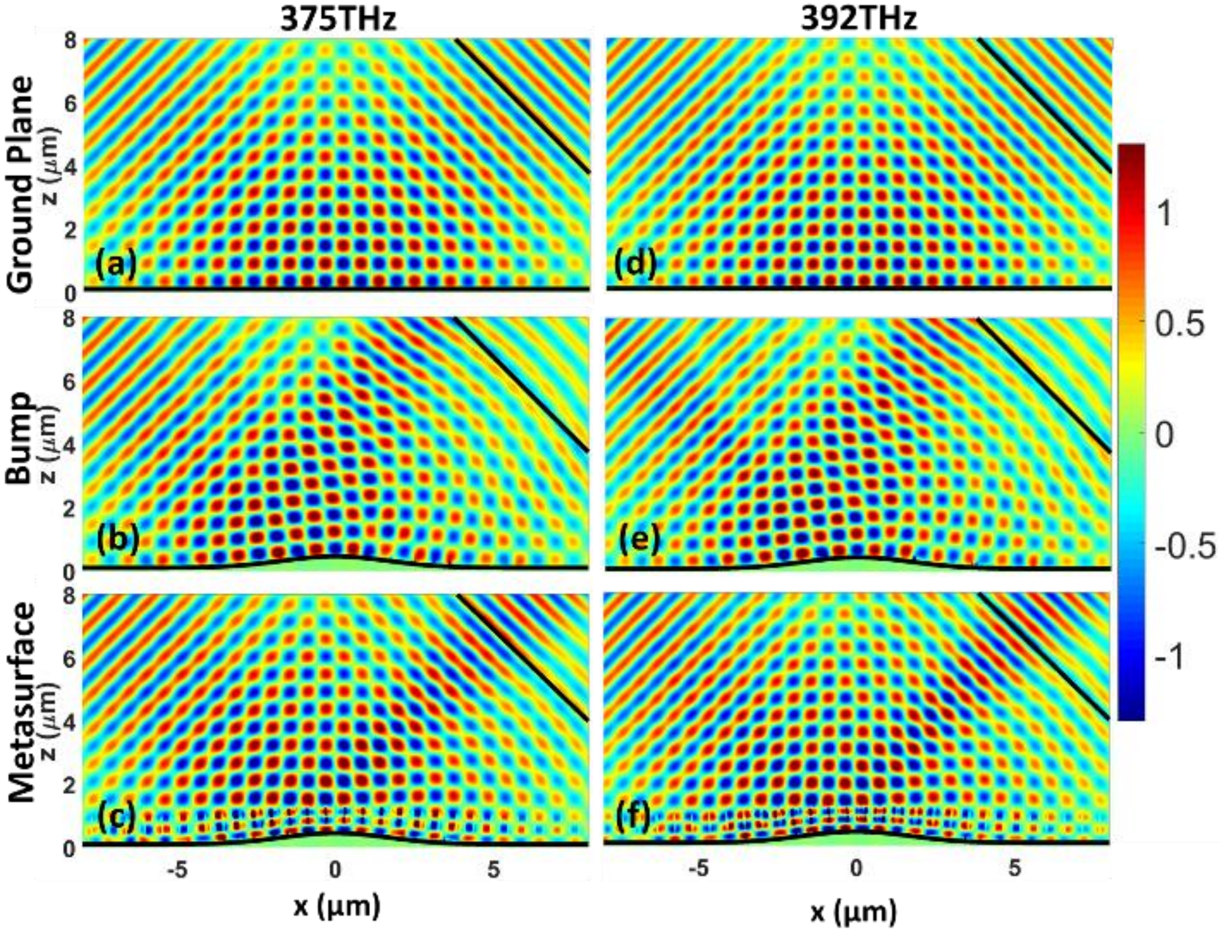

Figure 3.5: Real part of electric E field for the ground plane, bump, and metasurface at different frequencies from 375 THz to 460 THz. The columns present different frequencies (375 THz, 392 THz, 409 THz, 426 THz, 443 THz, 460 THz) and the rows present different structures such as the ground plane (a, d, g, j, m, p), the Gaussian-shaped bump (b, e, h, k, n, q), and the Gaussian-shaped bump covered by the designed metasurface (c, f, i, l, o, r).

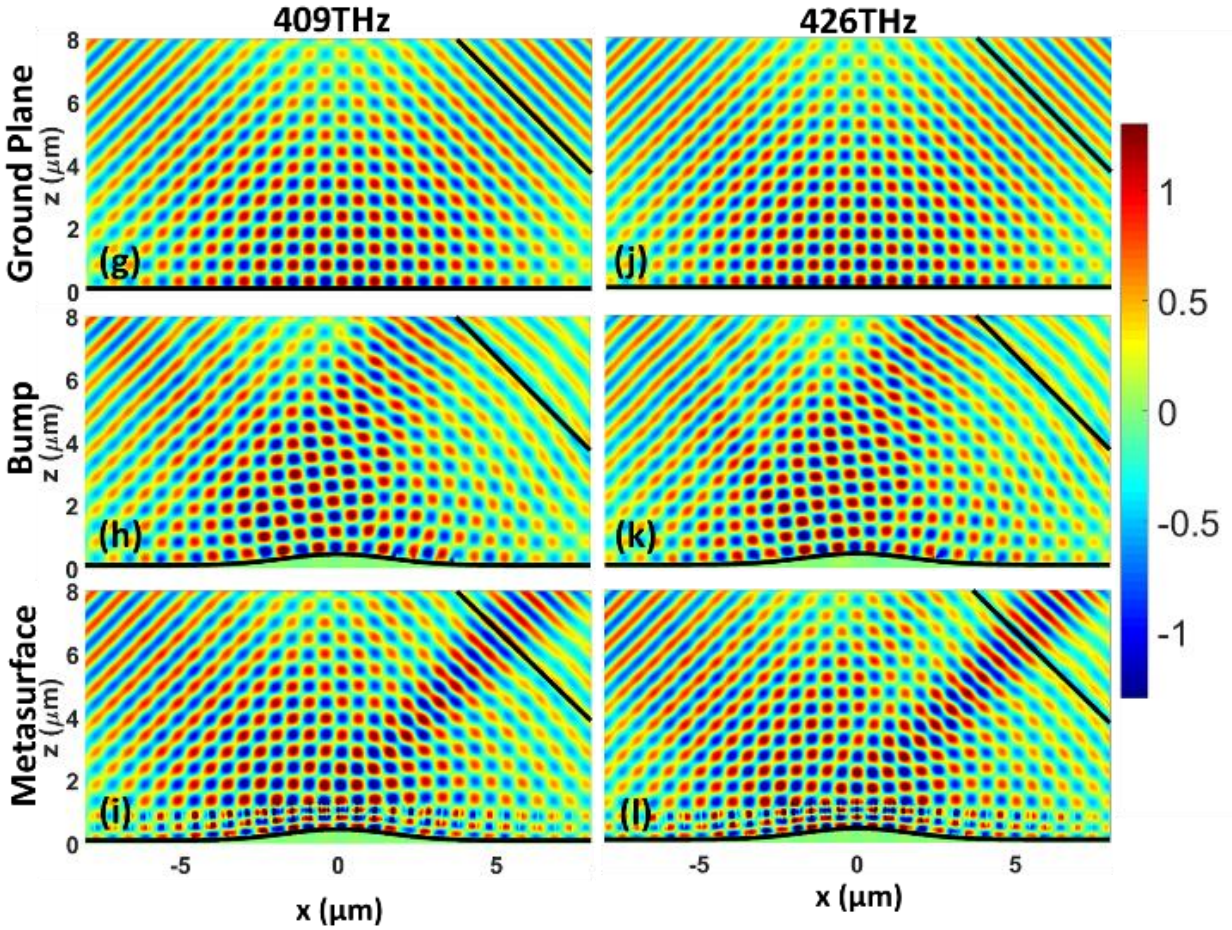

Figure 3.5: Real part of electric E field for the ground plane, bump, and metasurface at different frequencies from 375 THz to 460 THz. The columns present different frequencies (375 THz, 392 THz, 409 THz, 426 THz, 443 THz, 460 THz) and the rows present different structures such as the ground plane (a, d, g, j, m, p), the Gaussian-shaped bump (b, e, h, k, n, q), and the Gaussian-shaped bump covered by the designed metasurface (c, f, i, l, o, r), continued.

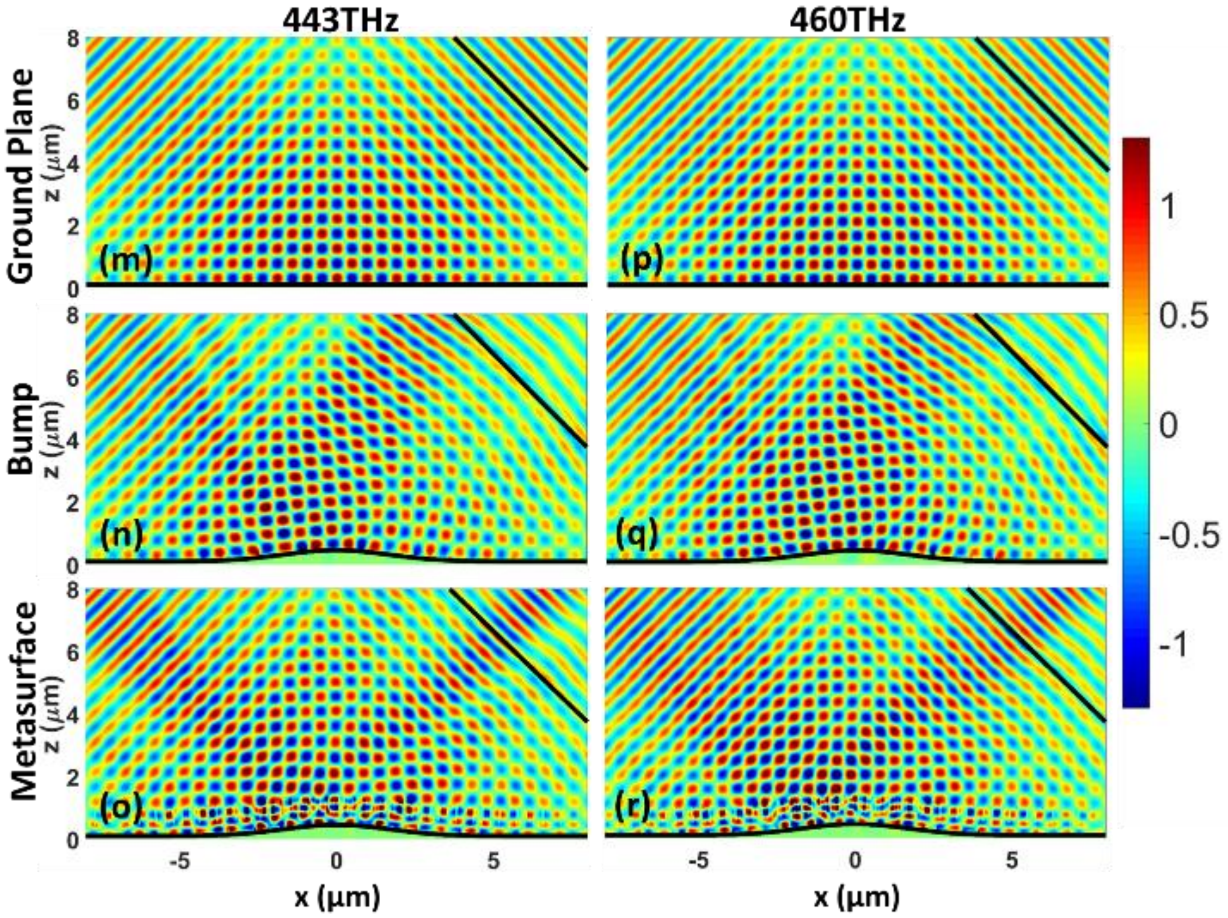

Figure 3.5: Real part of electric E field for the ground plane, bump, and metasurface at different frequencies from 375 THz to 460 THz. The columns present different frequencies (375 THz, 392 THz, 409 THz, 426 THz, 443 THz, 460 THz) and the rows present different structures such as the ground plane (a, d, g, j, m, p), the Gaussian-shaped bump (b, e, h, k, n, q), and the Gaussian-shaped bump covered by the designed metasurface (c, f, i, l, o, r), continued.

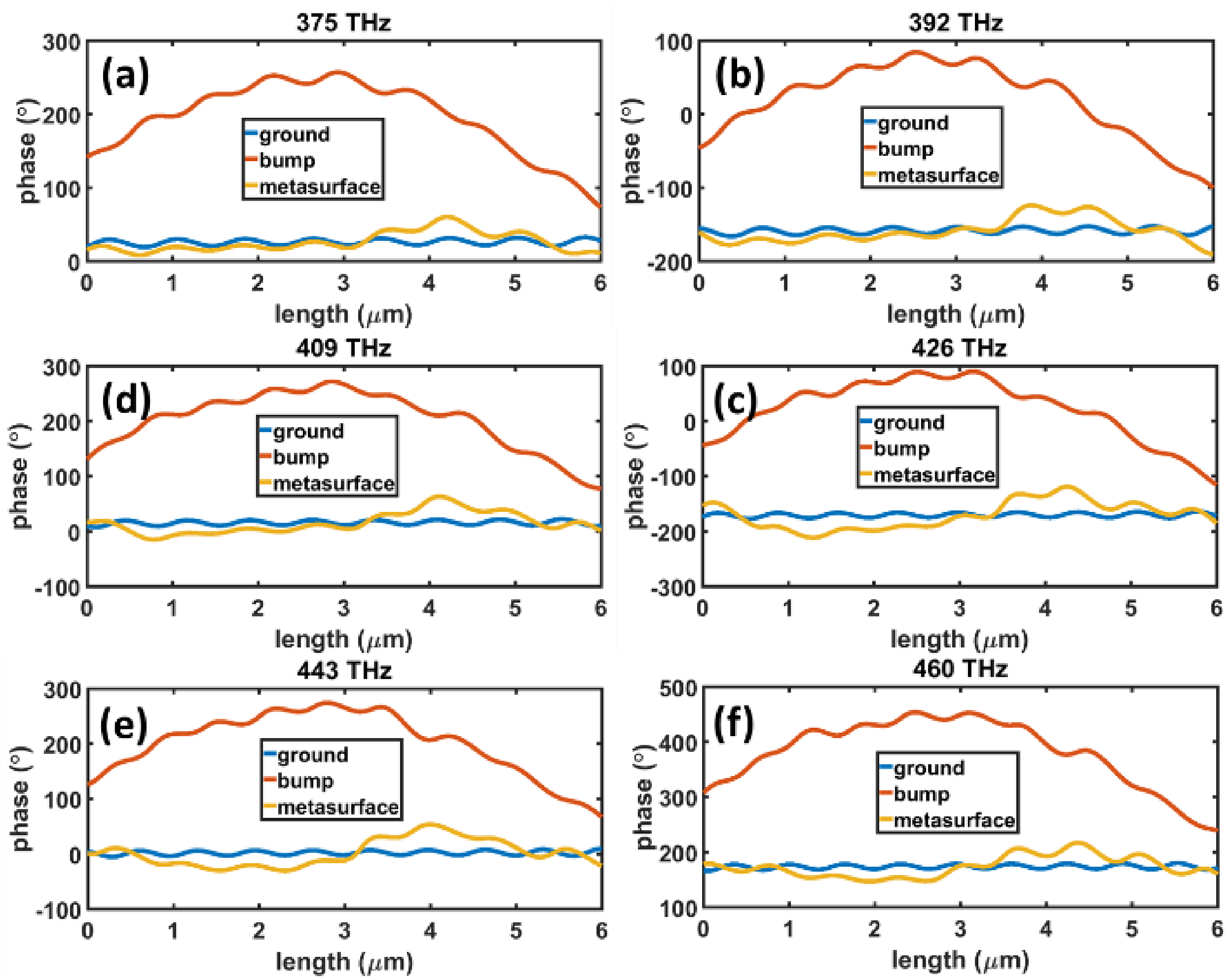

Figure 3.6: Phase profile of electric E field in figure 3.5 (black dish lines) at different frequencies from 375 THz to 460 THz. (a) 375THz (b) 392 THz (c) 409 THz (d) 426 THz (e) 443 THz (f) 460 THz.

3.4 Conclusion

We have proposed and numerically demonstrated a new and simple design for broadband metasurfaces carpet cloaking with linear polarization at visible wavelengths from 650 nm to 800 nm [36]. The design consists of two high index ridges (Si_3N_4), separated by a narrow low index gap (air). Due to such refractive index discontinuity forming the slot waveguide, this structure allows one of the propagating modes to confine its energy within the slot region. The advantage of the slot waveguide is to mitigate materials dispersion by confining light in the subwavelength air gap region. The approach enables broadband operation for metasurfaces.

Chapter 3, in part, is a reprint of the material as it appears L.-Y. Hsu, A. Ndao, B. Kanté, "Broadband and linear polarization metasurface carpet cloak in the visible," Optics Letters 44 (12), 2978-2981 (2019). The dissertation author was the primary researcher and author of this paper.

3.5 Reference

1. F. Falcone, T. Lopetegi, M. A. G. Laso, J. D. Baena, J. Bonache, M. Beruete, R. Marqués, F. Martín, and M. Sorolla, "Babinet Principle Applied to the Design of Metasurfaces and Metamaterials," Phys. Rev. Lett. 93(19), 197401 (2004).

2. Yu, N., P. Genevet, M. A. Kats, F. Aieta, J.-P. Tetienne, F. Capasso, and Z. Gaburro, "Light Propagation with Phase Discontinuities: Generalized Laws of Reflection and Refraction," Science, 334, 333-337 (2011).

3. A. V. Kildishev, A. Boltasseva, and V. M. Shalaev, "Planar Photonics with Metasurfaces," Science 339(6125),1232009 (2013).

4. N. Yu, and F. Capasso, "Flat optics with designer metasurfaces," Nat. Mater. 13, 139 (2014).

5. A. Arbabi, Y. Horie, M. Bagheri, and A. Faraon, "Dielectric metasurfaces for complete control of phase and polarization with subwavelength spatial resolution and high transmission," Nat. Nanotechnol. 10(11), 937–943 (2015).

6. F. Aieta, M. A. Kats, P. Genevet, and F. Capasso, "Multiwavelength achromatic metasurfaces by dispersive phase compensation," Science 347(6228), 1342–1345 (2015).

7. L. Hsu, M. Dupré, A. Ndao, J. Yellowhair, and B. Kanté, "Local phase method for designing and optimizing metasurface devices," Opt. Express 25(21), 24974–24982 (2017).

8. R. Paniagua-Domínguez, Y. F. Yu, E. Khaidarov, S. Choi, V. Leong, R. M. Bakker, X. Liang, Y. H. Fu, V. Valuckas, L. A. Krivitsky, and A. I. Kuznetsov, "A Metalens with a Near-Unity Numerical Aperture," Nano Lett. 18(3), 2124–2132 (2018).

9. P. Lalanne and P. Chavel, "Metalenses at visible wavelengths: past, present, perspectives," Laser Photonics Rev. 3(3), 1600295 (2017).

10. J. Ha, A. Ndao, L. Hsu, J.-H. Park, B. Kante, “Planar dielectric cylindrical lens at 800 nm and the role of fabrication imperfections,” Opt. Express 26 (18), 23178-23184 (2018).

11. M. Dupré, L. Hsu, B. Kanté, “On the design of random metasurface based devices,” Sci. Rep. 8 (1), 7162 (2018).

12. T. Chen, A. Y. Zhu, V. Sanjeev, M. Khorasaninejad, Z. Shi, E. Lee, and F. Capasso, “A broadband achromatic metalens for focusing and imaging in the visible,” Nat. Nanotechnol.(3), 220–226 (2018).

13. S. Wang, P. C. Wu, V. C. Su, Y. C. Lai, M. K. Chen, H. Y. Kuo, B. H. Chen, Y. H. Chen, T. T. Huang, J. H. Wang, R. M. Lin, C. H. Kuan, T. Li, Z. Wang, S. Zhu, and D. P. Tsai, “A broadband achromatic metalens in the visible,” Nat. Nanotechnol. 13(3), 227–232 (2018).

14. L. Hsu, M. Dupré, A. Ndao, and B. Kanté, “From parabolic-trough to metasurface-concentrator: assessing focusing in the wave-optics limit,” Opt. Lett. 42(8), 1520–1523 (2017).

15. A. Ndao, R. Salut, M. Suarez, and F. I. Baida, “Plasmonless polarization-selective metasurfaces in the visible range,” J. Opt. 20(4), 045003 (2018).

16. C. Simovski, D. Morits, P. Voroshilov, M. Guzhva, P. Belov, and Y. Kivshar, “Enhanced efficiency of light trapping nanoantenna arrays for thin-film solar cells,” Opt. Express 21(S4 Suppl 4), A714–A725 (2013).

17. W. Guo, Y. Liu, and T. Han, “Ultra-broadband infrared metasurface absorber,” Opt. Express 24, 20586-20592 (2016).

18. J.-H. Park, A. Kodigala, A. Ndao, and B. Kanté, “Hybridized metamaterial platform for nano-scale sensing,” Opt. Express 25(13), 15590–15598 (2017).

19. Y. Lee, S. J. Kim, H. Park, and B. Lee, “Metamaterials and Metasurfaces for Sensor Applications,” Sensors (Basel, Switzerland), 17(8) (2017).

20. J. B. Pendry, D. Schurig, and D. R. Smith, “Controlling electromagnetic fields,” Science 312, 1780-1782 (2006).

21. J. Li and J. B. Pendry, “Hiding under the carpet: A new strategy for cloaking,” Phys. Rev. Lett. 101, 203901 (2008).

22. B. Kanté, J. M. Lourtioz, and A. de Lustrac, “Experimental demonstration of a nonmagnetic metamaterial cloak at microwave frequencies,” Phys. Rev. B 80(20), 205120 (2009).

23. L. Y. Hsu, T. Lepetit, and B. Kanté, “Extremely thin dielectric metasurface for carpet cloaking,” Prog. Electromagnetics Res. 152, 33–40 (2015).

24. X. Ni, Z.-J. Wong, M. Mrejen, Y. Wang, and X. Zhang, “An ultrathin invisibility skin cloak for visible light,” Sciences 349, 6254 (2015).

25. Y. Yang, H. Wang, F. Yu, Z. Xu H. Chen, “A metasurface carpet cloak for electromagnetic, acoustic and water waves,” Sci. Rep. 6, 20219 (2016).

26. Y. Yang, L. Jing, B. Zheng, R. Hao, W. Yin, E. Li, C. M. Soukoulis, and H. Chen, “Full-Polarization 3D Metasurface Cloak with Preserved Amplitude and Phase,” Adv. Mater. 28, 6866 (2016).

27. M. Wei, Q. Yang, X. Zhang, Y. Li, J. Gu, J. Han, and W. Zhang, “Ultrathin metasurface-based carpet cloak for terahertz wave,” Opt. Express 25, 15635-15642 (2017)

28. B. Orazbayev, N. Mohammadi Estakhri, M. Beruete, and A. Alù, “Terahertz carpet cloak based on a ring resonator metasurface,” Phys. Rev. B 91, 195444 (2015).

29. J. Valentine, J. Li, T. Zentgraf, G. Bartal and X. Zhang, ‘’An optical cloak made of dielectrics,” Nature Materials 8 (7), 568 (2009).

30. M. Gharghi, C. Gladden, T. Zentgraf, Y. Liu, X. Yin, J. Valentine, and X. Zhang, ‘’A Carpet Cloak for Visible Light’’, Nano Letters 11, 2825–2828 (2011)

31. S. Xu, H. Xu, H. Gao, Y. Jiang, F. Yu, J. D. Joannopoulos, M. Soljačić, H. Chen, H. Sun, and B. Zhang, “Broadband surface-wave transformation cloak”, PNAS 25 7635-7638 (2015)

32. J. Yang, C. Huang, X. Wu, B. Sun, and X. Luo, “Dual-wavelength carpet cloak using ultrathin metasurface,” Adv. Opt. Mater. 6(14), 1800073 (2018).

33. C. Wang, Y. Yang, Q. Liu, D. Liang, B. Zheng, H. Chen, Z. Xu, and H. Wang, “Multi-frequency metasurface carpet cloaks,” Opt. Express 26, 14123-14131 (2018).

34. H. Tao, M. Zhao, Y. Xu, S. Wang, Z. Yang, “Broadband Metasurface Carpet Cloak in the Near Infrared Region,” IEEE Photonics Technology Letters 30 (14), 1281-1284 (2018).

35. V. R. Almeida, Q. Xu, C. A. Barios, and M. Lipson, “Guiding and confining light in void nanostructure,” Opt. Lett. 29, 1209–1211 (2004).

36. LiYi Hsu, Abdoulaye Ndao, Boubacar Kanté, “Broadband and linear polarization metasurface carpet cloak in the visible,” Optics Letters 44 (12), 2978-2981 (2019).

Chapter 4

Ultra-broadband, high efficiency, and linear polarization achromatic meta-lens from visible to telecommunication wavelength

Metasurfaces attract a continuously growing interest in the last few years because of their fascinating ability to manipulate optical phase front resulting in many different applications. However, mitigating chromatic aberration at micrometer scale for broad wavelength range using metasurfaces remains a fundamental problem for optical components and imaging applications. These fundamental limitations are in general due to the intrinsic optical properties of the employed materials, and the fundamental design principle. Here, we proposed and demonstrated a new method based on a new design principle to engineer ultra-high efficiencies achromatic metalens from visible to infrared. First, we designed a hybrid metalens which is composed of a meta-correct and a normal lens. The meta-correct corrected chromatic aberration of a normal lens. The bandwidth can be 500 nm to 1580 nm. Secondly, we proposed and experimentally demonstrated a new design that has planar structure to engineer high efficiencies and polarization-independent achromatic meta-lens from visible IR: 640 nm to 1200 nm with efficiency up to 70 % efficiencies in transmission mode. Such devices pave a new way from new functionalities that require ultra-broadband polarization-independent achromatic metalens with high efficiency.

4.1 Introduction

Since the first publication of Newton's discoveries on the decomposition of white light by prism and color theory, optical dispersion continues to fascinate the scientific world. Optical dispersion is one of the fundamental properties of optical components which can be useful for many applications such as mode locking laser, prism spectroscopy light splitting. However, optical imaging faces a major challenge: chromatic aberration resulting from optical dispersion. Chromatic aberration is generally due to the variation of the refractive index of the material of the optical components as a function of the wavelength of the light passing through them. This chromatic aberration limits the performance of broadband optical applications. To overcome these limitations, conventional optical bulky lens often uses an appropriate combination of multiple lenses. Although these methods can considerably reduce the chromatic aberration, however, these methods are bulky, expensive and wavelength limited. In addition, due to the context of stringent requirements in terms of miniaturization and further integration of heterogeneous optical and electronic functions, considerations regarding system compatibility and size without chromatic aberration become a major issue. Recent advances made in photonics, both in understanding physical phenomena and in the control of fabrication processes, have contributed to improved detection capabilities in terms of multi-functionality and miniaturization.

To face these challenges, metasurfaces have been investigated as potential alternatives for integrated optical free space components [1-4]. Metasurfaces are subwavelength nanostructured devices that enable the control of optical wave fronts, polarization, and phase. A large variety of flat optical components, including planar lenses [5-14], holograms quarter-wave plates, half wave plates, optical vortex plates, carpet cloaks, solar concentrators, polarizers, thin absorbers, biomedical imaging devices, and or sensors [16-26]. Although, metasurfaces are proposed as the most promising way to overcome these aforementioned lacks and achieve new functionalities, however, mitigating chromatic aberration at micrometer scale remains a fundamental problem for current metasurfaces. To date, multiple wavelengths, and broadband achromatic metalens have been recently reported in [5-12] to reduce monochromatic aberration. However, the currently proposed devices are so far limited discrete wavelength, continues bandwidth less than 450 nm [11], with average efficiency around 45%.

In this chapter, we proposed and experimentally demonstrated a new design principle based on Si_3N_4 (hybrid metalens) and TiO2 (planar metalens) to engineer ultra-high efficiency and achromatic meta-lens from visible (500 nm, 640 nm) to IR (1580nm, 1200 nm) with efficiencies up 90% and 70 % in transmission mode separately.

4.2 Design Principle

In order to focus light to a point for a normal incident plane wave, a flat lens needs to deflect light by a position (r) dependent angle (θ) given by the relation [5]:

$$\sin(\theta) = \frac{r}{\sqrt{r^2+F^2}} = \frac{1}{k_0}\frac{d\phi(r,\omega)}{dr}, \text{ i.e., } \phi(r,\omega) = \int dr k_0 \frac{r}{\sqrt{r^2+F^2}} = -\frac{2\pi f}{c}\left(\sqrt{r^2+F^2}-F\right) + g \quad (1)$$

Where ϕ (r, f) is the phase profile required, f is the frequency, F is the focal length, r is the radial position, c is the speed of light, and g is a reference phase function independent of r. The reference phase can be an arbitrary function of frequency because only the spatial phase difference matters for the interference of waves at the same frequency after their interaction with the lens. We thus consider the phase shift, i.e., the phase difference between the local phase and the phase at the reference position taken at r = 0 (center of the lens). Hence, the phase-shift equation for a normal incident wave $\Delta\phi(r, \mathrm{f})$ is:

$$\Delta\phi(r,\mathrm{f}) = \phi(r,\mathrm{f}) - \phi(0,\mathrm{f}) = -\frac{2\pi}{c}\left(\sqrt{r^2+F^2}-F\right)f = m(r)f, m(r) = -\frac{2\pi}{c}\left(\sqrt{r^2+F^2}-F\right) \quad (2)$$

Where m(r) is the frequency slope of the phase-shift. Equation 2 reveals the requirements of a broadband achromatic metalens. First, the phase-shift for all positions is linear with respect to frequency. This condition can be locally satisfied using waveguide modes. Second, the slope of the phase-shift (dispersion) varies with position following equation 2 and the phase-shift $\Delta\phi(r,\mathrm{f})$ is proportional to frequency, i.e., the phase-shift intercept with respect to frequency is zero. The metasurface is thus a waveguide array with, ideally, a local and simultaneous control of the slope and the intercept of the phase-shift.

4.3 First Implementation: Hybrid metalens

To satisfy the requirements of achromatic broadband metalenses, we proposed two methods to achieve the requirements. First, the hybrid metalens which composed of Si_3N_4 waveguide (meta-corrector) and a normal lens. The normal lens mainly provides different slopes of the phase-shift and the waveguide correct the intercept of the phase-shift. The slot waveguide structure is based on a low-refractive-index slot (air) formed between two high-refractive-index (Si_3N_4) waveguides. Compared to the previous work based on waveguide, the electric field is confined in the high refractive-index while the field for the slot waveguide, the mode is confined in the air which is dispersion less. This is one of the main and fundamental reasons to be able to achieve three-time broader band and higher efficiency than the previous works.

Figure 4.1(a) presents the schematic of a hybrid lens and 4.1(b) presents the considered unit cell geometry. The period of the metasurface array is 200 nm, the width of the air gap is 85nm. The substrate is SiO_2 and the slot waveguide is Si_3N_4 with air gap inside. Figure 4.1(c) shows the normalized electrical field at 375THz with L = 240 nm and p = 200 nm. One can observe that the field is well confined in the air gap even with small length (L). To demonstrate the versatility of our approach, we designed and simulated a high efficient broadband achromatic metalens. In order to control the slope of the phase-shift and the intercept of shift, we tune the thickness of the substrate (h) and the period of the slot waveguide (p). These two parameters provide enough degree of freedom to achieve a broadband metasurface lens. The thickness of the substrate mainly changes the slope (a normal lens) and the period of the slot waveguide tunes the phase shift-intercept (meta-corrector). The design flowchart is as follows. First, we linear fit each phase shifts with respect to frequency to obtain the phase slope and the phase shift-intercept. The maximum phase errors between fitting curve and simulation phase in the sweeping region are less than 20°. Figure 4.1(d) & (e) presents fits of the phase slope and phase-shift intercept plots for different values of h and p. Based on this contour plots, we optimize h and p to have the required slope and keep zero phase-shift intercept which is the main requirement of a broadband achromatic metalens. The dark circles are the designed dimensions for an aperture size of 220 µm and a focal length of 900 µm. One can observe that the intercept is zero while the slope varies from 0 to -8 °. THz^{-1}.

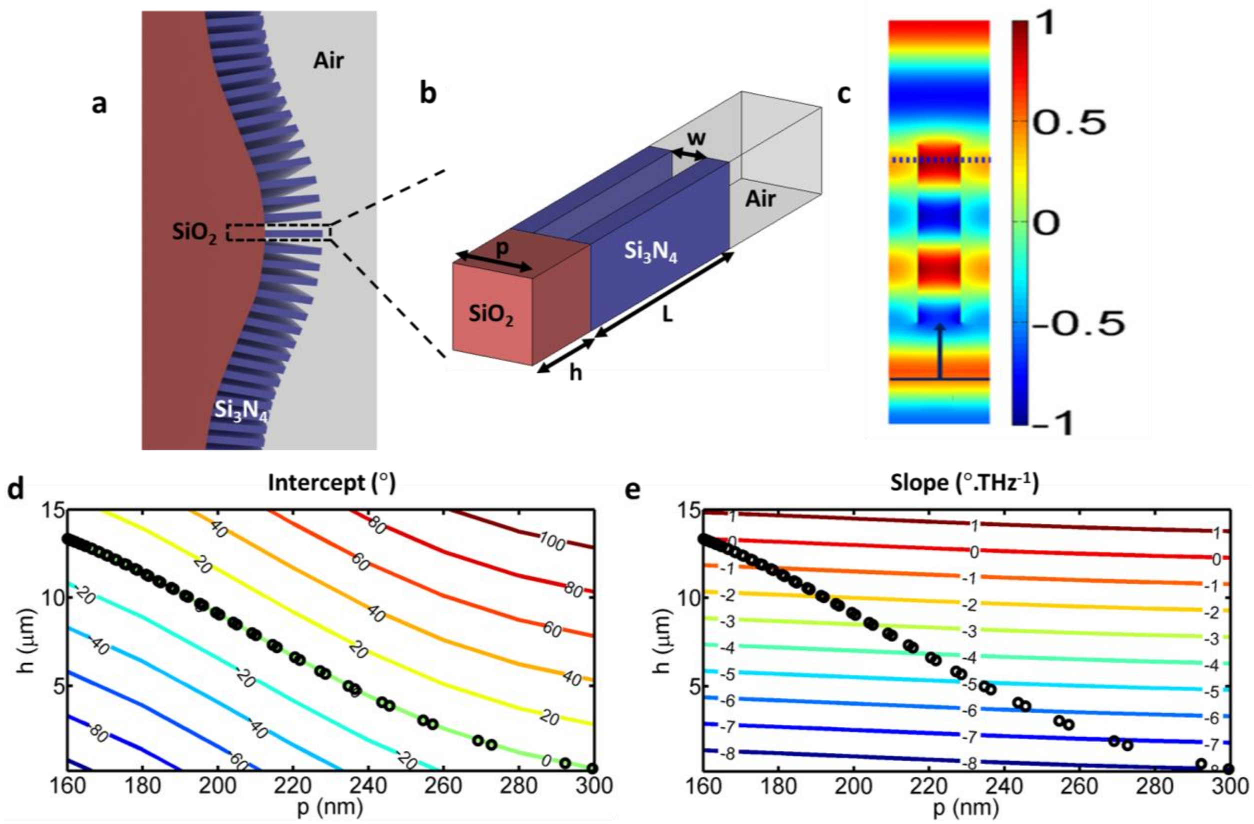

Figure 4.1 Design of metasurface (a) Schematic of a hybrid metalens. (b) Unit cell of the metalens (c) The normalized e-field of a unit cell at 375THz with L = 240 nm and p = 200 nm. (d) The intercept of the phase-shift. (e) The slope of the phase-shift.

To obtain the required 2π phase-shift, the scattering coefficients of the resonators are calculated using the commercial software CST, and, boundary conditions in x and y directions are set to periodic. When an incident plane wave with TE polarization illuminate the structure, the waves transmit through each unit cell and emit with specific phase distributions. Then, the emitted electromagnetic waves will be focused on a spot as shown in figure 4.2(a-h), which presents the normalized power intensity distributions for different frequencies. The black crosses show the focal spot of the hybrid metalens. One can observe that the focal lengths barely vary during the design frequency range. To further demonstrate the performance of the hybrid metalens. We compared the focal length respect with frequencies for the hybrid metalens (meta-corrector + normal lens) and its substrate only (normal lens only). Figure 4.3 shows the chromatic aberration of the focal lengths with frequencies range for both cases. We can observe that the chromatic aberration decreases from 40 μm to less than 10 μm.

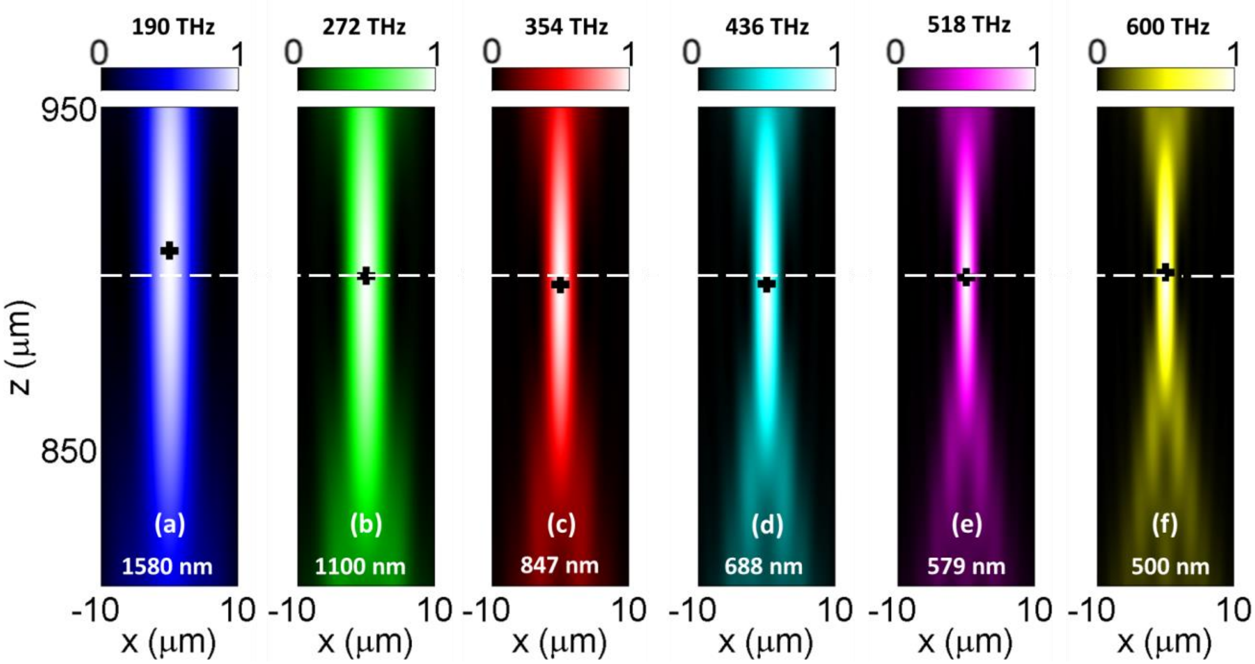

Figure 4.2 Normalized power intensity distribution for different frequencies (a) 600 THz (b) 518 THz (c) 436 THz (d) 354THz (e) 272 THz and (f) 190 THz. The black crosses present focal points and the while dish line presents the designed focal length.

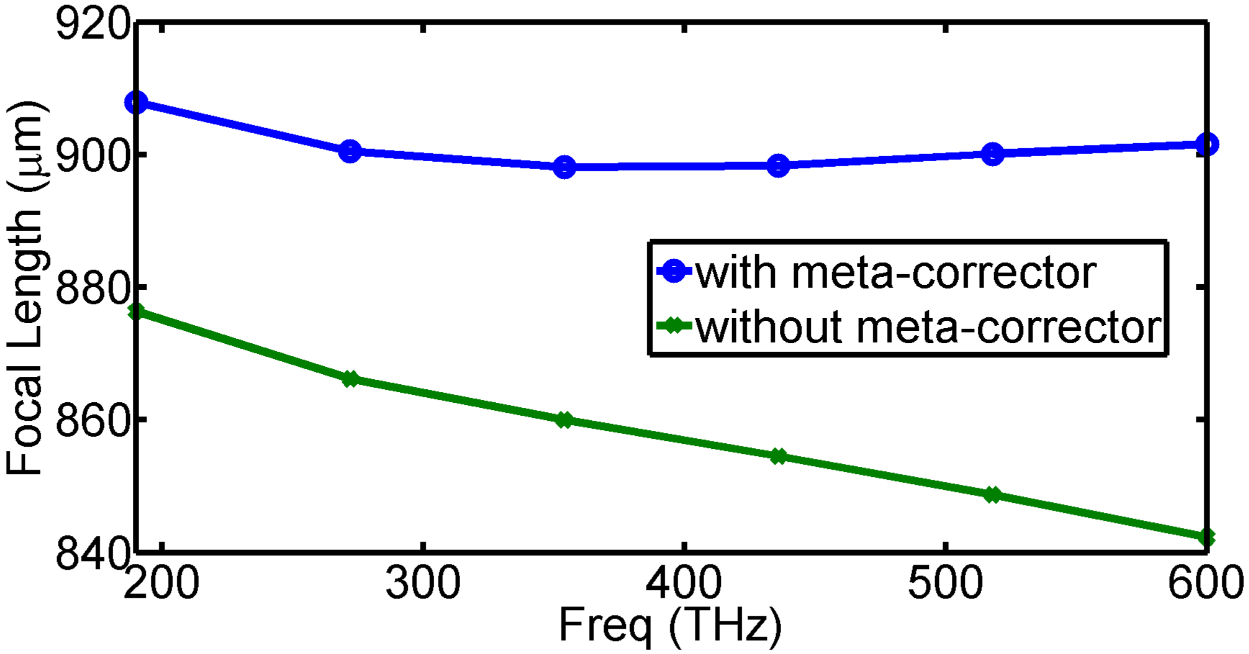

Figure 4.3 Simulation focal length in spectral range from 190 THz to 600 THz.

4.4 Second Implementation: Fishnet-Achromatic-Metalens (FAM)

In the previous section, we demonstrated the achromatic hybrid metalens. However, the meta-corrector is on a curved substrate and it is challenging to fabricate it. Hence, to make a planar achromatic metalens, we proposed to use the cross-circle (fishnet) waveguide shown in Fig. 4.4(a**)** as building block. The building block has four geometrical parameters that are the radius (R), the width (W), the length (L), and the period (P). Constraints impose for example W ≤ 2R and L ≤ P. Using geometric parameters, the slope can be controlled with a quasi-control of the phase-shift intercept consisting of minimizing it (ideally zero). Because each position has a unique (slope, phase-shift intercept) coordinate, dimensions can be chosen accordingly. It is important to note that the four geometric parameters are not independent, as a change in any of them can affect the effective index of the waveguide they form. This signifies that it is challenging to have perfect achromaticity and efficiency as phase-shift intercepts and slopes cannot be fully independently controlled in a planar design. The limitation confirms that this is intrinsically an optimization problem [29-32]. In metasurfaces, the spatial derivative of the slope controls the direction of incident rays to make them reach the focal point. It is thus important to have the correct slope to prevent chromatic effects and a decrease in efficiency. The intercept, however, controls the superposition of waves at the focal point, i.e., only affects the efficiency of the lens, not the position of the focal length. We can thus compromise on the intercept in the design of the lens.

Figure 4.4(a) presents a sketch of the titanium dioxide (TiO_2) based metasurface and the geometry of the unit-cell with multiple degrees of freedom. It is a fishnet-like structure with a period P = 370 nm and a height H = 350 nm. The structure is fabricated by top-down nanomanufacturing methods and a scanning electron micrograph of a fabricated metalens is shown in Fig. 4.4(b). To design our metasurface, geometric parameters are controlled by pair, (W, R) in Fig. 4.5(a-b) and (L, R) in Fig. 4.5(c-d). By considering fabrication limits, iso-slopes and iso-phase-shift intercept plots of realistic geometries are computed using full-wave numerical simulations (CST Microwave Studio) and the local phase method [20], followed by least-square linear fitting. The phase shift of elements is calculated using a reference at the center of the lens with geometric parameters W = 270 nm, R = 135 nm, and L = P = 370 nm. For all other geometries, the parameters in Fig. 4.5 are calculated.

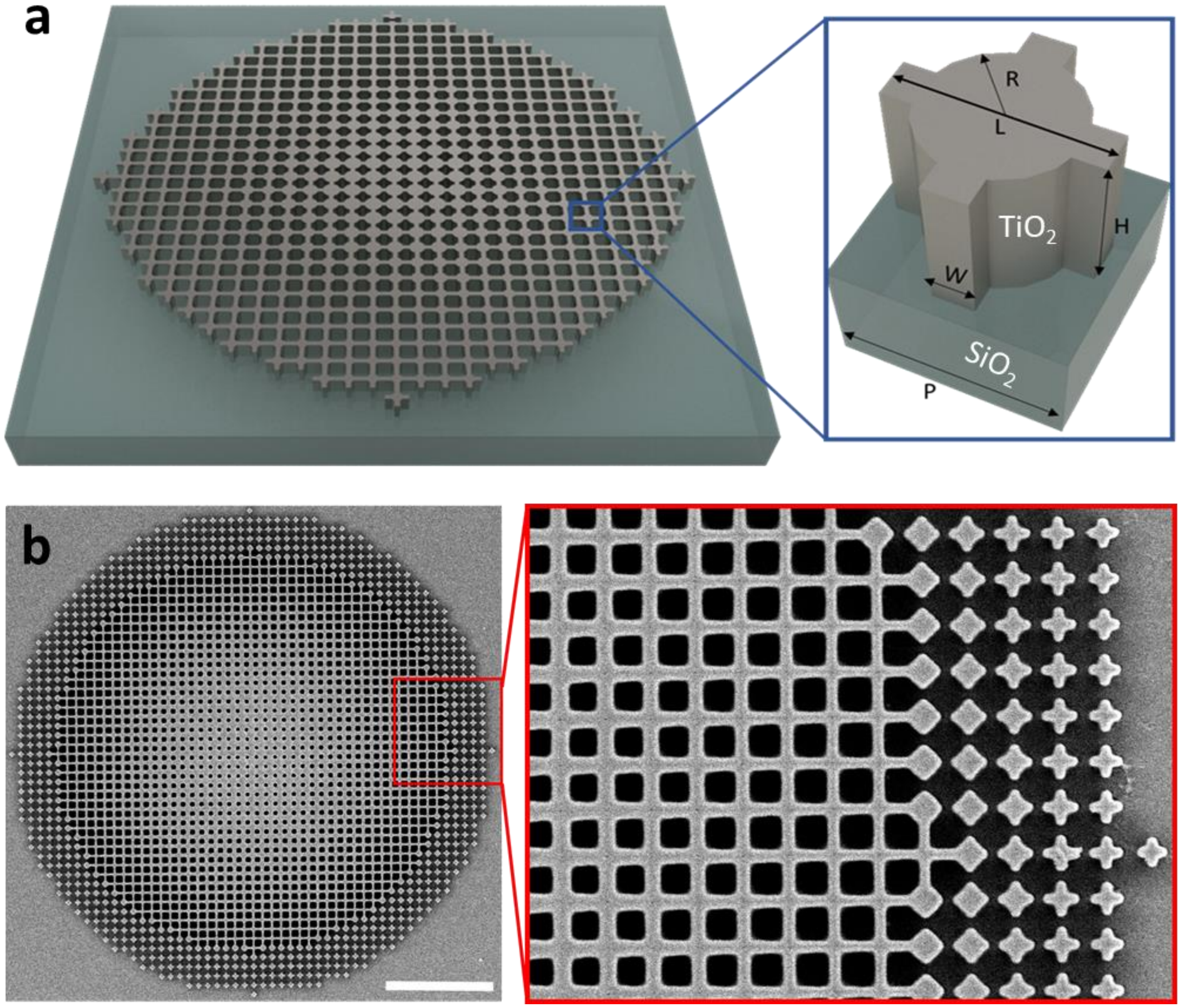

Figure 4.4 Schematic and scanning electron micrograph of a fishnet-achromatic-metalens (FAM). (a) Schematic of the proposed broadband metalens and its unit-cell with multi-degrees of freedom. The period of the unit-cell (P) is 370 nm, the height of the unit-cell (H) is 350 nm, and the metasurface is made of titanium dioxide (TiO_2). The design parameters are the width of the cross (W), the length of the cross (L), and the radius (R). (b) Top view of an optical microscope image of a fabricated FAM and zoom-in showing the quality of the fabricated device. The scale bar represents 5 µm.

Figure 4.5(a) and 4.5(c) show that changes in R, W, and L enable slopes from zero to -0.35°.THz^{-1} which in turn determines the maximum achievable size of the metalens for a given focal length. The figure also confirms that it is not possible to fully independently control the slope and the phase shift-intercept. However, accepting an error on the phase shift intercept enables designs sweeping all slope values. Fig. 4.5(a**)** enables slopes from zero to -0.2°.THz^{-1} while keeping a phase-shift intercept error below 30° (Fig. 4.5(b)). For the 20 µm x 20 µm metalens, we have chosen points indicated in blue (along the black arrow) to minimize discretization errors and points in the grey area are not physical as W≥2R. For absolute value of slopes larger than 0.2°.THz^{-1}, we used parameters in Fig. 4.5(c) and the second trajectory (blue points along the black arrow) also keeps the phase-shift intercept error below 30° (Fig. 4.5(d)).

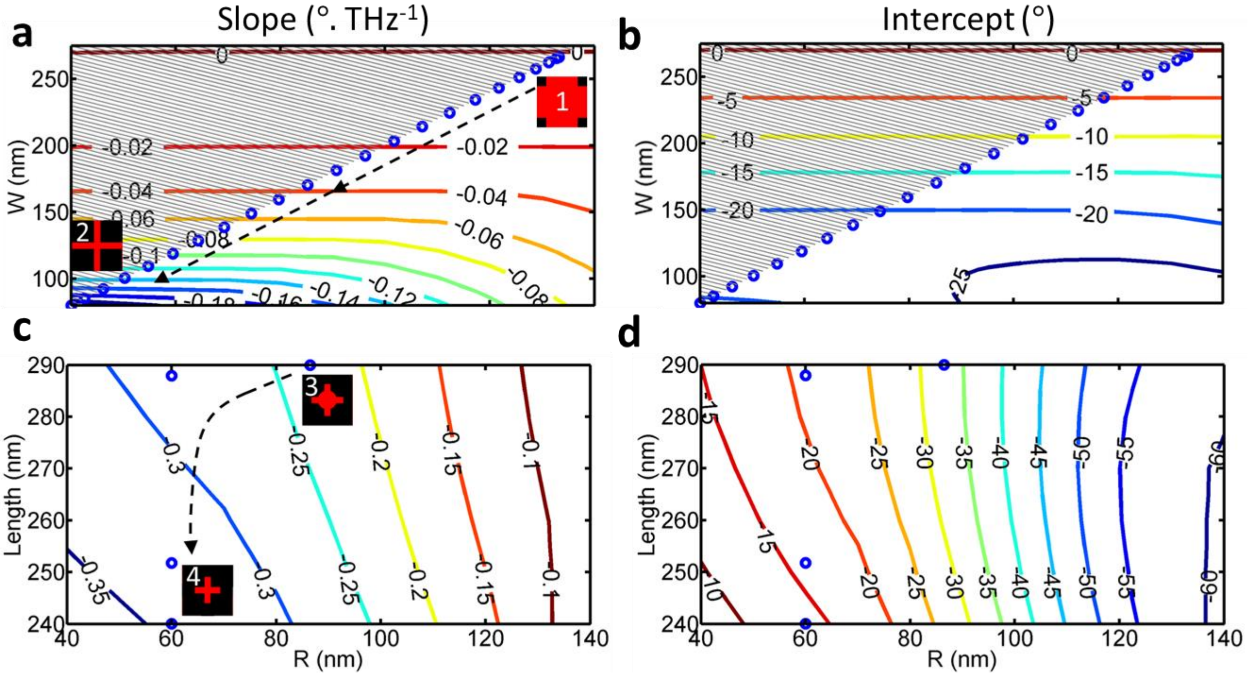

Figure 4.5 Design strategy of the FAM. To control the slope (a, c) and the phase-shift intercept (b, d), at least two parameters need to be controlled. The considered two parameters are the width and the radius (W, R) (from step 1 to step 2 in fig. 2 (a-b)) and the length and the radius (L, R) (from step 3 to step 4 in fig. 2 (c-d)). From step 1 to step 2, W varies from 80 nm to 270 nm, and, R varies from 60 nm to 135 nm while L is fixed to 370 nm. From step 3 to step 4, L varies from 240 nm to 290 nm while W is fixed to 80 nm to account for limitations in fabrication. Insets in Fig. 2(a) illustrate the evolution of the structure (top view) as one moves from the center (step 1) to the edge of the FAM (step 4), and, red/ back colors represent TiO$_2$/ SiO$_2$.

4.5 Efficiency ratio change with non-zero phase-shift intercepts in the metalens

To quantify the impact of a non-zero phase-shift intercept on the efficiency of our metalens, Monte Carlo simulations are performed with hundred simulations for each element using a homemade finite difference time domain code. Each simulation was given a certain magnitude of the phase-shift intercept (error or deviation from the ideally zero phase-shift intercept) that was randomly distributed between unit-cells. The focus efficiency was then compared to the ideal metalens implementing not only the correct slope but also the correct phase-shift intercept. Results, presented in Fig 4.6, indicate that an error on the phase-shift intercept smaller than 30° decreases the efficiency of the metalens by less than 10% and does not affect the position of the focal point. Monte Carlo simulations are performed with hundred simulations for each element in the metalens by using a homemade finite difference time domain code. Each simulation was given a certain magnitude of the phase-shift intercept (error or deviation from the ideally zero phase-shift intercept) that was randomly distributed between unit-cells. The focus efficiency ($\eta(\Delta)$) is then compared to the ideal metalens ($\eta(0)$) implementing not only the correct slope but also the correct phase-shift intercept.

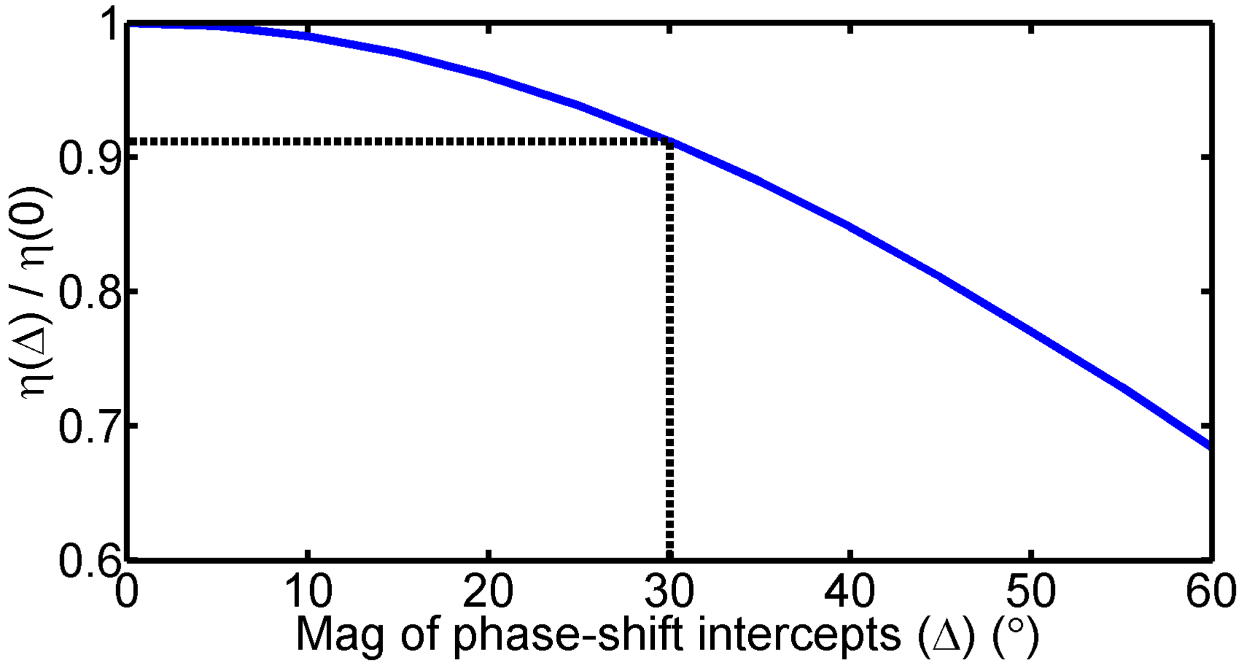

Figure 4.6 Efficiency ratio between the metasurface with randomly distributed non-zero phase-shift intercept (η (Δ)) and the one with zero phase-shift intercept (η (0)).

4.6 Fabrication method

The designed structure is fabricated by top-down methods and the scanning electron micrograph (SEM) of a metalens, presented in Fig. 4.4(b). Fig. 4.7 illustrates the flow chart of a metasurface fabrication using the top-down etching and lift-off process. First, it is crucial to thoroughly clean the BK7 glass substrate in order to acquire a surface as clean as possible for the subsequent deposition steps. The glass substrate is immersed in an acetone bath to remove any organic traces and then transferred to an isopropyl alcohol-containing beaker to remove the remaining dirt of any origin. In addition, O_2 plasma treatment performed to the glass substrate for adhesion between glass and other materials including resist and TiO_2. An electron beam resist (370nm PMMA A4) is coated on the sample (1500 rpm) followed by 1min bake at 180 °C (hot plate). The metasurface pattern is written in the resist using electron beam lithography (EBL) (step c in Fig. 4.7)). We patterned the resist using electron beam lithography then development process performed to remove the exposed EBR. This resist pattern is the inverse of our final metasurface. We transferred the patterned sample to an ALD chamber set to 100 °C. The low temperature deposition is important to obtain the desired amorphous material and also to avoid the contamination of the ALD chamber by the EBR. Using planarization method, we removed the residual TiO_2 film on top of the surface of the resist by reactive-ion-etching using applying mixture of BCl_3 and Cl_2 gases (20:8 sccm), 200W, 40 mtorr. The etch depth was equal to tfilm so that the etching process exposes the underlying resist and the top of the nanostructures. We finally removed the remaining EBR (step g in Fig. 4.7) and left only the TiO_2 metasurfaces.

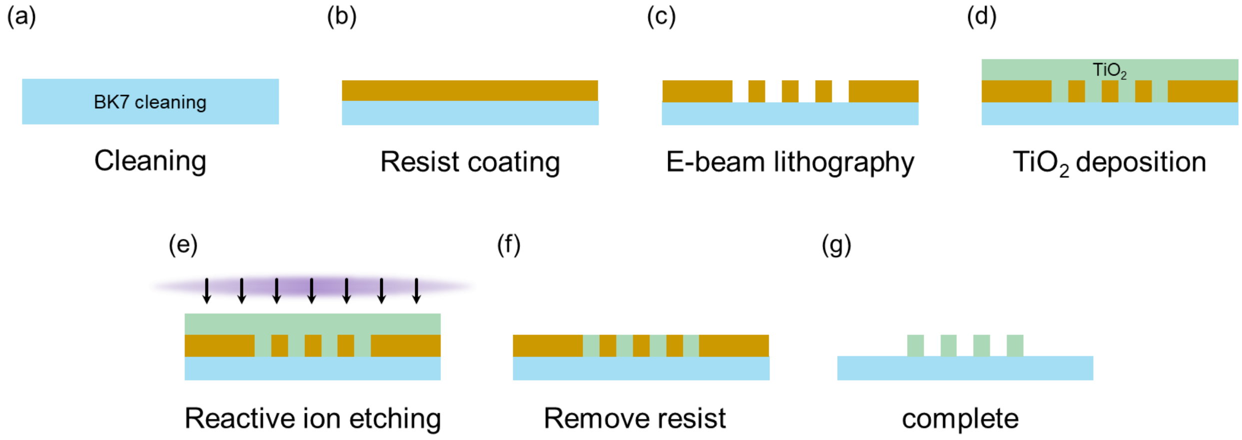

Figure 4.7 Fabrication flow chart of metalenses.

4.7 Experimental measurements

To optically characterize the fabricated lenses, a custom setup was used (Fig. 4.8). The experimental setup is composed of two main systems dedicated to illumination and imaging. The illumination system comprises a supercontinuum laser (NKT photonics) and an acousto-optic tunable filter (Super K) to select the operating wavelength from 640 nm to 1200 nm with bandwidth around 10 nm. For the image system, a 50X extra-long working distance microscope objective lens with a NA =0.65 and a tube lens with a focal distance of 20 cm were used to image intensity at planes of interest to a camera. To image different plane of the sample, we moved the sample using translation stage around the focal point.

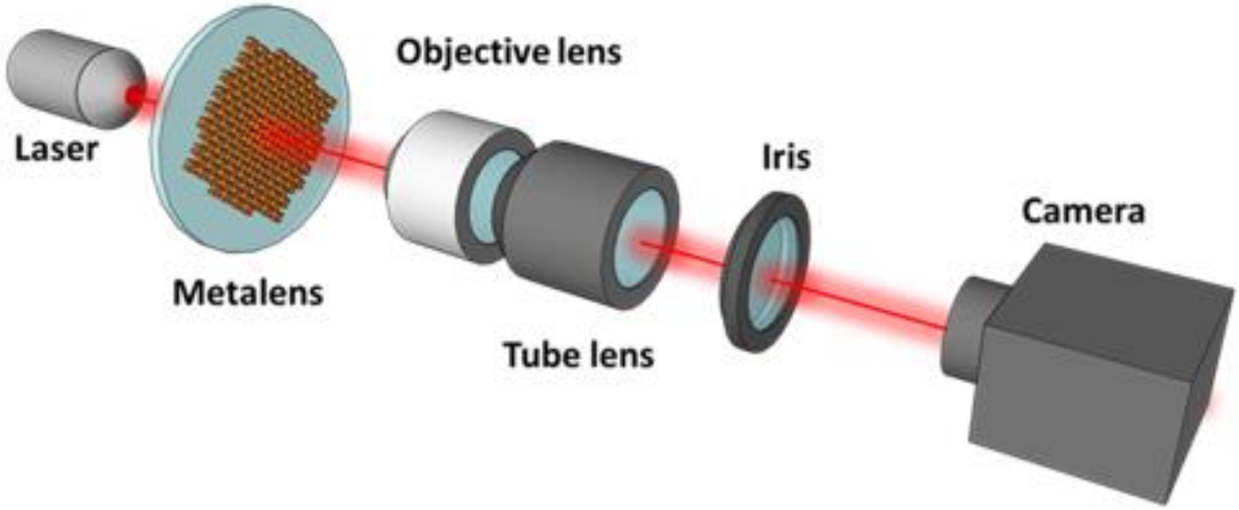

Figure 4.8 Experimental setup.

Figure 4.9 a presents the measured intensity profiles in the focal plane z = F (transverse x-y plane) of the metalenses at different wavelengths (10μmx10μm). The dots in Fig. 4.9(b) represent a normalized cross-section of the experimental measurements in Fig. 4.9(b) and the lines correspond to the theoretical Airy disk. Figure 4.9(c) shows the normalized intensity profiles in the plane x = 0 (axial x-z plane) around the focal point of the metalens at different wavelengths. Black crosses represent the focal spots for different wavelengths. These results show nearly diffraction-limited focal spots with no obvious distortion.

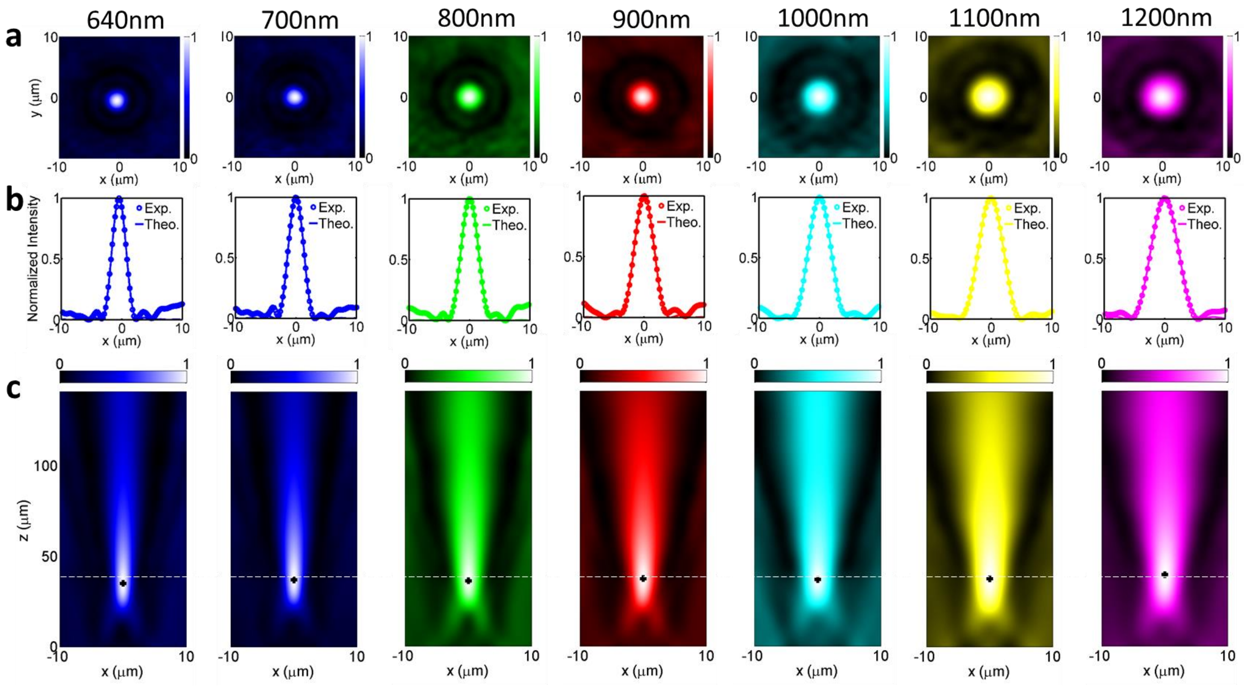

Figure 4.9 Experimental demonstration of achromatic and broadband focusing by a FAM. (a) Measured intensity profiles in the focal plane z = F (transverse x-y plane) of the FAM at different wavelengths from 640 nm to 1200 nm. (b) Normalized cross-section of the experimental measurements in Fig. 4.9 (a) and the lines correspond to the theoretical Airy disk. (c) Normalized intensity profiles in the plane x = 0 (axial x-z plane) around the focal point of the FAM at different wavelengths. Black crosses represent the focal spots for different wavelengths from 640 nm to 1200 nm.

Similarly, figure 4.10 represents the top view (x-z plane) of the experimental intensity profiles of the achromatic metalens along axial planes at different wavelength from 640 nm to 1200nm (15μmx15μm). The black crosses represent the center of focal spots for different wavelength from 640 nm to 1200 nm. Figure 4.11 presents the normalized intensity profiles along the black cross achromatic metalens. Measured intensity profiles (1D and 2D) of the achromatic metalens at different wavelength from 640 nm to 1200 nm (15μmx15μm). The circles are the measurement and the lines are from an ideal Airy spot. Moreover, figure 4.12 and 4.13 show the same plots for the size of 20μmx20μm.

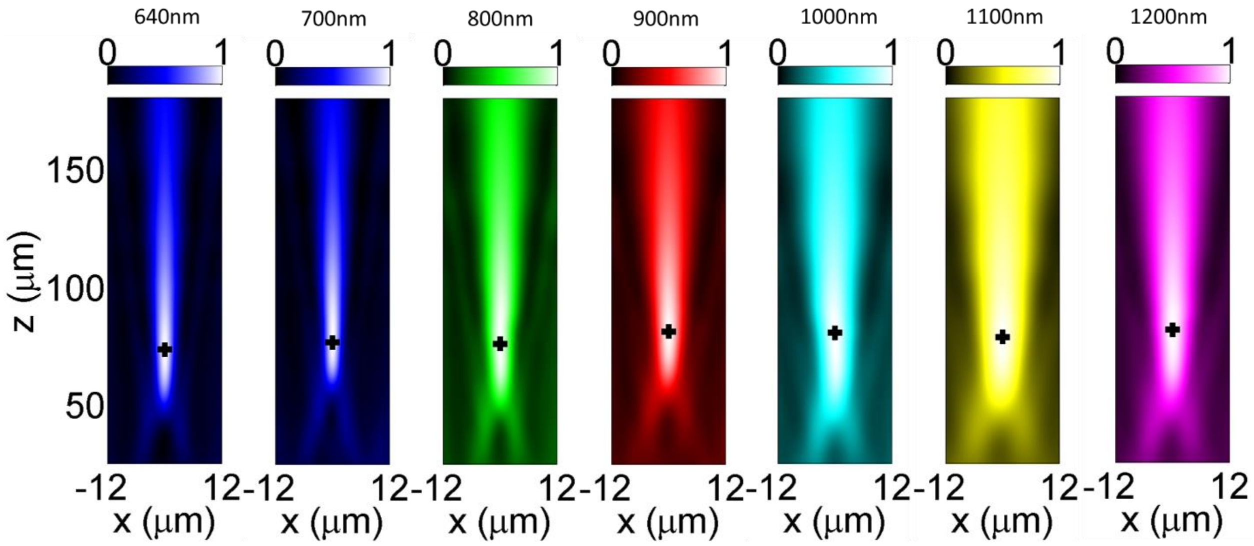

Figure 4.10 Top view (x-z plane) of the experimental intensity profiles of the achromatic metalens along axial planes at different wavelength from 640 nm to 1200nm (15μmx15μm). The black crosses represent the center of focal spots for different wavelength from 640 nm to 1200 nm.

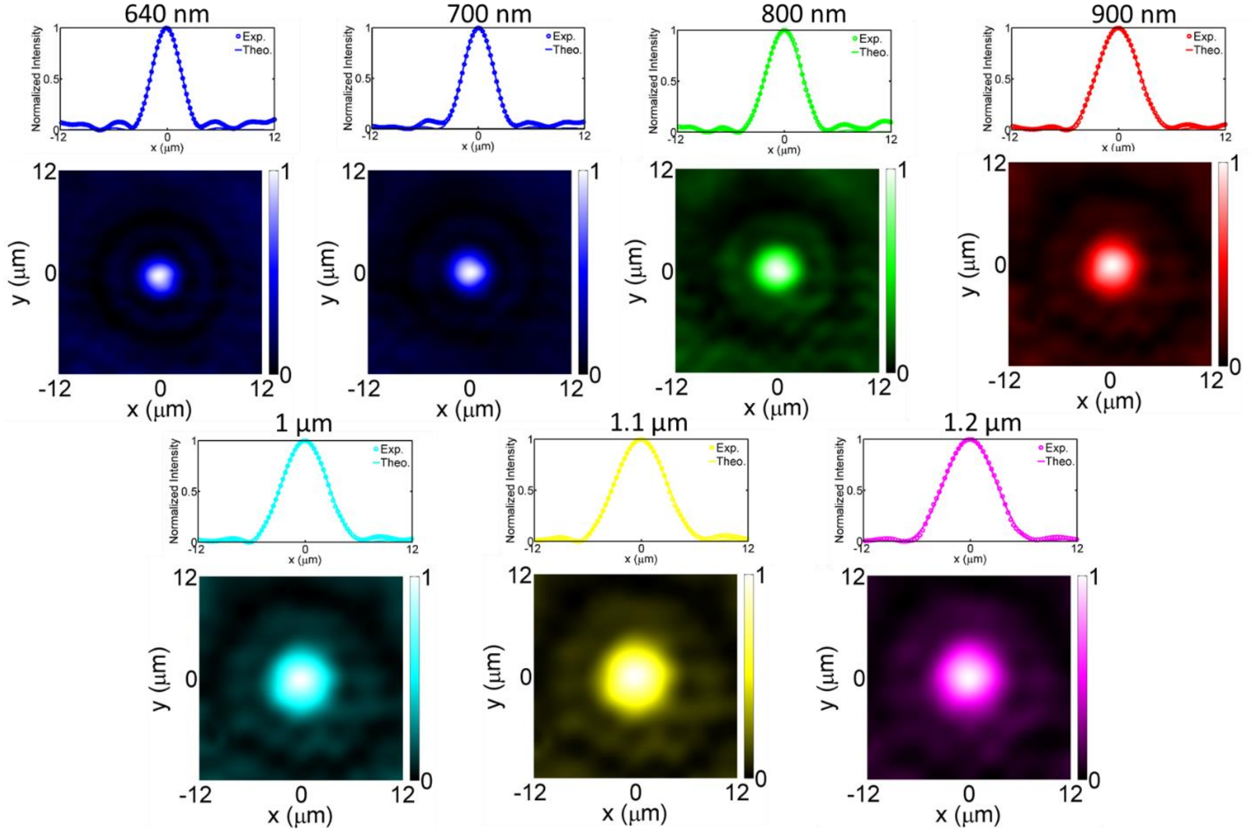

Figure 4.11 presents the normalized intensity profiles along the black cross achromatic metalens in Fig. 4.10. Measured intensity profiles (1D and 2D) of the achromatic metalens at different wavelength from 640 nm to 1200 nm (15μmx15μm). The circles are the measurement and the lines are from an ideal Airy spot.

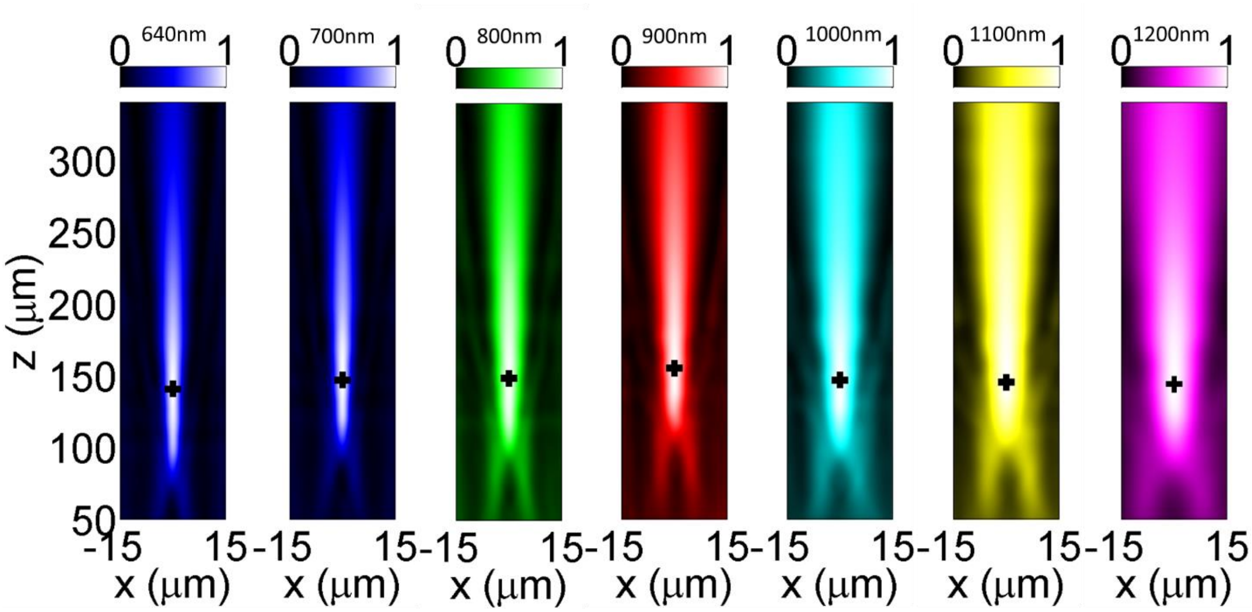

Figure 4.12 Top view (x-z plane) of the experimental intensity profiles of the achromatic metalens along axial planes at different wavelength from 640 nm to 1200nm (20μmx20μm). The black crosses represent the center of focal spots for different wavelength from 640 nm to 1200 nm.

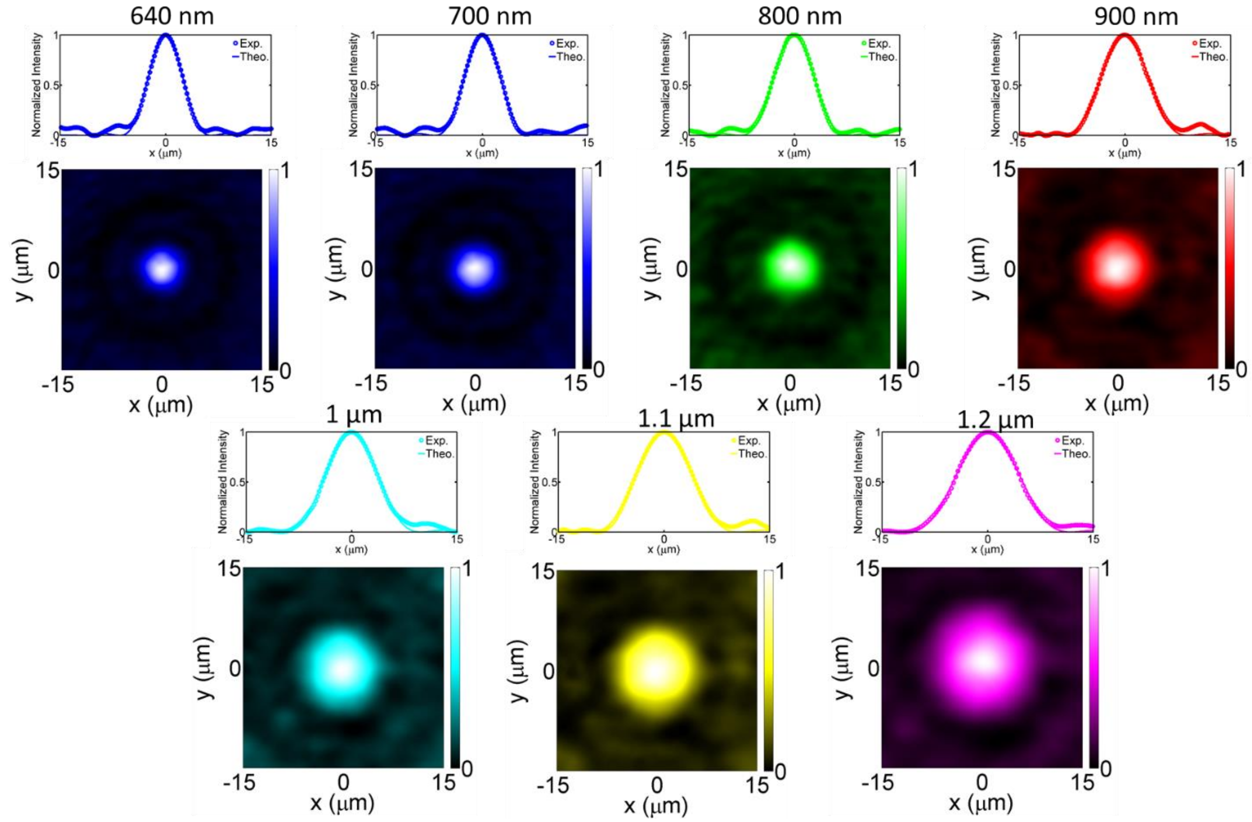

Figure 4.13 Normalized intensity profiles along the black cross achromatic metalens in Fig. 4.12. Measured intensity profiles (1D and 2D) of the achromatic metalens at different wavelength from 640 nm to 1200 nm (20µmx20µm). The circles are the measurement and the lines are from an ideal Airy spot.

4.8 Performance Measurement

To further examine the performance of designed metalenses, we measured focal lengths, focusing efficiencies, and full-widths at half-maximum (FWHM) for different lens diameters as shown in Fig. 4.14 Figure 4.14(a–c) presents SEM images of lenses of diameters 10 µm, 15 µm, and 20 µm. Figure 4.14(d) presents the focal length of the metalenses and shows that they are mostly unchanged when the wavelength varies from 640 nm to 1200 nm, demonstrating the successful realization of the broadband achromatic property. Figure 4.14(e) presents the focusing efficiency for metasurfaces of different diameters and focal lengths. The measured efficiency of a metalens is defined as the focal spot power divided by the transmitted power through an aperture of the same diameter as the metalens. Efficiencies from 65% to 75% for the entire band are measured. In Fig. 4.14(f), the experimental FWHM plots of the focal spots show that they nicely follow a diffracted limited focus (black dashed lines). We have thus successfully implemented planar achromatic metalenses spanning the continuous wavelength range from 640 nm in the visible to 1200 nm in the infrared.

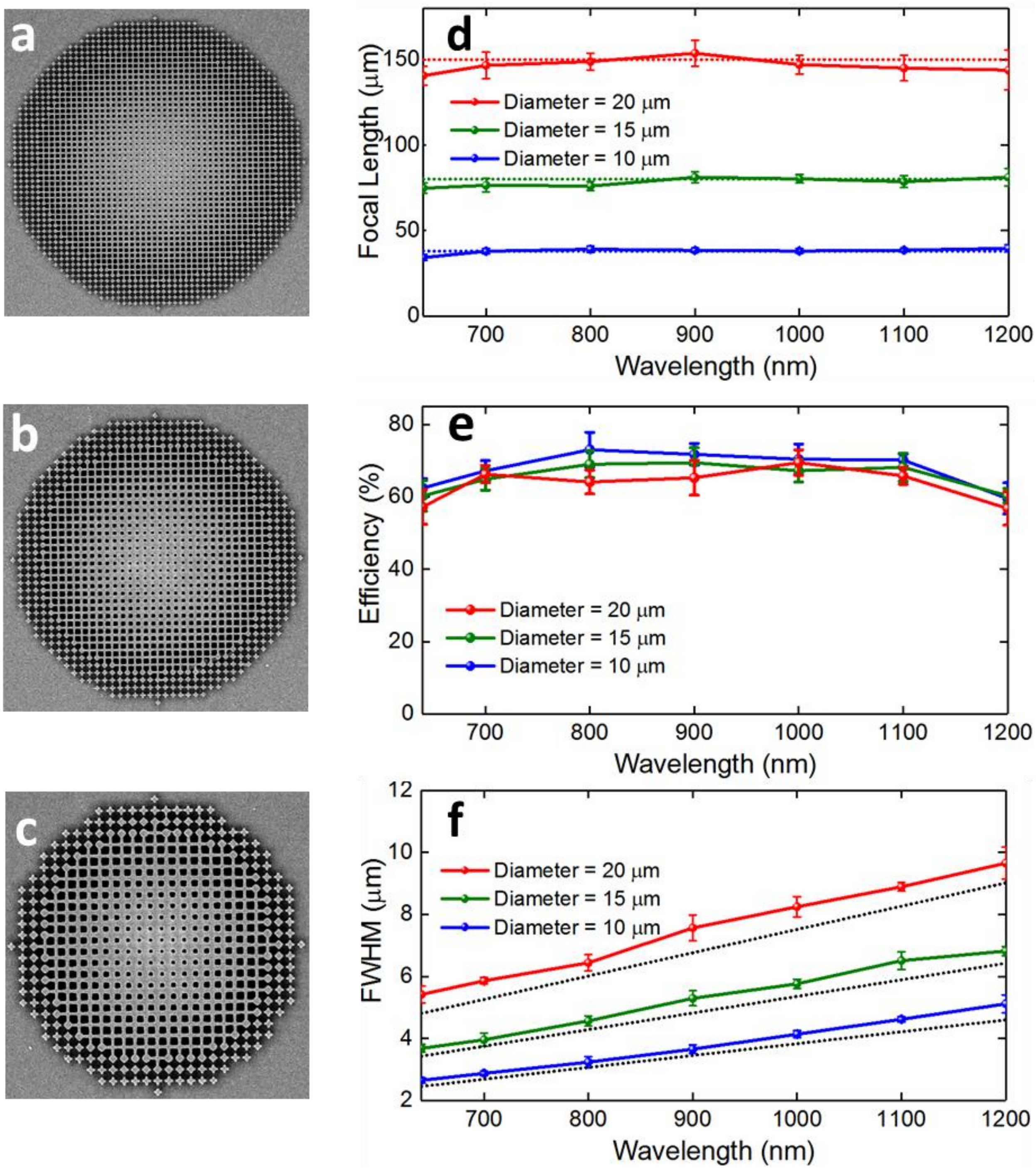

Figure 4.14 Measured performance of various FAMs. SEM of metalenses of diameter 20 µm (a), 15 µm (b), and 10 µm (c). (d) Comparison of the measured and designed focal lengths for metalenses of various sizes. € Focus efficiency and (f), FWHM at corresponding focal planes as a function of the wavelength. The measured average efficiency is about 70% in the band from 640 nm to 1200 nm. The measured efficiency of a FAM is defined as the power at the focal spot divided by the power transmitted through an aperture of the same diameter as the FAM. Error bars are the standard deviation of measurements on different samples.

4.9 Conclusion

We proposed and experimentally demonstrated metalenses combining high efficiency, polarization independence, and achromaticity in the continuous wavelength range ranging from 640 nm in the visible to 1200 nm in the infrared. The broadband operation is achieved by enforcing the slopes of the phase-shift that vary continuously from the center of the lens to its edge, and, by minimizing the phase-shift intercepts that are ideally zero for achromatic operation. To the best of our knowledge, this is the broadest band achromatic metalens reported to date. The proposed approach significantly extends the current state of the art of metalenses both in terms of bandwidth and efficiency and opens the door to many applications.

Chapter 4, in part, has been submitted for publication of the material as it may appear in Nature Communications, 2020, A. Ndao, J. Ha, J. Park, and B. Kanté. The dissertation author was the primary researcher and author of this paper.

Chapter 4, in part, is currently being prepared for submission for publication of the material. A. Ndao and B. Kanté. The dissertation/thesis author was the primary investigator and author of this material.

4.10 Reference

1. Lalanne, P., Astilean, S., Chavel, P., Cambril, E. & Launois, H. Blazed binary subwavelength gratings with efficiencies larger than those of conventional échelette gratings. Opt. Lett. **23**, 1081-1083 (1998).

2. Bomzon, Z., Kleiner, V. & Hasman, E. Pancharatnam-Berry phase in space variant polarization-state manipulations with subwavelength gratings. Opt. Lett. **26**, 1424-1426 (2001).

3. Lu, F., Sedgwick, F. G., Karagodsky, V., Chase,C., & Chang-Hasnain, C. J. Planar high-numerical-aperture low-loss focusing reflectors and lenses using subwavelength high contrast gratings, Opt. Exp. **18**, 12606-12614 (2010).

4. Fong, B. H., Colburn, J. S., Ottusch, J. J., Visher, J. L. & Sievenpiper, D. F. Scalar and tensor holographic artificial impedance surfaces. IEEE Trans. Antennas Propag. **58**, 3212-3221 (2010).

5. Yu, N. F., Genevet, P., Kats, M. A., Aieta, F., Tetienne, J.-P., Capasso, F., Gaburro, Z., Light propagation with phase discontinuities: generalized laws of reflection and refraction. Science **334**, 6054 (2011).

6. Arbabi, A., Horie, Y., Ball, A. J., Bagheri, M. & Faraon, A. Subwavelength-thick lenses with high numerical apertures and large efficiency based on high contrast transmit arrays. Nat. Commun. **6**, 7069 (2015).

7. Khorasaninejad, M, Chen, W.-T., Devlin, R. C., Oh, J., Zhu, A.Y., Capasso, F., Metalenses at visible wavelengths: diffraction-limited focusing and subwavelength resolution imaging. Science **352**, 6290 (2016).

8. Pors, A., Nielsen, M. G., Eriksen, R. L. & Bozhevolnyi S. I., Broadband Focusing Flat Mirrors Based on Plasmonic Gradient Metasurfaces. Nano Lett. **13**, 829-834 (2013).

9. Khorasaninejad, M., Shi, Z., Zhu, A. Y., Chen, W.T., Sanjeev, V., Zaidi, A., Capasso, F., Achromatic metalens over 60 nm bandwidth in the visible and metalens with reverse chromatic dispersion. Nano Lett. **17**, 1819-1824 (2017).

10. Wang, S. M., Wu, P. C., Su., V.-C., Lai, Y.-C., Chu, C. H., Chen, J.-W., Lu, S.-H., Chen, J., Xu, B., Kuan, C.-H., Li, T., Zhu, S., Tsai, D. P., Broadband achromatic optical metasurface devices. Nat. Commun. **8**, 187 (2017).

11. Chen, W. T., Zhu, A. Y., Sanjeev, V., Khorasaninejad, M., Shi, Z., Lee, E., Capasso, F., A broadband achromatic metalens for focusing and imaging in the visible. Nat. Nanotechnol. **13**, 220-226 (2018).

12. Wang, S. M, Wu, P. C., Su, V.-C., Lai, Y.-C., Chen, M.-K., Kuo, H. Y., Chen, B. H., Chen, Y. H., Huang, T.-T., Wang, J.-H., Lin, R.-M., Kuan, C.-H., Li, T., Wang, Z., Zhu, S., Tsai, D. P., A broadband achromatic metalens in the visible. Nat. Nanotechnol. **13**, 227-232 (2018).

13. Shrestha, S., Overvig, A. C., Lu, M., Stein, A. & Yu, N. Broadband achromatic dielectric metalenses. Light: Science & Applications **7**, 85 (2018).

14. Chen, W. T., Zhu, A. Y., Sisler, J., Bharwani, Z. & Capasso, F. A broadband achromatic polarization-insensitive metalens consisting of anisotropic nanostructures. Nat. Commun. **10**, 355 (2019).

15. Zheng, G. X., Muhlenbernd, H., Kenney, M., Li, G., Zentgraf, T., Zhang, S., Metasurface holograms reaching 80% efficiency. Nat. Nanotechnol. **10**, 308-312 (2015).

16. Yu, N. F., Aieta, F., Genevet, P., Kats, M. A., Gaburro, Z., Capasso, F., A broadband, background-free quarter-wave plate based on plasmonic metasurfaces. Nano Lett. **12**, 6328-6333 (2012).

17. Kats, M. A., Blanchard, R., Genevet, P., Capasso, F. Nanometre optical coatings based on strong interference effects in highly absorbing media. Nat. Materials **12**, 1, 20 (2013).

18. Hsu, L. Y., Lepetit, T. & Kanté, B., Extremely thin dielectric metasurface for carpet cloaking. Prog. Electromagnetics Res. **152**, 33-40 (2015).

19. Ni, X., Wong, Z. J., Mrejen, M., Wang, Y. & Zhang, X. An ultrathin invisibility skin cloak for visible light. Science **349**, 6254 (2015).

20. Hsu, L., Dupré, M., Ndao, A., Yellowhair J. & Kanté, B. Local phase method for designing and optimizing metasurface devices. Opt. Express **25**(21), 24974-24982 (2017).

21. Devlin, R. C., Ambrosio, A., Rubin, N. A. , Mueller, J. P. B. & Capasso, F. Arbitrary spin-to-orbital angular momentum conversion of light. Science **358**, 6365 (2017).

22. Ding Q., Barna, S. F., Jacobs, K., Choubal, A., Mensing, G., Zhang, Z., Yamada, K., Kincaid, N., Zhu, G., Tirawat, R., Wendelin, T., Guo, J., Ferreira, P., Jr, K. C. T., Feasibility Analysis of Nanostructured Planar Focusing Collectors for Concentrating Solar Power Applications. ACS Applied Energy Materials, **12**, 6927-6935 (2018).

23. Shaltout, A. M., Shalaev, V. M., Brongersma, M. L. Spatiotemporal light control with active metasurfaces. Science **364**, 6441 (2019).

24. Divitt S., W Zhu, Zhang, C., Lezec, H.J., Agrawal A. Ultrafast optical pulse shaping using dielectric metasurfaces. Science **364**, 6443 (2019).

25. Ren, H., Briere, G., Fang, X., Ni, P., Sawant, R., Héron, S., Chenot, S., Vézian, S., Damilano B., Brändli V., Maier, S. A. & Genevet P. Metasurface orbital angular momentum holography. Nat. Commun. **10**, 1, 2986, (2019).

26. Shaltout, A. M., Lagoudakis, K. G., Groep, J. V. D., Kim, S. J., Vučković, J., Shalaev, V. M., Brongersma & M. L. Spatiotemporal light control with frequency-gradient metasurfaces. Science **365**, 6451 (2019).

27. Ding Q., Barna, S. F., Jacobs, K., Choubal, A., Mensing, G., Zhang, Z., Yamada, K., Kincaid, N., Zhu, G., Tirawat, R., Wendelin, T., Guo, J., Ferreira, P., Jr, K. C. T., Feasibility Analysis of Nanostructured Planar Focusing Collectors for Concentrating Solar Power Applications. ACS Appl. Energy Mater. **1**, 6927-6935 (2018).

28. Zhou, Y., Kravchenko, I. I., Wang, H., Zheng H., Gu, G. & Valentine J. Multifunctional metaoptics based on bilayer metasurfaces. Light: Science & Applications **8**, 80 (2019).

29. Phan, T., Sell, D., Wang, E. W., Doshay, S., Edee, K., Yang, J. & Fan, J. A. High-efficiency, large-area, topology optimized metasurfaces. Light: Science & Applications **8**, 48 (2019).

30. Karagodsky, V., Sedgwick, F. G. & Chang-Hasnain, C. J. Theoretical analysis of subwavelength high contrast grating reflectors. Opt. Express **18**, 16973-16988 (2010).

31. Xiao, T. P., Cifci, O. S., Bhargava, S., Chen, H., Gissibl, T., Zhou, W., Giessen, H., Toussaint, K. C., Jr, Yablonovitch, E., Braun, P. V. Diffractive Spectral-Splitting Optical Element Designed by Adjoint-Based Electromagnetic Optimization and Fabricated by Femtosecond 3D Direct Laser Writing. ACS Photonics **3**, 886-894 (2016).

32. Zhang, H., Hsu, C. W. & Miller, O. D. Scattering concentration bounds: brightness theorems for waves. Optica **10**, 1321-1327 (2019).

Chapter 5

Local phase method for designing and optimizing metasurface devices

Metasurfaces have attracted significant attention due to their novel designs for flat optics. However, the approach usually used to engineer metasurface devices assumes that neighboring elements are identical, by extracting the phase information from simulations with periodic boundaries, or that near-field coupling between particles is negligible, by extracting the phase from single particle simulations. This is not the case most of the time and the approach thus prevents the optimization of devices that operate away from their optimum. Here, we propose a versatile numerical method to obtain the phase of each element within the metasurface (meta-atoms) while accounting for near-field coupling. Quantifying the phase error of each element of the metasurfaces with the proposed local phase method paves the way to the design of highly efficient metasurface devices including, but not limited to, deflectors, high numerical aperture metasurface concentrators, lenses, cloaks, and modulators.

5.1 Introduction

Optical metasurfaces are artificial planar structures, composed of dielectric or plasmonic nano-resonators [1-3]. Metasurfaces offer a wide control over the reflection and refraction by tuning the amplitude, the phase, and the polarization states of light incident on a surface [4]. In addition to having strong potentials in applied research such as optical components (lenses, optical wave-plates, modulators, etc.) [5-9] cloaking devices [10-11], solar applications [12-13], biomedical imaging [14], sensing [15-16], hologram [17], metasurfaces are of great scientific interest to explore fundamental questions in optics and wave physics in complex environments. In general, there are two primary methods to design efficient metasurfaces. Both methods involve the engineering of the phase and amplitude information. The first approach is the single meta-atom method [18] and it consists in calculating the reflection or transmission phase of a single particle by assuming that near-field coupling between particles is negligible. The second method is a widely used approach that we term the unit cell method (UCM). In this approach, unit cell boundary conditions are used, and the phase is thus obtained with identical neighbors. This method is only accurate if coupling differences between identical and different neighbors are negligible, which we called near-field coupling difference throughout the paper. However, in physical metasurface devices, the elements are not single particles or identical particles and devices constructed using these methods are thus not optimized. To the best of our knowledge, no numerical approach has been reported in the literature to address this problem. Here, we propose a method, that we term the local phase method (LPM). The LPM accounts for near-field coupling between adjacent neighbors. It is a powerful and versatile tool to quantify the phase error and amplitude of each element of the metasurface. These quantifications can be used to design high efficiency metasurface devices for various applications. The paper briefly presents the LPM and illustrates its capabilities and advantages for various applications such as deflectors (for different designs) and high numerical aperture concentrators. Furthermore, we compare the LPM to the UCM with the same examples.

5.2 Local phase method

For applications based on metasurfaces without strong near-field coupling, the unit cell method is sufficient. However, when strong near-field coupling is present, the unit cell method limits the performance of devices. To address these limitations, we propose the LPM that takes into account near-field coupling differences and quantifies the phase of meta-atoms in presence of non-identical neighbors. This quantification based on the LPM allows an efficient optimization of metasurfaces for a given application.

We first consider the standard UCM for a metasurface deflector that relies on the simulation and analysis of individual elements in a periodic array. The metasurface elements provide a linear phase shift as a function of their position with a constant phase difference of 40° between adjacent elements, which correspond to 9 (360° / 40°) elements. Figure 5.1(a) depicts the super-cell illuminated by a plane wave incident at an angle (10°) on the metasurface and polarized along the Y direction. The incident field interacts with the TiO_2 dielectric resonator (in brown), and is reflected by a metallic ground plane modelled as a perfect electric conductor (PEC) in grey. The light blue color represents the SiO_2 spacer. The boundary conditions in other directions (x and y) are set to periodic boundary conditions.

To obtain the phase of each element, we start by computing the field of the whole structure using the commercial software CST. From this total field ($\mathbf{E}$, $\mathbf{H}$), we obtain the equivalent sources ($\mathbf{J}_s$, $\mathbf{M}_s$) of each element (blue boxes in Fig. 5.1(a)) using the equivalence principle [19]. According to the equivalence principle, the field outside a virtual closed surface can be obtained by suitable electric- and magnetic-current densities over the closed surface. The equivalent current densities are given by the following equations:

$$\boldsymbol{J}_s = \boldsymbol{n} \times \boldsymbol{H} \tag{1}$$

$$\boldsymbol{M}_s = -\boldsymbol{n} \times \boldsymbol{E} \tag{2}$$

where **n** is the unit vector orthogonal to the surface and directed outward. In CST, it can be achieved with the Field Source Monitor. As a result, the near-field coupling effect is included in this solution. Finally, we export the equivalent source into a new simulation file and add a probe to record its phase. Figure 5.1(b) presents the schematic of the new simulation. The distance between the probe and the new equivalent source is 2 m, and, it is large enough to be considered as far field for a wavelength of 800nm. Besides, the boundary conditions in x and y directions [Fig. 5.1(b)] are set to periodic boundary conditions. The boundary conditions in ±z direction are set to open. Using this method, the field radiated by the previous neighbors is not taken into account, and the phase shift produced by the considered element can be measured. Therefore, we refer to it as the Local Phase Method (LPM).

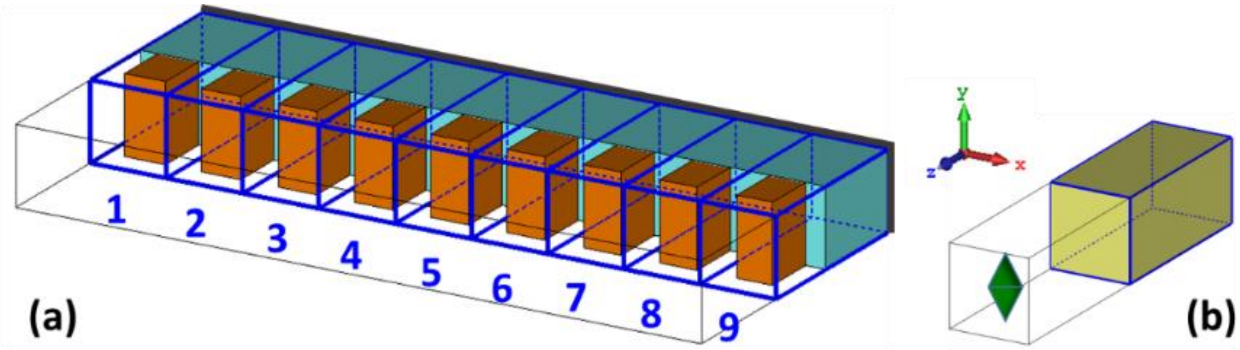

Figure 5.1: The schematic of the local phase method (LPM). The deflector super-cell is made of 9 different elements. (a) Super-cell illuminated by a plane wave coming from the left (top z plane) that interacts with the TiO_2 dielectric resonator (in brown) with a refractive index of 2.52 and is reflected by a metallic ground plane (grey-bold). The green-blue color represents the SiO_2 spacer. (b) Schematic of the new field source. The green rhombus represents the probe.

5.3 Deflector

To compare the UCM and the LPM, we use metasurface deflectors as a first example. A plane wave comes from the top z plane with a 10° incident angle. We design deflectors based on three types of elements. The first is a simple rectangular element based reflector [Fig. 5.2(a)] with weak coupling between its elements. The second deflector is made of rectangular elements embedded in a low refractive index material, SiO_2 [Fig. 5.2(b)] with $nSiO_2$=1.45. In this configuration, the smaller refractive index contrast decreases the field confinement inside the TiO_2 particles and the coupling between particles increases [20]. The third design consists in tilted parallelepiped elements with a tilted angle of 20° from the normal [Fig. 5.2(c)] [21]. The blue-green color in Fig. 5.2 (a)-(c) represents the low refractive index material (SiO_2). The brown color represents the TiO_2 material with a refractive index of 2.52 and the grey-bold represents the metallic ground plane. We chose to work in the visible spectrum at 800 nm to illustrate the LPM. Figure 5.2 (d)-2(f) presents the phase shift obtained in simulation with the UCM. In all cases, we take the phase provided by the longest length (L) as phase reference. The other dimensions are listed as insets. The theoretical deflection angles for the three cases are respectively 0.5°, 1.3° and 0.5°, given by $\theta_r = \sin^{-1}\left(\sin\theta_i - \frac{\lambda_0}{2\pi}\frac{\Delta\Phi}{p}\right)$, with $\theta_i = 10°$, $\Delta\Phi = 40°$ and $\lambda_0 = 800$ nm.

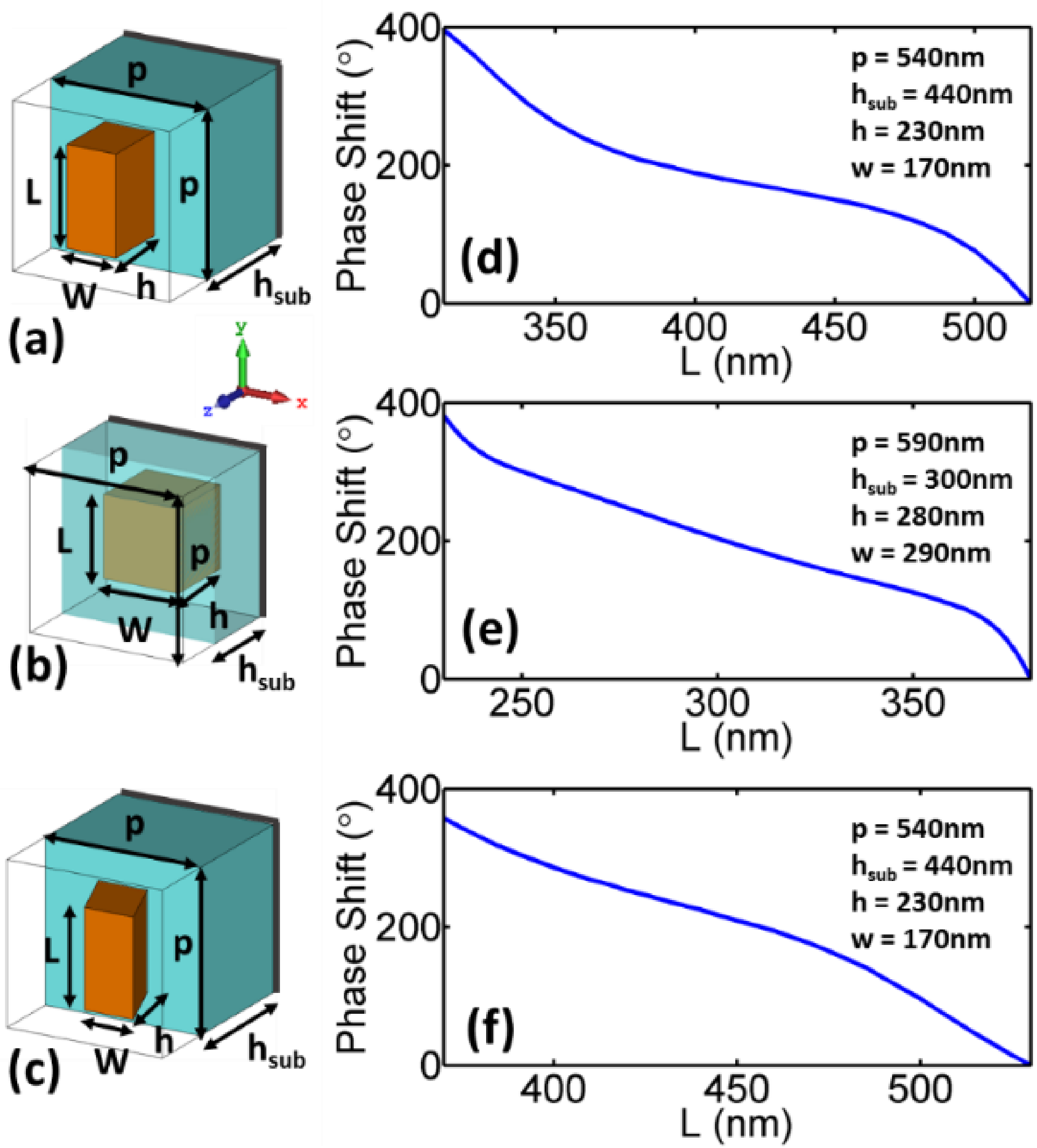

Figure 5.2: Dimensions of (a) the rectangular elements. (b) the rectangular elements with covered layer. (c) the parallelepiped elements. Phase-shift obtained with the UCM with (d) the rectangular elements, (e) the rectangular elements with covered layer and (f) the parallelepiped elements.

We first start with the rectangular elements design and compare it with the standard UCM design. The initial elements lengths of the optimized deflector are chosen with the UCM. The corresponding required lengths are shown in blue in Fig. 5.3(a). The radiated energy in the far-field, or equivalently the radar cross section (RCS), is given by the blue curve in Fig. 5.3(b). The

RCS exhibits a maximum value of 187 λ^2 at 0°. Subsequently, we use the LPM to obtain the real phase of the elements. Then, we tune the length of each element to optimize the phase difference between adjacent elements to be 40°. To do so, we use a derivative free approach based on the Matlab fminsearch algorithm which is well suited to optimize discontinuous functions, and we constrain the lengths to be between 100 and 540 nm [22]. The cost function to minimize is given by the sum of the square difference of the phases: $\sum_m |\Delta\varphi_m|^2$, where $\Delta\varphi_m$ is the phase error of the mth element, in other words, the phase difference between the target and the considered method (LPM and UCM).

The green circles in Fig. 5.3(a) correspond to the optimized dimensions by LPM. These optimized dimensions are used to provide the RCS plotted in Fig. 5.3(b). The RCS has been increased to 200 λ^2, corresponding to an enhancement of 7%. Figure 5.3(c) represents the comparison between the phase difference obtained from the LPM and the UCM. Figure 5.3(d) presents the absolute value of the phase for both methods with the UCM in blue and the LPM in green. The maximum phase error is about 40° for the UCM and is decreased to 20° for the LPM. The final RCS has not increased a lot as the near-field coupling difference of rectangular elements is initially minor.

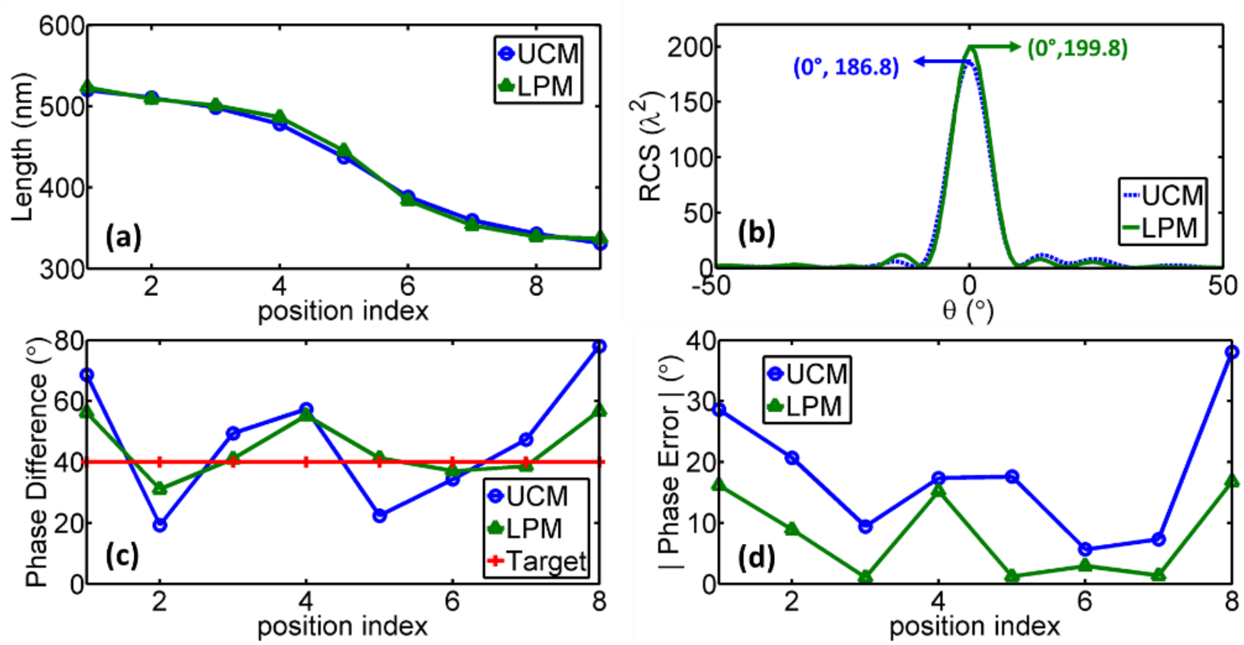

Figure 5.3: Designing metasurfaces with rectangular elements. (a) Dimensions for the UCM and LPM metasurface elements. (b) Radar cross-section of the UCM and LPM metasurfaces. (c) Phase difference between two adjacent elements for two metasurfaces. (d) Phase error for the UCM and LPM metasurfaces.

To further investigate our method, we now consider a new design with strong near-field coupling as is the case for rectangle elements embedded in a SiO_2 layer shown in Fig. 5.2(b). Figure 5.4(a) presents the lengths obtained with the UCM (blue) and LPM (green). Unlike the first situation, the dimensions of the LPM are quite different from the ones of the UCM. This is due to the strong near-field coupling effect. Figure 5.4(b) shows the RCS obtained with the two methods. We observe that the RCS exhibits two low peaks at -3° with a value of 120 λ^2 and at 8° with a value of 90 λ^2. It is worth noting that the period, in this case, is a little larger than in the previous case [Fig. 5.2(a)] and that the theoretical deflection angle is 1.3°. By using the same approach as in the case of the rectangle elements, the RCS for the LPM increases to 269 λ^2, i.e. more than a 124% enhancement compared to the UCM design. We also note that the maximum phase error (given by the phase obtained with the method minus the required theoretical phase) for the LPM is only about 30° while the maximum phase error of the UCM is more than 100°.

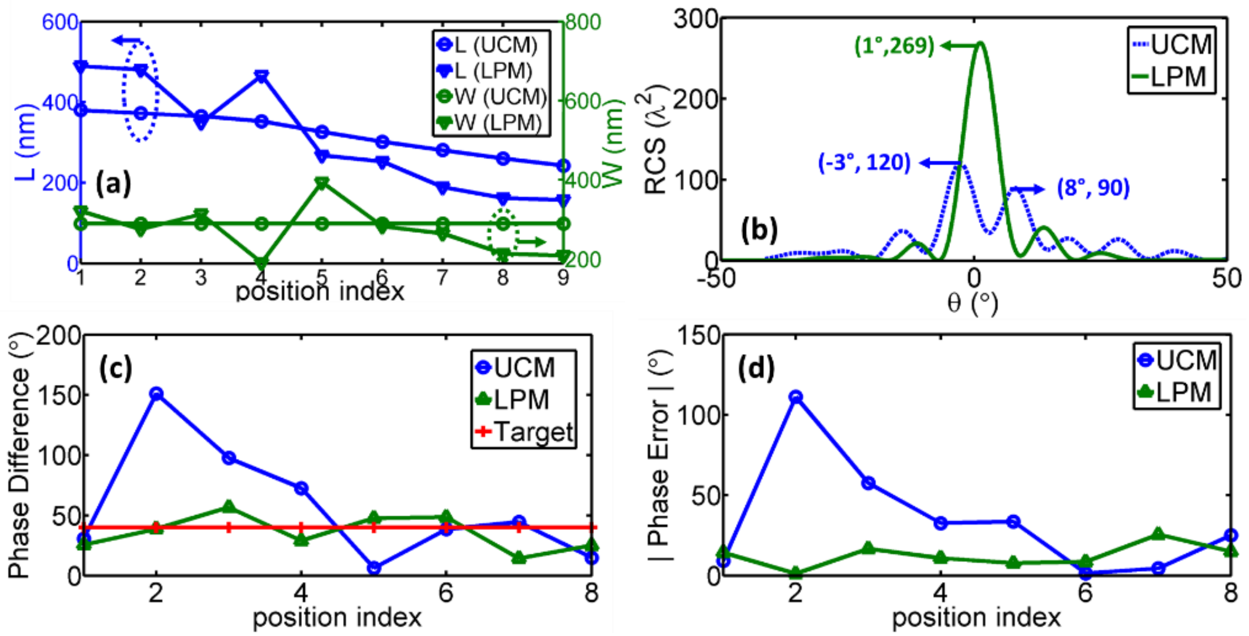

Figure 5.4: Designing metasurfaces with rectangular elements embedded in a SiO_2 layer. (a) Dimensions for the UCM and LPM metasurface elements. (b) Radar cross-section of the UCM and LPM metasurfaces. (c) Phase difference between two adjacent elements for two metasurfaces. (d) Phase error for the UCM and LPM metasurfaces.

The third design consists of slanted parallelepiped elements with a tilted angle of 20° as shown in Fig. 5.2(e). The concept figure is presented in Fig. 5.1(c) and the results are presented in Fig. 5.5. Unlike the rectangular ones [Fig. 5.3], the RCS at 0° is as small as 85 λ^2. Moreover, there is another beam at -10° which corresponds to specular reflection. On the other hand, the RCS for the LPM is shown in Fig. 5.5(b) and the RCS at 0° drastically increases to 180 λ^2, corresponding to an enhancement of 111%, and the secondary lobes are now negligible. Similarly, Figs. 5.5(c)-5(d) present the comparison of the phase difference between the two methods (UCM and LPM). As we can see, the LPM provides a phase much closer to the target. These results clearly show that, even if the near-field coupling difference is small, the LPM improves the efficiency of the metasurface devices. More importantly, when the near-field coupling difference becomes strong, our LPM significantly improves the results.

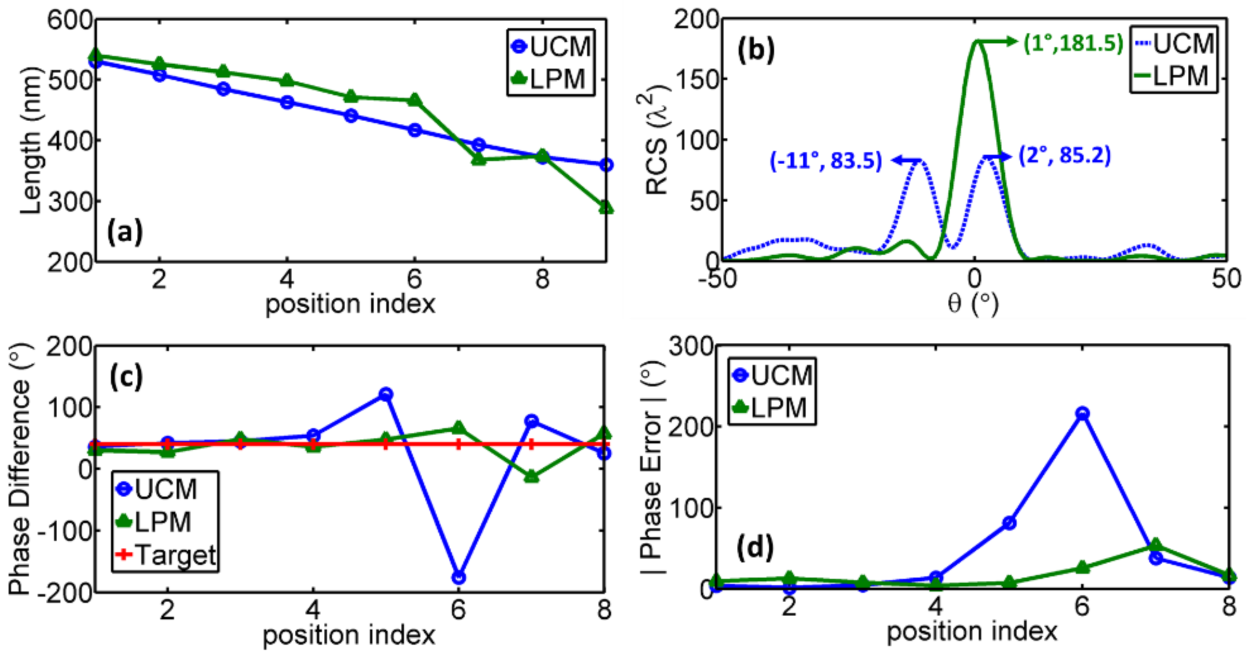

Figure 5.5: Designing metasurfaces with slanted parallelepiped elements. (a) Dimensions for the UCM and LPM metasurface elements. (b) Radar cross-section of the UCM and LPM metasurfaces. (c) Phase difference between two adjacent elements for two metasurfaces. (d) Phase error for the UCM and LPM metasurfaces.

5.4 High Numerical Aperture Concentrator

We now investigate a second class of devices by implementing a high numerical aperture concentrator where the advantage of the LPM over the usual UCM becomes evident. Figure 5.6(a) shows the unit cell dimensions (length) used to design the concentrator. The height is large enough to provide waveguide modes to the elements [23]. Figure 5.6(b) presents the phase shift obtained with the UCM. Again, we take the phase obtained with the largest dimension as the phase reference. The red curve in Fig. 5.6(c) represents the required theoretical phase (target) for the concentrator. We can observe that the first 8 elements have a smooth phase variation and the average of the absolute value of the phase difference between UCM and the target is 35°. However, when the slope or the derivative of φ(x) gets steeper, or discontinuous, the imposed phase shift is very different from the targeted one. About half of the elements are almost 150°

away from their targets. This is a consequence of the fact that the dimensions of the elements calculated by the UCM are extremely different from their neighbors and the coupling difference cannot be neglected anymore [Fig. 5.6(c)]. Figure 5.7(a) shows the real part of the reflected electric field. We can observe that the field is reflected towards the focal spot merely by the first eight elements. Figure 5.7(a) still shows a large discontinuity of the wave front around the 10th element because of its large phase error. On the other hand, in the LPM design, we optimize the dimensions of the elements from number eight to the end to obtain the desired phases. Overall, the phases obtained with our LPM optimization (in green in Fig. 5.6(c)) are much closer to their targets (in red) than with the UCM (in blue), except for some elements. This is due to the choice of our cost function $\sum_m |\Delta\varphi_m|^2$ which optimize the sum of the square difference and not all individual phase differences. For instance, to minimize the large error at element 18, we sacrifice a bit of the phase error at element 19. Interestingly, this may also indicate that the near-field coupling may impose some limits on the optimization approach and that it is not always possible to find a length distribution that fits exactly the theoretical phase profile of a perfect concentrator [24]. This may also be attributed to our optimization algorithm that is known to converge towards local maxima for high dimensional problems [22]. However, the optimization is still very efficient. Figure 5.8 presents the total power density produced by the metasurface concentrator with the UCM [Fig. 5.8(a)] and with the optimization based on the LPM [Fig. 5.8(b)]. We can see that the energy at the focal spot is increased by 15%, with a larger longitudinal length for a slightly reduced width.

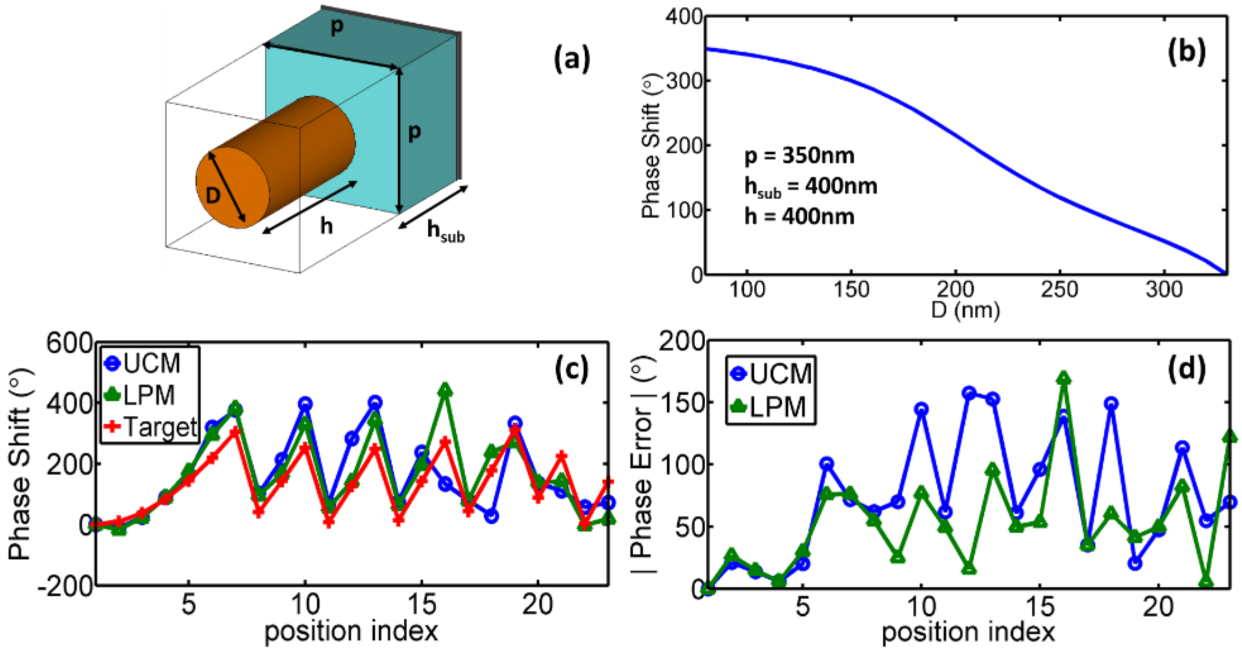

Figure 5.6: (a) The schematic of the concentrator. (b) Dimensions for unit cell method and LPM (c) Phase difference between two adjacent elements for the two methods. (d) Phase error for the two methods.

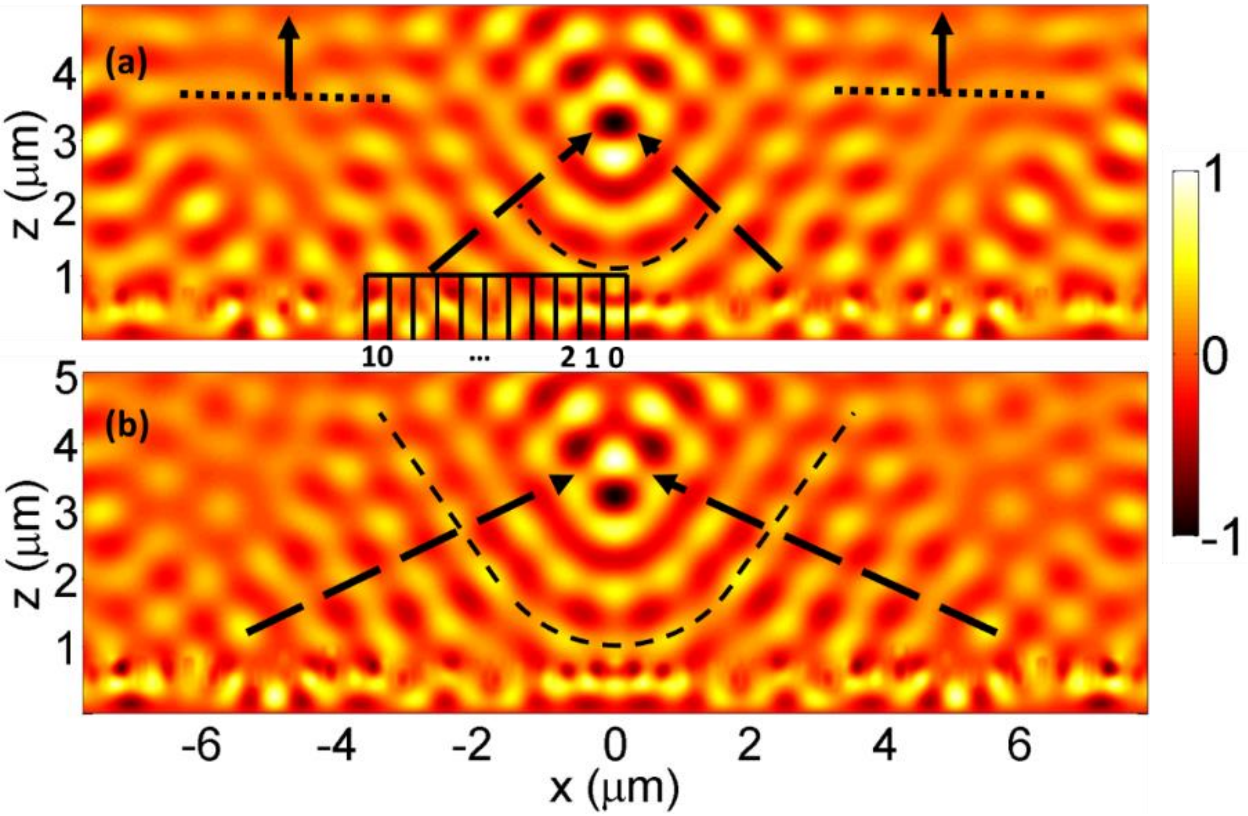

Figure 5.7: Real part of the reflected electric field for (a) the UCM, and (b) for the LPM. The black rectangular boxes represent the index position of the first 11 elements (from 0 to 10).

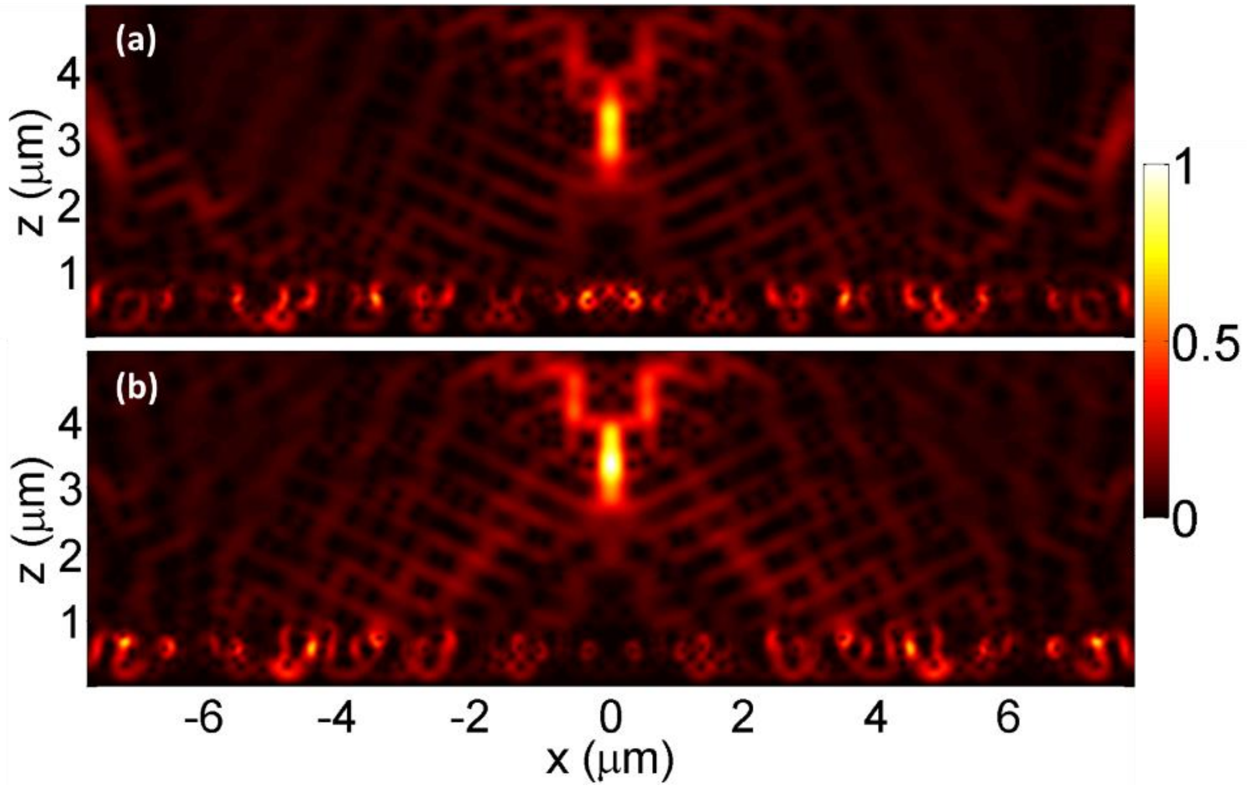

Figure 5.8: Total power density plot for (a) the UCM, and (b) for the LPM. The LPM increase the power at the spot.

5.5 Conclusion

In summary, we have proposed the local phase method, a versatile approach to quantify the phase error of each element within a metasurface accounting for the near-field coupling. The method improves the performance of devices based on metasurfaces. We have investigated two different applications, namely deflectors and high numerical aperture concentrators, to illustrate the impact of the LPM on the efficiency of metasurface devices. Even for devices with small near-field coupling, for which the UCM performs quite well, quantifying the local phase can improve the efficiency. In more advanced devices were near-field coupling is more important, optimizing the phase error using our LPM drastically improves the radar cross-section. The simplicity and the versatility of the LPM will lead to the design of highly-efficient metasurfaces and complex electromagnetic devices that rely on the discretization of theoretical profiles such as in transformation optics.

Chapter 5, in part, is a reprint of the material as it appears L.-Y. Hsu, M. Dupré, A. Ndao, J. Yellowhair, B. Kanté, “Local phase method for designing and optimizing metasurface devices,” Optics express 25 (21), 24974-24982 (2017). The dissertation author was the primary researcher and author of this paper.

5.6 Reference

1. N. Yu, F. Aieta, P. Genevet, M. A. Kats, Z Gaburro, F. Capasso, “A broadband, background-free quarter-wave plate based on plasmonic metasurfaces,” Nano Lett., 12 (12), pp 6328–6333 (2012).

2. Y. Zhao and A. Alù, “Manipulating light polarization with ultrathin plasmonic metasurfaces,” Phys. Rev. B 84, 205428 (2011).

3. P. Genevet, F. Capasso, F. Aieta, M. Khorasaninejad, R. Devlin, “Recent advances in planar optics: from plasmonic to dielectric metasurfaces,” Optica 4 (1), 139-152 (2017).

4. A. Arbabi, Y. Horie, M. Bagheri, A. Faraon, “Dielectric metasurfaces for complete control of phase and polarization with subwavelength spatial resolution and high transmission,” Nat. Nanotechnol. 10, 937–943 (2015).

5. F. Aieta, M. A. Kats, P. Genevet & F. Capasso, “Multiwavelength achromatic metasurfaces by dispersive phase compensation,” Science 347, 1342–1345 (2015).

6. P. Lalanne and P. Chavel, “Metalenses at visible wavelengths: past, present, perspectives,” Laser & Photonics Reviews 11 (2017).

7. Z. Wang, K. Yao, M. Chen, H. Chen, and Y. Liu, “Manipulating Smith-Purcell Emission with Babinet Metasurfaces,” Physical Review Letters 117, 157401, (2016).

8. J. He, Z. Xie, S. Wang, X. Wang, Q. Kan, Y. Zhang, “Terahertz polarization modulator based on metasurface,” J. Opt. 17 105107 (2015).

9. E. Maguid, I. Yulevich, M. Yannai, V. Kleiner, M. L Brongersma and E. Hasman, “Multifunctional interleaved geometric-phase dielectric metasurfaces,” Light: Science & Applications e17027 6 (2017).

10. L.Y. Hsu, T. Lepetit and B. Kanté, “Extremely Thin Dielectric Metasurface for Carpet Cloaking,” Progress In Electromagnetics Research, 152, 33-40 (2015).

11. X. Ni, Z. J. Wong, M. Mrejen, Y. Wang, and X. Zhang, “An ultrathin invisibility skin cloak for visible light,” Science 349, 1310–1314 (2015).

12. L. Y. Hsu, M. Dupré, A. Ndao, and B. Kanté, “From Parabolic-Trough to Metasurface-Concentrator: Assessing Focusing in the Wave-Optics Limit,” Opt. Letters, 1520 (2017).

13. C. Simovski, D. Morits, P. Voroshilov, M. Guzhva, P. Belov, Y. Kivshar, “Enhanced efficiency of light-trapping nanoantenna arrays for thin-film solar cells,” Opt. Express, 21, S3, A714 (2013).

14. R. Schmidt, A. Slobozhanyuk, P. Belov and A. Webb, “Flexible and compact hybrid metasurfaces for enhanced ultra-high field in vivo magnetic resonance imaging,” Sci. Rep. 7, 1678 (2017).

15. J.-H. Park, A. Kodigala, A. Ndao, and B. Kanté, “Hybridized Metamaterial Platform for Nano-Scale Sensing,” Opt. Express 25, 15590 (2017).

16. S. Zhan, Y. Peng, Z. He, B. Li, Z. Chen, H. Xu, and H. Li, “Tunable nanoplasmonic sensor based on the asymmetric degree of Fano resonance in MDM waveguide,” Sci. Rep. 6(1), 22428 (2016).

17. Lingling Huang , Xianzhong Chen, Holger Mühlenbernd, Hao Zhang, Shumei Chen, Benfeng Bai, Qiaofeng Tan, Guofan Jin, Kok-Wai Cheah, Cheng-Wei Qiu, Jensen Li, Thomas Zentgraf & Shuang Zhang, “Three-dimensional optical holography using a plasmonic metasurface,” Nat. Commun. 4, 2808 (2013).

18. Yu, N., P. Genevet, M. A. Kats, F. Aieta, J.-P. Tetienne, F. Capasso, and Z. Gaburro, “Light propagation with phase discontinuities: Generalized laws of reflection and refraction,” Science 334, 333–337 (2011).

19. C. Balanis, Antenna Theory, Analysis, and Design, chapter 12.2, 3rd Ed. New York: Wiley, (2005).

20. D. S. Boyuk, L.-W. Chou, M. A. Filler, “Strong Near-Field Coupling of Plasmonic Resonators Embedded in Si Nanowires,” ACS Photonics, 3, 184-189 (2016).

21. A. Ndao, A. Belkhir, R. Salut, and F. I. Baida, “Slanted annular aperture arrays as enhanced-transmission metamaterials: Excitation of the plasmonic transverse electromagnetic guided mode,” Appl. Phys. Lett. 103, 211901 (2013).

22. T. Alaridhee, A. Ndao, MP Bernal, E Popov, AL Fehrembach, FI Baida, “Transmission properties of slanted annular aperture arrays. Giant energy deviation over sub-wavelength distance”, Optics express 23 (9), 11687-11701 (2015).

23. A Ndao, J Salvi, R Salut, MP Bernal, T Alaridhee, A Belkhir, FI Baida, “Resonant optical transmission through sub-wavelength annular apertures caused by a plasmonic transverse electromagnetic (TEM) mode”, Journal of Optics 16 (12), 125009 (2014).

24. A. Ndao, Q. Vagne, J. Salvi, F.I. Baida, “Polarization sensitive sub-wavelength metallic structures: toward near-field light confinement control”, Applied Physics B 106 (4), 857-862 (2012).

25. J. C. Lagarias, J. A. Reeds, M. H. Wright, and P. E. Wright. “Convergence Properties of the Nelder-Mead Simplex Method in Low Dimensions,” SIAM Journal of Optimization. 9 (1) 112–147 (1998).

26. M. Khorasaninejad, A. Y. Zhu, C. Roques-Carmes, W. T. Chen, J. Oh, I. Mishra, R. C. Devlin, F. Capasso, “Polarization-insensitive metalenses at visible wavelengths,” Nano Lett., 16 (11) 7229–7234 (2016).

27. T. Lepetit and B. Kanté, “Cramér-Rao bounds for determination of electric and magnetic susceptibilities in metasurfaces,” Opt. Express 23, 3460-3471 (2015).

Chapter 6

From parabolic-trough to metasurface-concentrator: assessing focusing in the wave-optics limit

Metasurfaces are promising tools towards novel designs for flat optics applications. As such their quality and tolerance to fabrication imperfections need to be evaluated with specific tools. However, most such tools rely on the geometrical optics approximation and are not straightforwardly applicable to metasurfaces. In this Letter, we introduce and evaluate, for metasurfaces, parameters such as the intercept factor and the slope error usually defined for solar concentrators in the realm of ray-optics. After proposing definitions valid in physical optics, we put forward an approach to calculate them. As examples, we design three different concentrators based on three specific unit cells and assess them numerically. The concept allows for the comparison of the efficiency of the metasurfaces, their sensitivities to fabrication imperfections and will be critical for practical systems.

6.1 Introduction

Metasurfaces, as a two-dimensional version of metamaterials, have raised significant attention due to the simplified design afforded by generalized Snell's laws of reflection and refraction [1]. They consist of arrangements of subwavelength elements and provide powerful solutions to control the phase, the amplitude and the polarization of waves at subwavelength scales. The metasurfaces can be theoretically modeled in terms of surface polarizabilities (electric and magnetic) with physical bounds [2-3]. They offer a promising platform for applications including optical devices for polarization conversion [4], beam splitters [5], beam scanning [6], carpet cloaking [7-8], holography [9] and concentrators [10-12]. Among these applications, metasurface metalens and concentrators are receiving considerable attention due to their capabilities for flat and integrable optics, super-focusing, super-imaging and solar energy.

Conventional lenses are bulky as they rely on the Snell-Descartes laws of refraction and propagation over large distances—compared to the wavelength—to focus light. On the other hand, metalenses can concentrate light with very thin surfaces—of the order of micrometers— by imposing an abrupt phase-shift to light at some interface. For instance, a parabolic metallic concentrator can be replaced by a thin and flat metasurface which provides, to a normally incoming plane wave, the parabolic phase-shift given by:

$$\Phi = k_0(\sqrt{x^2 + f^2} - f) \tag{1}$$

where k_0 is the free space wave-vector, x is the distance between the considered element and the center of the lens and f is the focal length. In general, only the focusing efficiency is considered to determine the quality of metalenses [11-12]. The latter corresponds to the ratio of the power incident on the focus to the power incident on the lens. In the solar concentrator field, the efficiency is defined as the ratio of solar energy collected by the receiver—an optical absorber—to that intercepted by the concentrator. The total optical efficiency of a solar concentrator is given by the combination of the so-called intercept factor, the reflectance of the concentrator, and the absorbance of the latter [14]. Since the efficiency of an energy concentrator is extremely sensitive to its geometrical parameters, it is essential to develop methods that allow their optimization.

In this Letter, we introduce a method to compare the quality of concentrators in the realm of metasurfaces. Specifically, we generalize the concepts of the slope error and the intercept factor. An approach based on finite difference time domain (FDTD) simulations is proposed to evaluate the efficiency of concentrators. As examples, we design in the optical domain three metasurfaces based on different unit cells (with cylindrical, rectangular and ellipsoidal elements) made of titanium dioxide (TiO_2) [13]. We compare the three designs with our approach and show that the rectangular element has the minimal sensitivity to fabrication imperfections.

6.2 Intercept factor and slope error

Solar concentrators are usually made of parabolic mirrors that focus light from the sun onto a receiver. The dimensions of such mirrors and their focal length can reach several meters. In such conditions, their optical properties are efficiently described within the ray-optics approximation. In the solar concentrator field, specific parameters, based on geometrical optics considerations, such as the slope error and the intercept factor are generally used to characterize the efficiency of such devices. In nanostructured dielectrics, referring to ray-optics considerations does not make sense anymore, and the traditional parameters have to be adapted within a wave optics frame. We start here by introducing the intercept factor and the slope error as discussed in the solar concentrator field. We then propose to use such concepts for metasurface concentrators. Based on these parameters we quantitatively analyze the quality of metasurface concentrators.

In the solar concentrator field [14-18], the intercept factor and the slope error allow the description of the imperfections of a solar concentrator. The intercept factor is defined as the ratio of the ray incident on the concentrator that is intercepted by the receiver. Equivalently, we can define it as the ratio of the number of rays that hit the receiver to the number of rays impinging onto the concentrator. The slope error is locally given by the difference of angle between the normal of the mirror surface with respect to the normal of the ideal surface. Ideally, the parabolic slope of the mirror is perfect, the slope error is null, all rays intercept the receiver and the intercept factor is unity. In practice, the curve of the mirror is not perfect due to fabrication imperfections, the slope of the mirror deviates from the ideal one and the slope error is finite—generally of the order of 10^{-3} rad. As a result, some rays are not reflected in the expected direction and miss the receiver. The intercept factor is, therefore, inferior to one, with recommended values around 95% [16].

Fig. 6.1(a) illustrates the slope error and the intercept factor for conventional solar concentrators. The blue parabolic curve represents the ideal mirror while the brown one represents the real mirror. A ray incident on the surface mirror is not reflected towards the initial direction due to the slope error $\Delta\theta$ but with an angular error of $2\Delta\theta$, that can make it miss the receiver if $2\Delta\theta R > D/2$, where D is the diameter of the receiver and R the distance between the latter and the mirror.

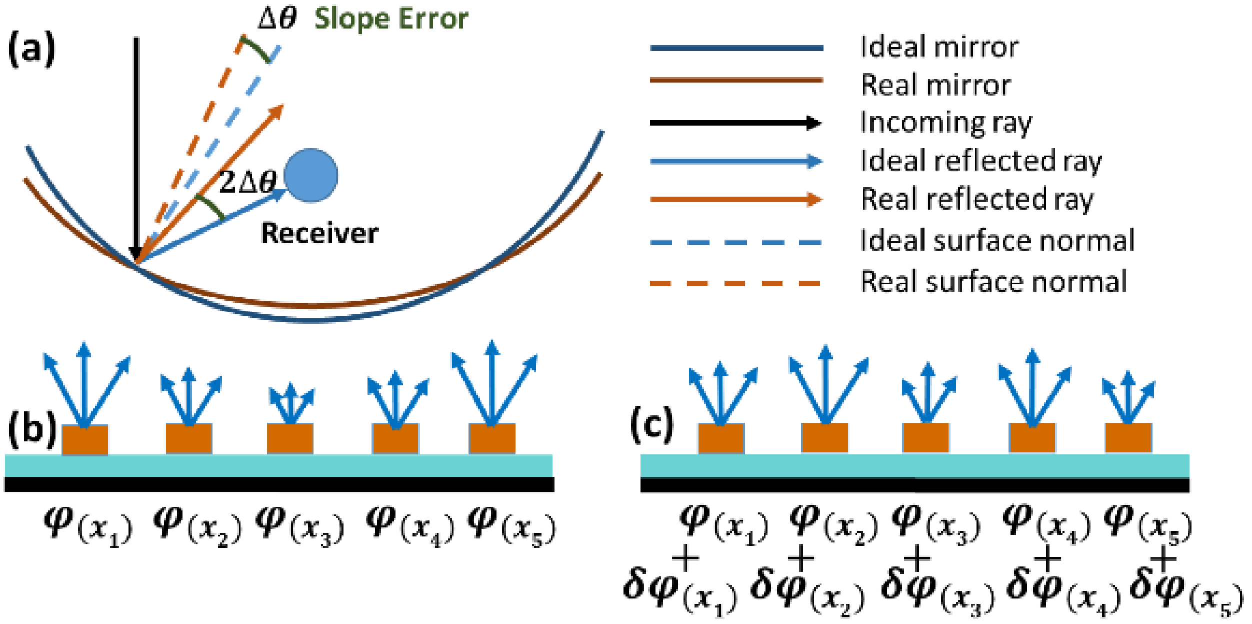

Figure 6.1: (a) Schematic of the parabolic concentrator: comparison between the ideal and real cases. (b) Ideal metasurface with uniform sampling of the exact phase required for a concentrator. (c) Real metasurface with a phase variation δφ due to fabrication imperfections.

6.3 Quantitative analysis of IF/SE in non-perfect metasurface

In the context of metasurface lenses and concentrators, such definitions based on ray-optics cannot hold anymore. Fig. 6.1(b) represents an ideal metasurface which elements impose an ideal phase φ to an incoming plane wave at different positions (x_1, x_2,…, x_n). This is the equivalent of the ideal slope of traditional parabolic mirrors. Fig. 6.1(c) schemes a real metasurface which elements impose a non-ideal phase that can be modeled as the sum of the ideal phase-shift with an additional deviation $\delta\varphi(x)$ due to fabrication imperfections. With metasurface, we prefer to refer to the power rather than considering a number of rays that do not have much meaning anymore. Hence, we can re-define the intercept factor as the ratio of the integrated power on the receiver to the power incident on the metasurface. As in the ray-optics case, if there is no absorption, the intercept factor is unity for a perfect fabrication without any phase variation ($\delta\varphi(x) = 0$). Generalizing the slope error is not as straightforward. In the ray-optics case, the slope error and the intercept factor are intimately related. Indeed, the loss of efficiency is characterized by the intercept factor and can be seen as the effect of the fabrication imperfections, characterized by the slope error. In other words, the slope error evaluates the cause, while the intercept factor assesses its effects. For traditional solar concentrators, the curved mirror has been used to bend light and focus it, which lead to the definition of the slope error. Metasurfaces are generally flat and rely on phase gradients and interferences to focus light. The corresponding equations for the ideal and real cases are respectively:

$$\begin{cases} \sin\theta_i - \sin\theta = \frac{1}{k_0}\frac{d\varphi(x)}{dx} \text{ for the ideal case} \\ \sin\theta_i - \sin(\theta + \delta\theta) = \frac{1}{k_0}\frac{d(\varphi(x)+\delta\varphi(x))}{dx} \text{ for the real case} \end{cases} \quad \textbf{(2)}$$

where θ_i is the angle of the incident plane wave, θ the angle of the reflected wave in the ideal case and $\theta + \delta\theta$ the angle of the reflected wave in the real case. This leads us to define the equivalent of the slope error, a unitless phase gradient error.

$$Slope\ Error = \left|\frac{1}{k_0}\frac{d\delta\varphi}{dx}\right| \quad \textbf{(3)}$$

In this case, $d\delta\varphi/dx$ can be approximated as the ratio of the phase difference between two adjacent elements to *dx,* the distance between two resonators.

The phase shift induced by the resonant elements strongly depends on the difference between the operating frequency and the resonant frequency, and the latter is mainly sensitive to the elements dimensions. Hence, the dominant source of phase error is the fabrication imperfection resulting in mismatches between the obtained dimensions of the elements and their nominal values. Most of the time, these imperfections can be modeled as a random noise on the dimensions and positions of the elements, as any constant bias can be overcome by carefully adapting the fabrication process.

In order to show how such fabrication imperfections can degrade the efficiency of a metasurface, and how they can be characterized by the intercept factor and by the slope error, we designed metasurfaces with three different geometrical structures: cylinders (Fig. 6.2(a)), rectangular parallelepipeds (Fig. 6.2(b)), and ellipses (Fig. 6.2(c)) that are widely used to design elements of metasurfaces [10-12]. We chose to work in reflection and in the visible spectrum at 800 nm to illustrate the concept. Therefore, we place our elements on a metallic ground plane, in black color in Fig. 6.2, and which will be modeled as Perfect Electric Conductor (PEC) in our FDTD simulations. Hence, we optimize their quality factor Q by tuning the thickness of a SiO_2 layer—represented in blue in Fig. 6.2—with a refractive index of 1.45 at the considered wavelength. On top of it, we deposit our TiO_2 elements—represented in brown in Fig. 6.2—with a refractive index of 2.52 for λ=800 nm [19-20].

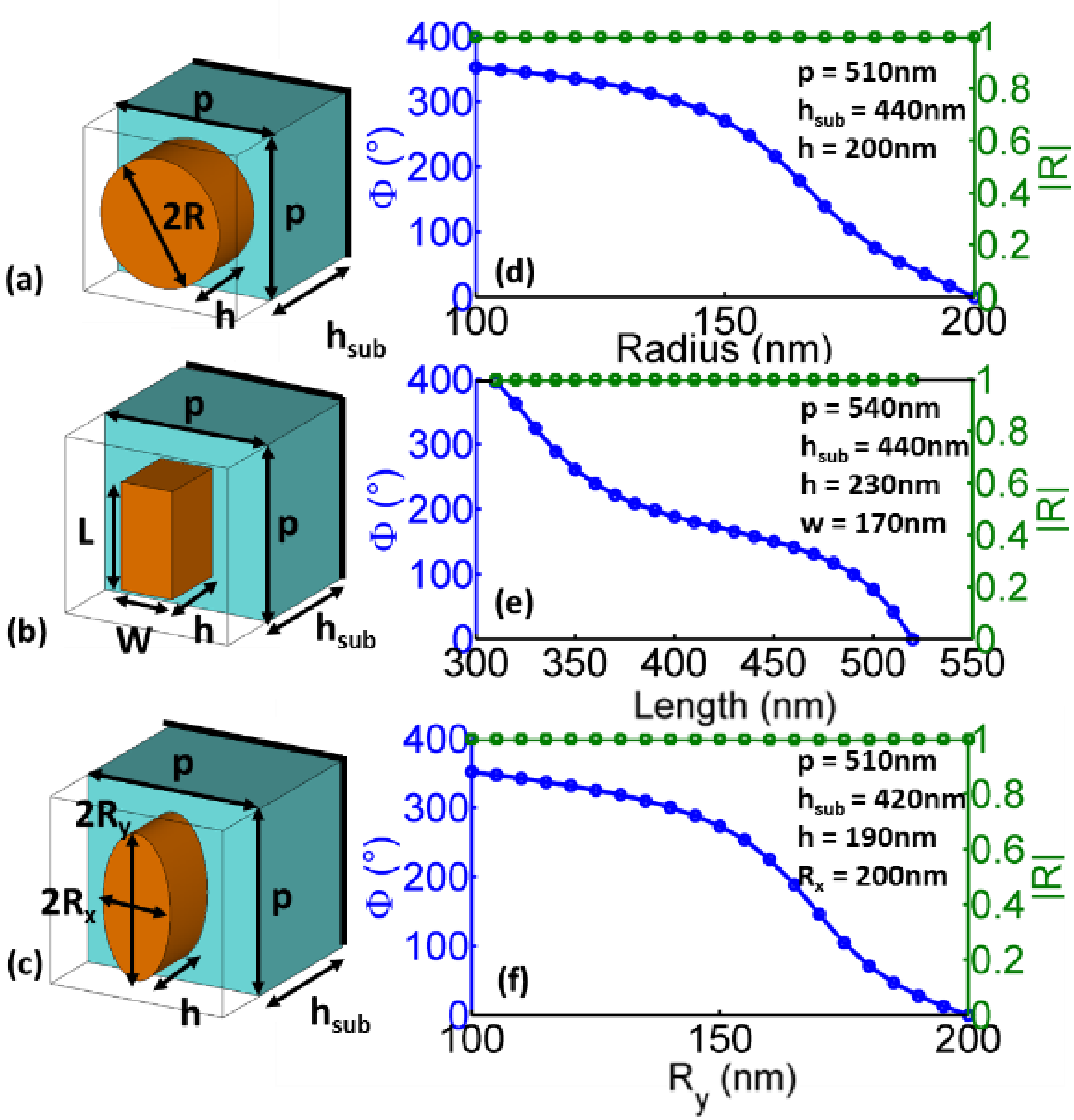

Figure 6.2: (a-c) Schematic of a conventional metasurface structure (cylinders, rectangular parallelepipeds and ellipses.) with the geometrical parameters: p is the period, h is the thickness of the resonator, R is the radius, h_{sub} is thickness of the substrate, W is the width, Rx is the radius in x direction and Ry is the radius in y direction. The brown color represents the TiO_2 material, the blue-green is SiO_2 and the black bold represents the ground plane. (d-f) Phase shift for different size of the cylinders, rectangular parallelepipeds and ellipses.

Tuning one geometrical parameter of each element—the radius of the cylinders, the length of the rectangles and the semi-axis in the y direction of the ellipses—modifies the eigenfrequency of the Mie mode of the corresponding elements. As a consequence, the phase-shift induced to an incident wave is modified. Fig. 6.2 (d-f) presents the resulting phase-shifts at a wavelength of 800 nm for the three considered geometries. The results are obtained with a commercial finite element code, with unit cell boundary condition in the plane of the metasurface. The cylinders and ellipses look very similar as they have closely related geometries, but they strongly differ from the rectangles, even if we could have expected the ellipsoidal elements to be an intermediary element between the cylindrical and rectangular ones. Furthermore, we can anticipate that the steepest the curve, the more sensitive is the element towards fabrication imperfections as a small parameter change will produce a large phase-shift.

In what follows, we propose to investigate more quantitatively the effects of fabrication imperfections. A solution would consist in fabricating the three metasurfaces, but it would be difficult to precisely tune the randomness of the fabrication imperfections. Therefore, we propose to adopt a simpler approach relying on FDTD simulations. We modeled the fabrication imperfections as a random phase noise that adds to the phase shift of the elements. Hence, the total phase at each element is given by, $\Phi_{\text{real}} = \Phi + \varepsilon\ \Delta P(\Phi)$. Where Φ_{real} is the phase of the element with fabrication imperfections, Φ is the ideal parabolic phase. ε is a random number between -0.5 and 0.5, picked up from a uniform distribution. The type of the distribution is not really important as long as its mean and standard deviation are defined and that all elements have independent imperfections, thanks to the central limit theorem. ΔP is the magnitude of the random number which is a function of the phase shift Φ.

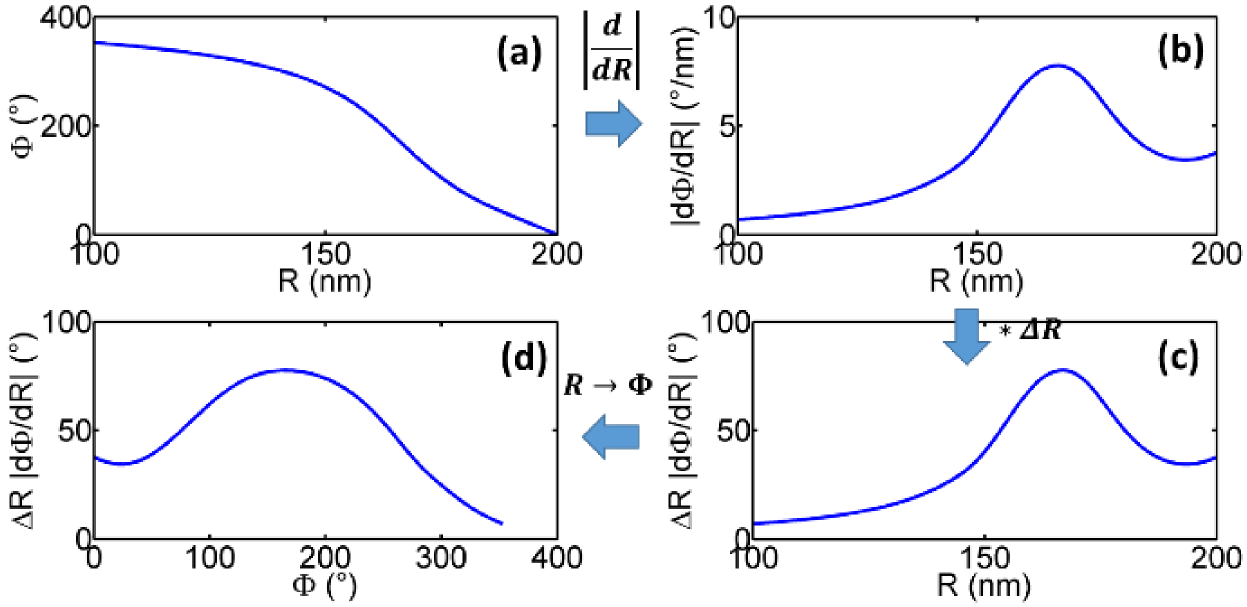

Figure 6.3: Flowchart of transformation. (a) The phase shifts as a function of a geometrical parameter. (b) The sensitivity of the phase shifts to the parameter resolution in degree/nm. (c) Same in absolute value for an average noise of 10 nm. (d) Sensitivity in degree as a function of the targeted phase shift.

We will now link the fabrication imperfections to the phase noise. Fig. 6.3 illustrates our approach for the cylindrical element. Fig. 6.3(a) presents the phase shift Φ(R), provided by the elements as a function of the radii. Then, we calculate |dΦ(R)/dR| the absolute value of the derivative of the phase-shift with respect to the radius—shown in Fig. 6.3(b)—which can be seen as a quantitative measure of the phase sensitivity to the size variation. This value is maximum for the elements which are the most sensitive to noise, i.e. the points of Fig. 6.3(a) for which the slope of the curve is maximum. We multiply the sensitivity by the average size variation (ΔR) (see Fig. 6.3(c)). In real experiments, such value is around 10 nm for conventional electron beam lithography techniques [21]. Hence, the curve plot in Fig. 6.3(c) represents the average phase error—in degree—for an element with radius R. Finally, we convert the parameter size axis into its phase shift (Φ) counterpart, using the bijection of Fig. 6.3(a). This curve, presented in Fig.

6.3(d) shows the average phase noise on an element for the desired phase Φ. The maximum of this noise reaches 80° for a phase shift of 170° and which corresponds to a radius R equals to 170 nm. Using this approach, we calculate the sensitivity of the phase-shift for the rectangles and the ellipses. Results are presented in Fig. 6.4. As noticed before, the sensitivity of the cylinders and ellipses are similar with a maximum around 180 degrees, while the rectangular elements have a minimum of sensitivity around this value. We only considered variations in one dimension, even though, in practical fabrication, elements could have variations in other dimensions which would reduce the intercept factor. However, our approach is general and can be expanded to consider more fabrication imperfections.

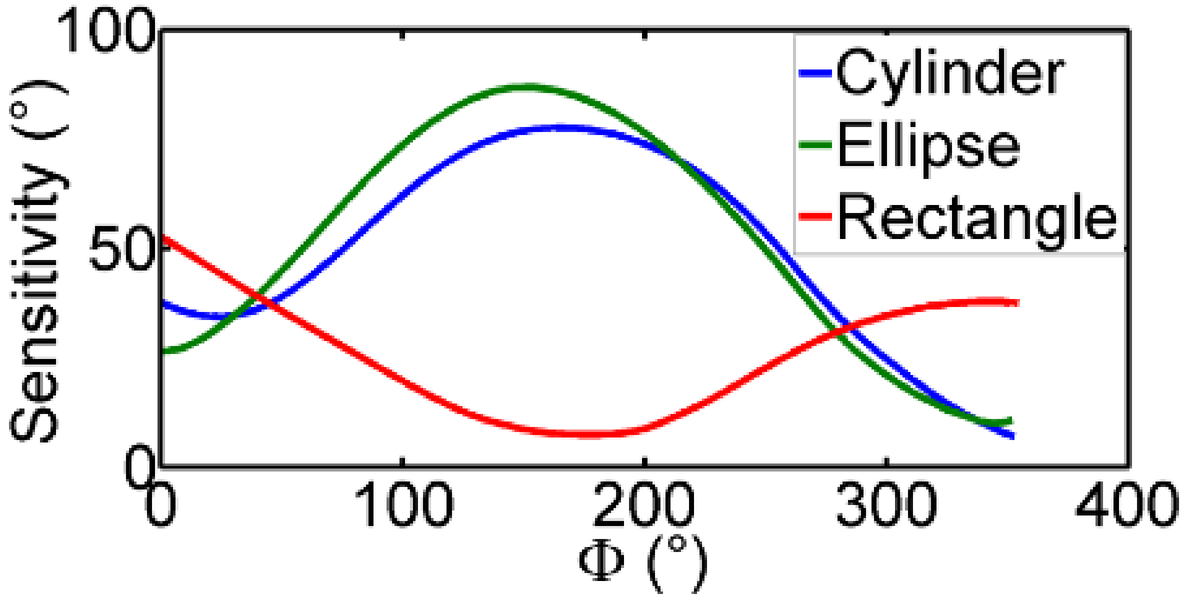

Figure 6.4: Sensitivity for cylinders, ellipses and rectangular parallelepipeds.

To statistically analyze our metasurface concentrators, we run 100 simulations for each element using a homemade FTTD code. Each simulation was given a certain magnitude of the noise related to the type fabrication imperfections. We simulate a 115µm-long metasurface with a focal length of 170µm, and 241 elements. To reduce the computational time, we replace the wave reflected by the metasurface elements by point sources. Their phases are set to match the phase of a concentrator with a random spatial phase noise given by the approach described in Fig. 6.3 and a given magnitude of the fabrications imperfections (from 0 to 20 nm). Based on this method, we calculate the intercept factors of metasurfaces designed with the three common elements.

Fig. 6.5(A$_1$) shows the intercept factor as a function of fabrication imperfections. For a structure without fabrication imperfections, the value of the intercept factor is equal to unity as illustrated in Fig. 6.5(A$_1$). The field is very well focused (see Fig. 6.5(B$_1$)). For example, for a fabrication imperfection value equal to 10 nm for cylinders and ellipses, the value of the intercept factor is about 0.72 (as illustrate in Fig. 6.5(B$_2$)). In the case of the rectangular parallelepipeds a similar intercept factor of 0.71 (see Fig. 6.5(B$_3$)) is obtained for twice as larger fabrication imperfections (20nm). . For this same value of fabrication imperfections in the case of a cylinder and the ellipse, the value of the intercept factor is 3 times smaller than the rectangular one. (Fig. 6.5(B$_4$)). Fig. 6.5(A$_2$) presents the slope error as a function of the fabrication imperfections. The ellipses and the cylinders metasurface have the approximately equal slope error value that is about twice that of the rectangle. This proves that the rectangular parallelepipeds are less sensitive to the considered fabrication imperfections, and they would be more advantageous to use to design highly efficient metasurfaces.

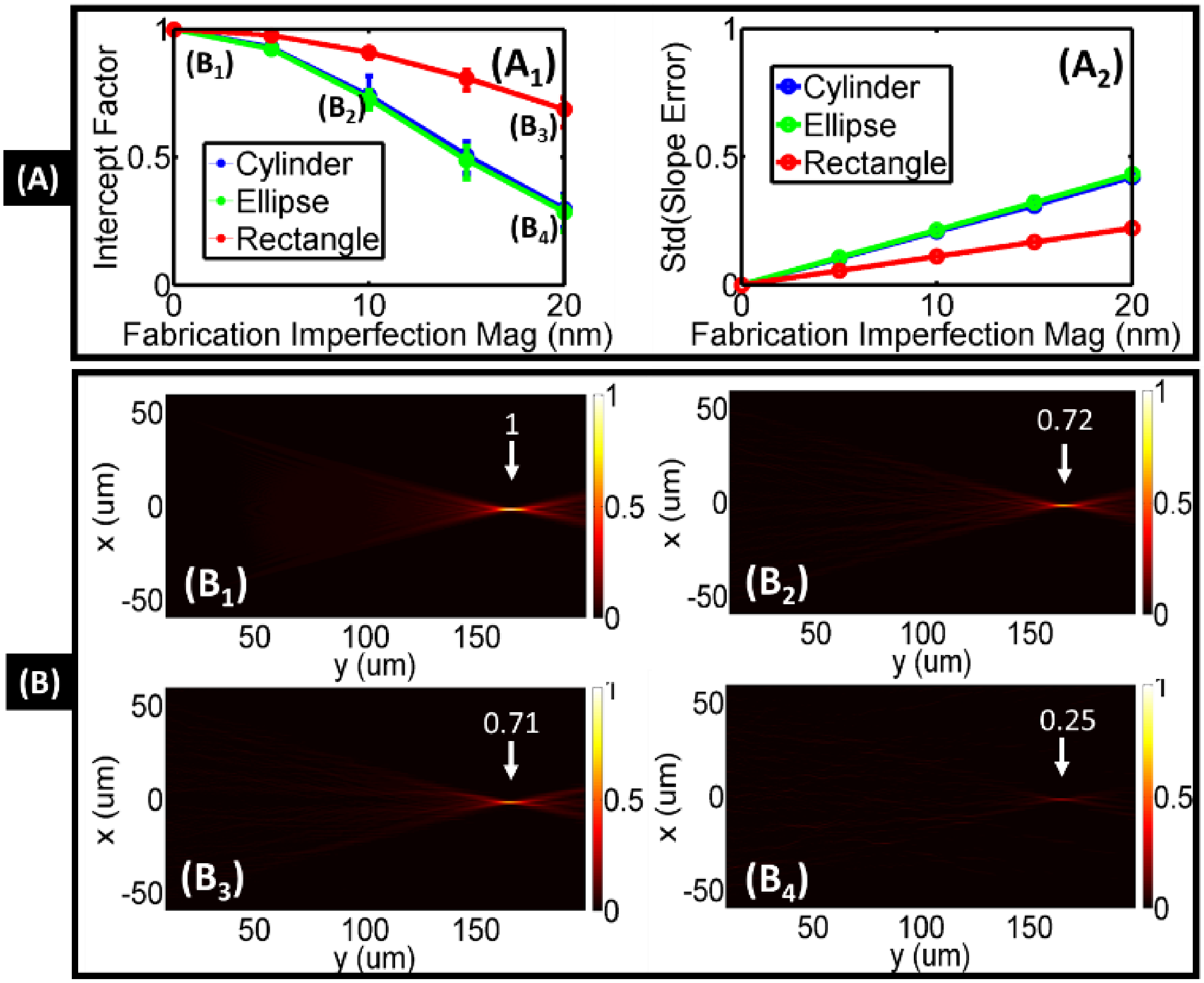

Figure 6.5: (A1) Intercept factor and (A2) Standard variation of the slope error for cylinders, rectangular parallelepipeds and ellipses. (B) Power pattern.

6.4 Conclusion

In conclusion, we presented an approach to evaluate the robustness of metasurface concentrators to fabrication imperfections. We started by describing the general methods used, and investigated three different geometries as unit cell elements with cylinders, rectangular parallelepipeds, and ellipses cross sections. We studied the effects of imperfection via the intercept factor and the slope error. Specifically, we have computed these quantities and shown that the rectangular parallelepipeds are less sensitive to fabrication imperfections compared to the ellipse and the cylinder. Our approach can provide a guidance to design large scale and highly efficiency metasurface concentrators.

Chapter 6, in part, is a reprint of the material as it appears L.-Y. Hsu, M. Dupré, A. Ndao, B. Kanté, “From parabolic-trough to metasurface-concentrator: assessing focusing in the wave-optics limit,” Optics letters 42 (8), 1520-1523 (2017). The dissertation author was the primary researcher and author of this paper.

6.5 Reference

1. Yu, N., P. Genevet, M. A. Kats, F. Aieta, J.-P. Tetienne, F. Capasso, and Z. Gaburro, “Light Propagation with Phase Discontinuities: Generalized Laws of Reflection and Refraction,” Science **334**, 333–337 (2011).

2. C. L.Holloway, A. Dienstfrey, E. F. Kuester, J. F. O’Hara, A. K. Azad, and A. J. Taylor, “A discussion on the interpretation and characterization of metafilms/metasurfaces: The two-dimensional equivalent of metamaterials,” Metamaterials **3**, 100–112(2009).

3. T. Lepetit and B. Kanté, “Cramér-Rao bounds for determination of electric and magnetic susceptibilities in metasurfaces,” Opt. Express **23**, 3460-3471 (2015).

4. N. Yu, F. Aieta, P. Genevet, M. A. Kats, Z. Gaburro, F. Capasso,” Nano Lett., **12**(12), 6328−6333 (2012).

5. T. Niu, W. Withayachumnankul, A. Upadhyay, P. Gutruf, D. Abbott, M. Bhaskaran, S. Sriram, and C. Fumeaux, “Terahertz reflectarray as a polarizing beam splitter,” Opt. Express **22**, 16148-16160 (2014).

6. J. Cheng and H. Mosallaei, “Optical metasurfaces for beam scanning in space,” Opt. Lett. **39**, 2719-2722 (2014).

7. L. Y. Hsu, T. Lepetit, B. Kante, “Extremely thin dielectric metasurface for carpet cloaking,” Prog. Electromagnetics Res. **152**, 33–40 (2015).

8. X. Ni, Z. J. Wong, M. Mrejen, Y. Wang and X. Zhang, “An ultrathin invisibility skin cloak for visible light,” Science **349**, 1310–1314 (2015).

9. G. Zheng, H. Mühlenbernd, M. Kenney, G. Li, T.Zentgraf, and S. Zhang, “Metasurface holograms reaching 80% efficiency,” Nat. Nanotechnol. **10**(4), 308–312 (2015).

10. Z. Ma, S. M. Hanham, P. Albella, B. Ng, H. T. Lu, Y. Gong, S. A. Maier, and M. Hong, “Terahertz All-Dielectric Magnetic Mirror Metasurfaces,” ACS Photonics, **3** (6), 1010–1018, (2016).

11. A. Zhan, S. Colburn, R. Trivedi, T. K. Fryett, C. M. Dodson, and A. Majumdar, “Low-contrast dielectric metasurface optics,” ACS Photonics **3**, 209–214 (2016).

12. A. Arbabi, Y. Horie, M. Bagheri and A. Faraon, “Dielectric metasurfaces for complete control of phase and polarization with subwavelength spatial resolution and high transmission,” Nature Nanotech. **10**, 937–943 (2015).

13. L. Zou, W. Withayachumnankul, C. M. Shah, A. Mitchell, M. Bhaskaran, S. Sriram, and C. Fumeaux, "Dielectric resonator nanoantennas at visible frequencies," Opt. Express **21**, 1344-1352 (2013).

14. Tiwari, G. N., and Arvind Tiwari, Handbook of Solar Energy: Theory, Analysis and Application (Springer, 2016).

15. D. Y. Goswami, F. Kreith, J. F. Kreider, Principles of Solar Engineering, Second Edition (CRC Press 2000).

16. Kreith F, Goswami DY. Handbook of energy efficiency and renewable energy, (Mech Eng Ser. Boca Raton: CRC Press; 2007).

17. Silverio García-Cortés, Antonio Bello-García and Celestino Ordóñez, “Estimating intercept factor of a parabolic solar trough collector with new supporting structure using off-the-shelf photogrammetric equipment,” Applied Energy, **92**, 815-821, (2012).

18. J. K. Stynes and B. Ihas, “A survey of methods for the evaluation of reflective solar concentrator optics,” (World Renewable Energy Forum Denver 2012).

19. I. H. Malitson, “Interspecimen Comparison of the Refractive Index of Fused Silica,” J. Opt. Soc. Am. **55**, 1205-1208 (1965).

20. J. R. DeVore, “Refractive indices of rutile and sphalerite,” J. Opt. Soc. Am. **41**, 416-419 (1951).

21. A. Kodigala, T. Lepetit, Q. Gu, B. Bahari, Y. Fainman, B. Kanté, doi:10.1038/nature20799.

Chapter 7

Summary

The thesis has been to state a comprehensive suitable definition of a metasurface and identify its salient features as well as highlight some of the numerous advantages which can be achieved through the use of metasurfaces. The sub-wavelength nature of building blocks of metasurfaces allows them to be defined using homogeneous boundary conditions. Another important characteristic of metasurfaces is the phase discontinuity which occurs when an electromagnetic wave goes through a metasurface. Both these behaviors can be successfully described by using generalized refraction and reflection laws. In this thesis, to illustrate the importance of the metasurfaces, we proposed and demonstrated different applications.

In chapter 2, we have reported an extremely thin dielectric metasurface carpet cloak. The geometrical scheme presented is general and can be used for any surface of class C1 and for frequencies up to the visible. We have also shown that despite being designed for 45 degrees, accepting a phase advance/delay of 3% of the period, results in an angular bandwidth of ±6 degrees. Moreover, this approach of bending electromagnetic waves with metasurfaces can be used not only for carpet cloaks but also for light focusing to make flat optics devices such as thin solar concentrators, quarter-wave plates, and spatial light modulators. Making these surfaces reconfigurable, we expect ideas proposed here to find applications in flexible devices.

In the chapter 3, we have proposed and numerically demonstrated a new and simple design for broadband metasurfaces carpet cloaking with linear polarization at visible wavelengths from 650 nm to 800 nm. The design consists of two high index ridges (Si_3N_4), separated by a narrow low index gap (air). Due to such refractive index discontinuity forming the slot waveguide, this structure allows one of the propagating modes to confine its energy within the slot region. The advantage of the slot waveguide is to mitigate materials dispersion by confining light in the subwavelength air gap region. The approach enables broadband operation for metasurfaces.

In Chapter 4, we proposed and experimentally demonstrated metalenses combining high efficiency, polarization independence, and achromaticity in the continuous wavelength range ranging from 640 nm in the visible to 1200 nm in the infrared. The broadband operation is achieved by enforcing the slopes of the phase-shift that vary continuously from the center of the lens to its edge, and, by minimizing the phase-shift intercepts that are ideally zero for achromatic operation. To the best of our knowledge, this is the broadest band achromatic metalens reported to date. The proposed approach significantly extends the current state of the art of metalenses both in terms of bandwidth and efficiency and opens the door to many applications.

In chapter 5, we have proposed the local phase method, a versatile approach to quantify the phase error of each element within a metasurface accounting for the near-field coupling. The method improves the performance of devices based on metasurfaces. We have investigated two different applications, namely deflectors and high numerical aperture concentrators, to illustrate the impact of the LPM on the efficiency of metasurface devices. Even for devices with small near-field coupling, for which the UCM performs quite well, quantifying the local phase can improve the efficiency. In more advanced devices were near-field coupling is more important, optimizing the phase error using our LPM drastically improves the radar cross-section. The simplicity and the versatility of the LPM will lead to the design of highly efficient metasurfaces and complex electromagnetic devices that rely on the discretization of theoretical profiles such as in transformation optics.

In chapter 6, we systematically analyzed and evaluated the robustness the impact of fabrication imperfection. We started by the general methods used and investigated three different geometries as unit cell elements with cylinders, rectangular parallelepipeds, and ellipses cross sections. We re-defined the intercept factor/ slope error in solar industry for metasurface to quantify the impact of fabrication imperfection. Our approach can provide a guidance to design large scale and highly efficiency metasurface concentrators.

With current metasurfaces and applications, one of the central issue is the nano-manufacturing to generate complex nano-patterns over large area with high throughput and low cost, particularly for the feature size less than 100 nm and pattern pitch less than 200 nm (i.e. below 100 nm) in an area larger than 1000 cm^2. Advance in this area will have a significant impact to a wide range of industrial applications, well beyond solar concentrator, such as semiconductors, solar cells, solid state lighting, fuel cells, data storage, optical communication, displays, biotechnology, to name a just a few.